UNIVERSIDAD COMPLUTENSE DE MADRID
FACULTAD DE FARMACIA

TESIS DOCTORAL

Nanomaterials for multimodal molecular imaging

Nanomateriales para imagen molecular multimodal

MEMORIA PARA OPTAR AL GRADO DE DOCTOR

PRESENTADA POR

Irene Fernández Barahona

Directores

Fernando Herranz Rabanal
Juan Pellico Sáez

Madrid

UNIVERSIDAD COMPLUTENSE DE MADRID

FACULTAD DE FARMACIA

NANOMATERIALS FOR MULTIMODAL MOLECULAR IMAGING

NANOMATERIALES PARA IMAGEN MOLECULAR MULTIMODAL

MEMORIA PARA OPTAR AL GRADO DE DOCTORA

PRESENTADA POR

Irene Fernández Barahona

DIRECTORES

Fernando Herranz Rabanal

Juan Pellico Sáez

UNIVERSIDAD COMPLUTENSE DE MADRID

FACULTAD DE FARMACIA

NANOMATERIALS FOR MULTIMODAL MOLECULAR IMAGING

NANOMATERIALES PARA IMAGEN MOLECULAR MULTIMODAL

MEMORIA PARA OPTAR AL GRADO DE DOCTORA

PRESENTADA POR

Irene Fernández Barahona

DIRECTORES

Fernando Herranz Rabanal

Juan Pellico Sáez

A mis padres

Agradecimientos

Me gustaría empezar dando las gracias a mis supervisores, Dr. Fernando Herranz y Dr. Juan Pellico por haberme dado la oportunidad de empezar a aprender de ellos e introducirme en el mundo de la investigación como alumna en prácticas hace ya unos cuantos años y por haber aceptado ser mis directores de tesis. Gracias por vuestro tiempo y paciencia durante todo este tiempo.

También a la Dra. Puerto Morales, la Dra. Lucía Gutiérrez y al Dr. Sabino Veintemillas-Verdaguer por su generosa y ayuda desinteresada.

Al Dr. Jesús Ruiz-Cabello por su ayuda con los experimentos de MRI.

Al personal técnico de la Unidad de Imagen Avanzada del CNIC por su ayuda en los experimentos de PET.

Al Dr. Jacob Fog Bentzon por proporcionar los modelos animales de aterosclerosis.

A toda la Unidad de Aplicaciones Médicas de las Radiaciones del CIEMAT por haberme acogido en su laboratorio como a una más del grupo. Gracias en especial a Dr. Miguel Ángel Morcillo, Dr. Marta Oteo y Marta Ibáñez y Rocío Santacruz por vuestra ayuda.

A María, Carlos y Adri por los buenos ratos en CNIC. A Laura por toda su ayuda en el IQM.

Published content

The following publications are included in this thesis:

Manuscript 1:

Irene Fernández-Barahona, Jesús Ruiz-Cabello, Fernando Herranz, Juan Pellico. Synthesis of ^{68}Ga Core-doped Iron Oxide Nanoparticles for Dual Positron Emission Tomography /(T_1)Magnetic Resonance Imaging. *Journal of Visualized Experiments*, 141, e58269, doi:10.3791/58269. **2018**

Manuscript 2:

Irene Fernández-Barahona, Lucía Gutiérrez, Sabino Veintemillas-Verdaguer, Juan Pellico, María del Puerto Morales, Mauro Catalá, Miguel A. del Pozo, Jesús Ruiz-Cabello, Fernando Herranz. Cu-Doped Extremely Small Iron Oxide Nanoparticles with Large Longitudinal Relaxivity: One-Pot Synthesis and in Vivo Targeted Molecular Imaging. *ACS Omega*, 4 (2), 2719-2727, doi:10.1021/acsomega.8b03004. **2019**

Manuscript 3:

Juan Pellico*, **Irene Fernández-Barahona***, Jesús Ruiz-Cabello, Lucía Gutiérrez, María Muñoz-Hernando, María J. Sánchez-Guisado, Irati Aiestarán Zelaia, Lydia Martínez-Parra, Ignacio Rodríguez, Jacob Benzton, Fernando Herranz. HAP-multitag, a PET and positive MRI contrast nanotracer for the longitudinal characterization of vascular calcifications in atherosclerosis. *ACS Applied Materials & Interfaces*, 13 (38), 45279-45290, doi:10.1021/acsami.1c13417. **2021**

Other publications not included in this thesis:

Marzia Marciello, Juan Pellico, **Irene Fernández-Barahona**, Fernando Herranz, Jesus Ruiz-Cabello, Marco Filice. Recent advances in the preparation and application of multifunctional iron oxide and liposome-based nanosystems for multimodal diagnosis and therapy. *Interface Focus*, 6 (6), 20160055, doi:10.1098/rsfs.2016.0055. **2016**

Juan Pellico, Jordi Llop, **Irene Fernández-Barahona**, Riju Bhavesh, Jesús Ruiz-Cabello, Fernando Herranz. Iron Oxide Nanoradiomaterials: Combining Nanoscale Properties with Radioisotopes for Enhanced Molecular Imaging. *Contrast Media & Molecular Imaging*, 2017, 1549580, doi:10.1155/2017/1549580. **2017**

Juan Pellico, Jesús Ruiz-Cabello, **Irene Fernández-Barahona**, Lucía Gutiérrez, Ana V. Lechuga-Vieco, José A. Enríquez, M. Puerto Morales, Fernando Herranz. One-step fast synthesis of nanoparticles for MRI: Coating chemistry as the key variable determining positive or negative contrast. *Langmuir*, 33 (39), 10239-10247, doi:10.1021/acs.langmuir.7b01759. **2017**

Juan Pellico, Ana V. Lechuga-Vieco, Elena Almarza, Andrés Hidalgo, Cristina Mesa-Núñez, **Irene Fernández-Barahona**, Juan A. Quintana, Juan Bueren, José A. Enríquez, Jesús Ruiz-Cabello, Fernando Herranz. In vivo imaging of lung inflammation with neutrophil-specific ^{68}Ga nano-radiotracer. *Scientific reports,* 7, 13242, doi:10.1038/s41598-017-12829-y. **2017**

Irene Fernández-Barahona, María Muñoz-Hernando, Juan Pellico, Jesús Ruiz-Cabello, Fernando Herranz. Molecular Imaging with ^{68}Ga Radio-Nanomaterials: Shedding Light on Nanoparticles. *Applied Sciences*, 8 (7), 1098, doi:10.3390/app8071098. **2018**

Irene Fernández-Barahona, María Muñoz-Hernando, Fernando Herranz. Microwave-Driven Synthesis of Iron Oxide Nanoparticles for Molecular Imaging. *Molecules*, 24 (7), 1224, doi:10.3390/molecules24071224. **2019**

Juan Pellico, **Irene Fernández-Barahona**, Marina Benito, Ángel Gaitán-Simón, Lucía Gutiérrez, Jesús Ruiz-Cabello, Fernando Herranz. Unambiguous detection of atherosclerosis using bioorthogonal nanomaterials. *Nanomedicine: Nanotechnology, Biology and Medicine*, 17, 26-35. doi:10.1016/j.nano.2018.12.015. **2019**

José M. Adrover, Juan Pellico, **Irene Fernández-Barahona**, Sandra Martín-Salamanca, Jesús Ruiz-Cabello, Andrés Hidalgo, Fernando Herranz. Thrombo-tag, and in vivo formed nanotracer for the detection of thrombi in mice by fast pre-targeted molecular imaging. *Nanoscale*, 12 (45), 22978-22987, doi:10.1039/D0NR04538A. **2019**

Irene Fernández-Barahona, María Muñoz-Hernando, Jesús Ruiz-Cabello, Fernando Herranz, Juan Pellico. Iron Oxide Nanoparticles: An Alternative for Positive Contrast in Magnetic Resonance Imaging. *Inorganics*, 8 (4), 28. doi:10.3390/inorganics8040028. **2020**

Yilian Fernández-Alonso, Gorka Salas, **Irene Fernández-Barahona**, Fernando Herranz, Cordula Grüttner, Jesús Martínez de la Fuente, María del Puerto Morales, Lucía Gutiérrez. *Particle & Particle Systems Characterisation*, 37 (7), 2000032, doi:10.1002/ppsc.202000032. **2020**

Olaia Martí-Marí, Belén Martínez-Gualda, **Irene Fernández-Barahona**, Alberto Mills, Rana Abdelnabi, Sam Noppen, Johan Neyts, Dominique Schols, María-José Camarasa, Fernando Herranz, Federico Gago, Ana San-Félix. Organotropic dendrons with high potency as HIV-1, HIV-2 and EV-A71 cell entry inhibitors. European Journal of Medicinal Chemistry, 237, 114414. doi:10.1016/j.ejmech.2022.114414. **2022**

Summary

The development of hybrid probes for multimodal molecular imaging is changing the diagnosis and characterisation of complex pathologies. The fusion of the outstanding sensitivity of positron emission tomography (PET) and the excellent anatomical resolution of magnetic resonance imaging (MRI), provides an ideal combination of structural and anatomical information, which is key to expand the application of molecular imaging for the diagnosis of complex and multifactorial diseases.

Iron oxide nanoparticles (IONPs) have been traditionally used as negative (T_2) contrast agents, darkening tissues or areas in which they accumulate. However, in recent years there has been a great amount of research focusing on the production of IONPs for positive (T_1) contrast MRI. One of the most appealing properties that nanoparticles usually offer is the possibility of tailoring their synthesis and functionalisation to obtain probes that generate or enhance the signal in more than one imaging modality, via incorporation of moieties in the core or the surface of the nanoparticle.

In this thesis, we developed a novel microwave-assisted method for the synthesis of IONPs core-doped with the positron emitter ^{68}Ga and with relaxometric properties suitable for hybrid T_1 MRI/PET imaging. Full characterisation revealed optimal radiochemical properties for PET imaging and excellent relaxometric properties for T_1 MR imaging, demonstrating that the combined use of nanotechnology and radiochemistry can render an innovative tool for the dual imaging of biological processes *in vivo*.

Furthermore, in an attempt to improve the relaxometric properties of our IONPs, we synthesised iron oxide nanoparticles doped with different amounts of copper. This resulted in three copper-doped samples with different relaxometric properties and hence, contrast capabilities. Further MR angiography in mice revealed an outstanding candidate for T_1 MRI, having relaxometric properties and contrast capabilities ameliorated with respect to undoped IONPs. In addition, this copper-doped nanoparticle sample was successfully vectorised into tumours by the bioconjugation of an integrin-binding peptide, providing a remarkable T_1 contrast enhancement in T_1-weighted MR imaging of tumour-bearing mice.

Finally, we used our ^{68}Ga core-doped IONPs to visualise microcalcifications in atherosclerotic plaque by PET and T_1-weighted MRI. To do this, we conjugated our ^{68}Ga core-doped IONPs with a bisphosphonate moiety to produce a surface conjugated bisphosphonate nanoparticle, named as HAP-multitag. Our nanotracer showed high affinity towards calcium salts both *in vitro* and *in vivo*, allowing us to spot microcalcifications in mice of different ages fed on high fat cholesterol diet and therefore, different plaque progression stages. To our knowledge, HAP-multitag is the first reported probe that enables not only the localisation of microcalcifications at the earliest stage but also the longitudinal characterisation of microcalcifications in atherosclerotic plaque *in vivo*.

Resumen

El desarrollo de sondas de imagen duales para imagen molecular es una posibilidad fascinante para el diagnóstico de enfermedades complejas. La fusión de la alta sensibilidad que ofrece la imagen de tomografía por emisión de positrones (PET por sus siglas en inglés) con la detallada información anatómica que ofrece la imagen por resonancia magnética (MRI por sus siglas en inglés) combina la obtención de imágenes con detallada información funcional y estructural, clave para extender el uso de la imagen molecular para el diagnóstico de enfermedades complejas y multifactoriales.

Las nanopartículas de óxido de hierro (IONPs por sus siglas en inglés) se han usado tradicionalmente para imagen por resonancia T_2, oscureciendo las áreas y órganos en los que se acumulan. Sin embargo, en los últimos años ha habido bastante investigación en la producción de IONPs para contraste positivo en imagen por resonancia magnética. Una de las propiedades más atractivas de las nanopartículas es la posibilidad de hacer una síntesis y funcionalización "a la carta" para obtener sondas que generan o ensalzan la señal en más de una modalidad de imagen, ya sea incorporando, por ejemplo, algún metal en su núcleo o biomolécula en su superficie.

En esta tesis hemos desarrollado un nuevo método de síntesis asistida por microondas para IONPs dopadas con el emisor de positrones ^{68}Ga en su núcleo y con propiedades relaxométricas idóneas para imagen dual T_1 MRI/PET. La caracterización completa de las muestras obtenidas revela un alto rendimiento de marcaje y estabilidad radioquímica, además de unas propiedades relaxométricas ideales para contraste positivo en MRI, demostrando que el uso combinado de la nanotecnología y la radioquímica produce una herramienta innovadora para la detección dual de procesos biológicos *in vivo*.

También hemos estudiado el efecto que tiene un metal dopante en el núcleo de las IONPs en sus propiedades relaxométricas y capacidades de contraste. En este caso usamos cobre y sintetizamos muestras con diferentes cantidades de dopaje. Obtuvimos tres muestras con capacidades de contraste y propiedades relaxométricas distintas. Llevamos a cabo experimentos *in vivo* de angiografía por resonancia magnética en ratón con las tres muestras que revelaron que nuestras nanopartículas son un candidato excelente para T_1 MRI, mostrando unas propiedades relaxométricas y capacidad de contraste mejoradas con respecto a las IONPs sin dopar. Esta muestra dopada con cobre se dirigió a tumores mediante la conjugación de un péptido que se une a integrinas, obteniendo un excelente contraste para la detección de tumores en ratones por T_1 MRI.

Finalmente, usamos nuestras IONPs para visualizar microcalcificaciones en placa de aterosclerosis usando PET y T_1-MRI. Para ello funcionalizamos estas nanopartículas con un bisfosfonato, creando HAP-multitag. Este nanoradiotrazador presenta una gran afinidad por las sales de calcio tanto *in vitro* como *in vivo*, permitiendo la localización de microcalcificaciones en ratones de diferentes edades y por lo tanto con estados de progresión ateroscleróticas distintos. Hasta donde sabemos, HAP-multitag es la

primera sonda que no solo permite la localización de las microcalcificaciones en su estado más temprano, sino que también nos ha permitido caracterizar la aterosclerosis longitudinalmente usando las microcalcificaciones como biomarcador *in vivo*.

List of abbreviations

AC: Alternating current

BP: Bisphosphonate

DLS: Dynamic Light Scattering

EDX: Energy Dispersive X-Ray Spectroscopy

FTIR: Fourier Transform Infrared Spectroscopy

HAP: Hydroxyapatite

ICP-MS: Inductively Coupled Plasma Mass Spectroscopy

IONP: Iron Oxide Nanoparticle

LDL: Low Density Lipoprotein

MRA: Magnetic Resonance Angiography

MRI: Magnetic Resonance Imaging

M_s: Saturation Magnetisation

MW: Microwave

NP: Nanoparticle

PET: Positron Emission Tomography

r_1: Longitudinal relaxivity value

r_2: Transversal relaxivity value

STEM-HAADF: Scanning Transmission Electron Microscopy – High-Angle Annular Dark Field Imaging

TGA: Thermogravimetric Analysis

XRD: X-Ray Diffraction

Index

Published and submitted content

Summary

Resumen

List of abbreviations

1. Introduction **1**

1.1 Molecular Imaging 1

1.2 Nanotechnology and nanomedicine 6

1.3 Iron oxide nanoparticles for multimodal molecular imaging 10

2. Hypothesis and objectives **12**

3. Main contributions and discussion **13**

3.1 Microwave assisted synthesis of citrate-coated ^{68}Ga core-doped iron oxide nanoparticles (Article 1) 13

3.2 Copper-doped extremely small iron oxide nanoparticles with large longitudinal relaxivity: applications in MRA and targeted T_1-MRI (Article 2) 21

3.3 Early multimodal diagnosis of atherosclerosis: HAP-multitag, a PET and T_1-MRI contrast nanotracer for the longitudinal characterisation of vascular calcification in atherosclerosis (Article 3) 31

4. Conclusions **46**

5. Bibliography **48**

1. Introduction

1.1 Molecular Imaging

Molecular imaging is playing a key role in the diagnosis and evaluation of treatments owing to the advance in fields like chemistry, molecular biology and imaging technologies. It is defined as the visualisation, characterisation and measurement of biochemical and biological processes or events at cellular and molecular levels in living systems in a non-invasive manner.[1] These events can be as simple as localising a cell population or as complex as studying transcription of a set of genes or intracellular protein interactions. Molecular imaging aims to provide deeper understanding of fundamental biological processes by easing the connection between structure and function. These processes might facilitate disease characterisation as the levels of specific molecular targets are often an indicator of the presence of a disease. Molecular imaging is also essential in drug validation, as well as in treatment response monitorisation. It enables the longitudinal monitoring of patients, allowing long-term surveillance that sheds light on the causes of whether a certain treatment is working as expected, which paves the way to a more personalised approach to medicine.

The majority of molecular imaging modalities involve the use of a molecular probe, usually a small molecule, that is administered to the living subject. This molecular probe must not disturb the metabolism of the living subject, nor cause acute or chronical toxicity. This molecular probe will bind a target that must be carefully selected, as the abundance and specificity of this target will drive the appropriateness of the molecular probe to reflect the presence of the disorder under evaluation. The molecular probe is typically composed by a targeting vector, usually a biomolecule that provides specificity towards the selected molecular target and a signalling component, responsible for generating or enhancing the signal detected by the chosen imaging modality.[2] Sometimes a linker may be included to bind these two components of the probe.

There is a wide range of imaging techniques: nuclear imaging (PET, SPECT), computed tomography (CT), magnetic resonance imaging (MRI), magnetic particle imaging (MPI), optical imaging and ultrasound, among others. These are commonly classified as anatomical (CT, MRI and ultrasound) or functional imaging techniques (nuclear imaging, MPI, MRI, and optical imaging) (Figure 1.1). Anatomical imaging techniques provide a detailed map of the anatomy of the subject and are able to track structural and morphological changes and the presence of an abnormality. Functional imaging techniques are used to visualise changes in metabolism or organ/tissue function in a highly sensitive manner, for this reason they are used to visualise changes in metabolism or organ/tissue function.[3] Both anatomical and functional techniques are usually combined to obtain the best of both worlds: elevated spatial resolution of the anatomical imaging techniques and the high sensitivity of the functional ones. For this reason, it is common to find PET scanners combined with CT or MR magnets to perform multimodal imaging (PET/CT or PET/MRI). This introduction will then focus on PET and MRI as they are the main techniques used throughout this thesis.

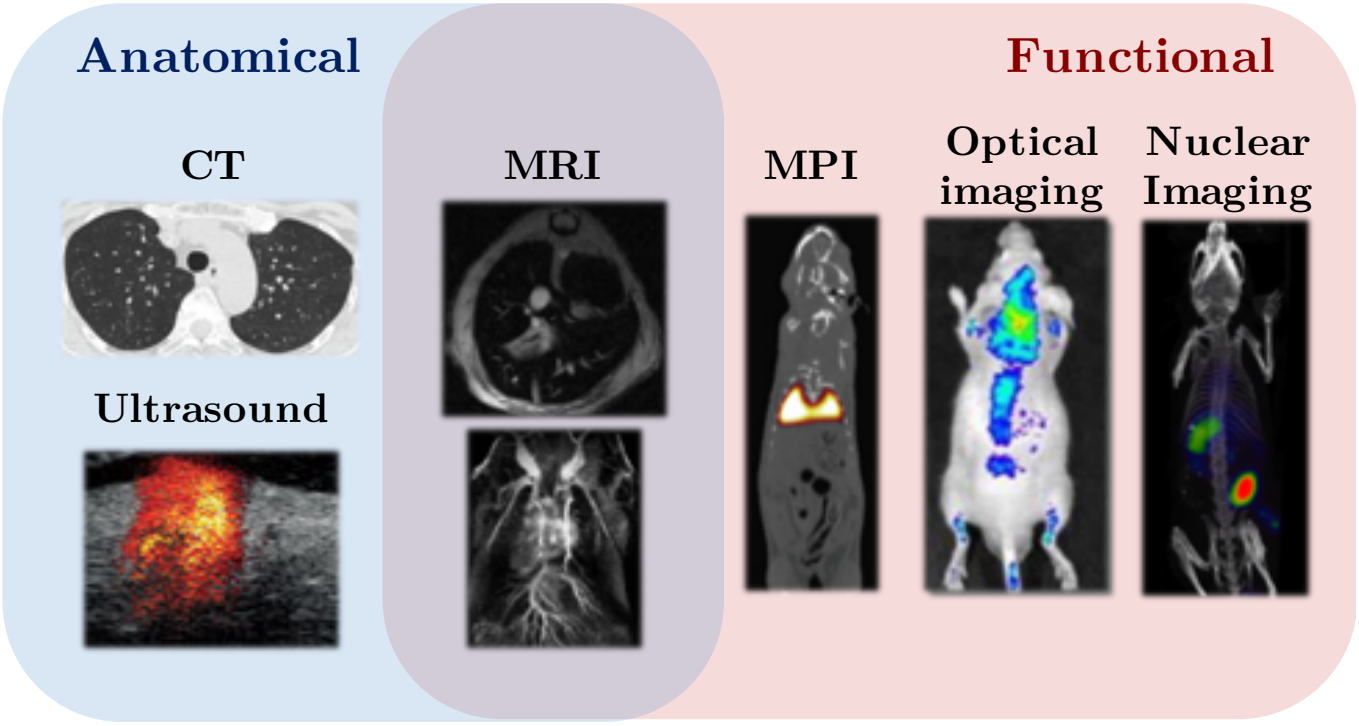

Figure 1.1: Anatomical and functional imaging modalities. CT image adapted from Hansel *et al.*, [4] ultrasound image adapted from Evertsson *et al.*,[5] MRI images adapted from Pellico *et al.*,[6] MPI image adapted from Zheng *et al.*,[7] optical imaging image adapted from Zheng *et al.*,[8] nuclear imaging image adapted from Pellico *et al.*[9]

1.1.1 PET imaging

PET imaging is based on the detection of positron emitting radioisotopes. A positron is the antiparticle of an electron that has the exact same mass and opposite charge.[10] Nuclei with this type of decay present protons in excess that make them unstable and therefore emit a positron to reach a stable state. As the emitted positron has kinetic energy, it travels through space colliding with electrons in surrounding tissues. The total loss of energy occurs when the positron is combined with an electron in a process called annihilation. By virtue of energy and momentum conservation laws, this process yields two gamma photons of 511 keV that travel in opposite directions. In PET, these two 511 keV gamma photons are detected by scintillation detectors and processed by photomultiplier tubes both arranged in the form of ring surrounding the imaged subject.[10] This detects an annihilation event occurring along the line that joins these two orthogonal crystal detectors. The data is then processed and reconstructed to yield a final tomographic image, providing information about the location and concentration of the positron emitter within the imaged subject (Figure 1.2). This technique offers an outstanding sensitivity (of up to picomolar tracer concentrations), enabling the extraction of molecular, functional and metabolic information in a precise and quantitative manner, representing the main advantage with respect to other imaging techniques. Moreover, the main drawback of PET is the inherent low spatial resolution.[11] The discovery of this technique is closely related to the cyclotron discovery and subsequent construction in 1934. PET imaging demands expensive equipment, being the reason for its modest application in the clinic in its early days. The development of new and diverse tracers and the

development of hybrid PET/CT scanners has turned this around and PET is now a key tool in the diagnosis of numerous conditions such as oncology,[12–14] cardiovascular diseases,[15–17] and neurodegenerative disorders[18–20] among many others.

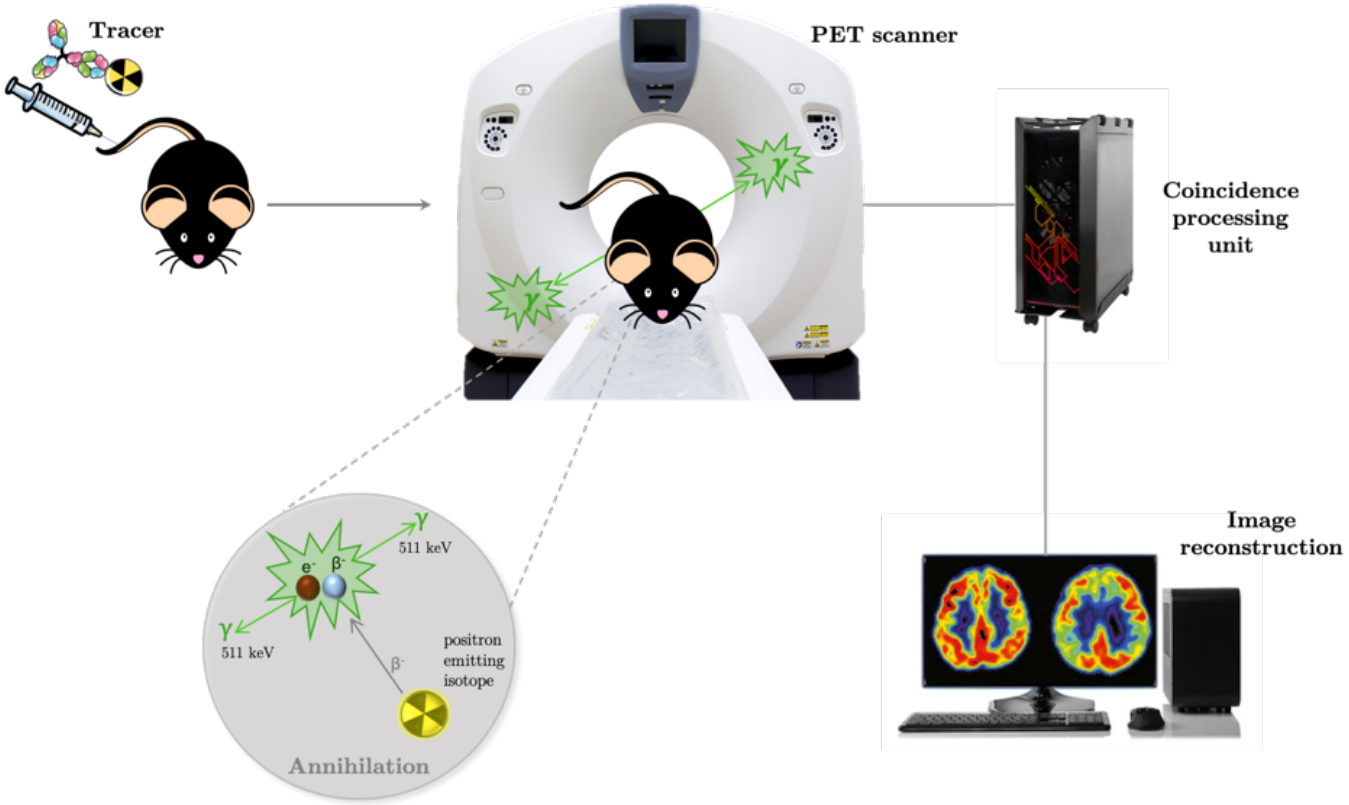

Figure 1.2: PET imaging process. Positron emitter (tracer) injection in living subject, positron annihilation, 511 keV gamma ray detection and data processing to render the final PET image.

Imaging a molecular target using PET requires a careful radioisotope and target selection.[3] Two main issues must be taken into account when selecting these. To start with, the half-life of the radioisotope must match the time the tracer takes to bind the target or to cause a metabolic effect. Secondly, the radiolabelling process, *i.e.*, the chemistry employed to unify the radioisotope with the selected molecule to bind a certain target must also be considered.

The half-life of a radioisotope is defined as the amount of time it takes for one-half of the radioactive isotope to decay to a stable isotope; in other words, the time it takes for a radioisotope to halve its initial activity. This parameter is constant and independent from initial radioisotope amount and conditions. There is a broad selection of radioisotopes to choose from depending on the final imaging application. The most common PET isotopes are ^{11}C, ^{13}N, ^{15}O, ^{18}F, ^{64}Cu, ^{62}Cu , ^{68}Ga, ^{76}Br, ^{89}Zr and ^{124}I. A cyclotron is required for

the production of the vast majority of these isotopes. However, radioisotopes such as ^{82}Rb, ^{62}Cu and ^{68}Ga can be easily produced in benchtop generators.

Indisputably, the most used in the clinic is ^{18}F in the form of 2-deoxy-2-[fluorine-18]fluoro-D-glucose ([^{18}F]FDG), a glucose analogue in which the 2-carbon hydroxyl group has been substituted for a ^{18}F atom.[3] This tracer provides functional information about metabolic abnormalities. For instance, cancer cells present increased glycolytic metabolism, hence [^{18}F]FDG uptake is significantly higher than in normal cells. For this reason it is routinely used in the clinic in the detection of numerous cancer types.[21–23]

^{11}C is another PET isotope commonly applied in the clinic. In this case, ^{11}C is usually covalently bonded to biomolecules such as choline, methionine and sodium acetate for different purposes. ^{11}C-choline has been used in the detection of prostate cancer,[24] multiple myeloma[25] and cirrhosis.[26] ^{11}C-methionine is employed in several brain tumour types.[27,28] ^{11}C-acetate has been of utility in the diagnosis of lymphoma types,[29] prostate cancer[30] and liver steatosis.[31]

^{89}Zr is a relevant radioisotope in PET imaging as its relatively long half-life ($t_{1/2}$ = 78.4 hours), allows long circulating species tracking when radiolabelled with it. Monoclonal antibodies present circulating times that span from hours to several days, making ^{89}Zr ideal for this purpose. ^{89}Zr-based tracers are based on chelating agents, which form stables complexes with ^{89}Zr. The most popular chelator for ^{89}Zr is deferoxamine (DFO). Antibodies such as bevacizumab, trastuzumab and cetuximab have been used in PET imaging of breast cancer and gliomas among other cancer types not only for diagnosis but also for immunotherapy.[32–34]

^{68}Ga is a PET emitter with a relatively short half-life (67.8 min) obtained from its parent radionuclide ^{68}Ge.[35] Its short half-life matches the pharmacokinetics of the vast majority of small molecules, making this radioisotope ideal for PET imaging of small biomolecules and peptides. The attractiveness of this radioisotope lies in its production. ^{68}Ga can be produced on site from a benchtop ^{68}Ge/^{68}Ga generator, discarding the need for a neighbouring cyclotron. Benchtop generators are designed to produce short-lived radionuclides from a parent long-lived pair (father isotope). Owing to the long half-life of ^{68}Ge ($t_{1/2}$ = 270.8 days), the life span of these generators is of several months. For this reason, ^{68}Ga offers an efficient and economical alternative to cyclotrons and reactors enables clinical PET studies in facilities where cyclotrons are unavailable or complicated to access.

1.1.2 Magnetic Resonance Imaging

Magnetic resonance imaging (MRI) is a non-invasive imaging technique used to detect multiple conditions and diseases.[36–42] Its functioning relies on the magnetic moment of isotopes with odd atomic numbers as for instance ^{13}C, ^{19}F, ^{31}P and water protons (^{1}H) present in the different tissues of the human body.[43] These align forming a parallel or anti-parallel configuration upon exposure to an external magnetic field, generating a net magnetisation that is aligned with the external magnetic field applied. A radiofrequency pulse is then applied at the isotope's resonance frequency and perpendicular to the external magnetic field's direction

(Figure 1.3a). This is done to alter the direction of the magnetisation vector. The system is then allowed to return back to equilibrium. This is measured by the transversal and longitudinal relaxation phenomena.

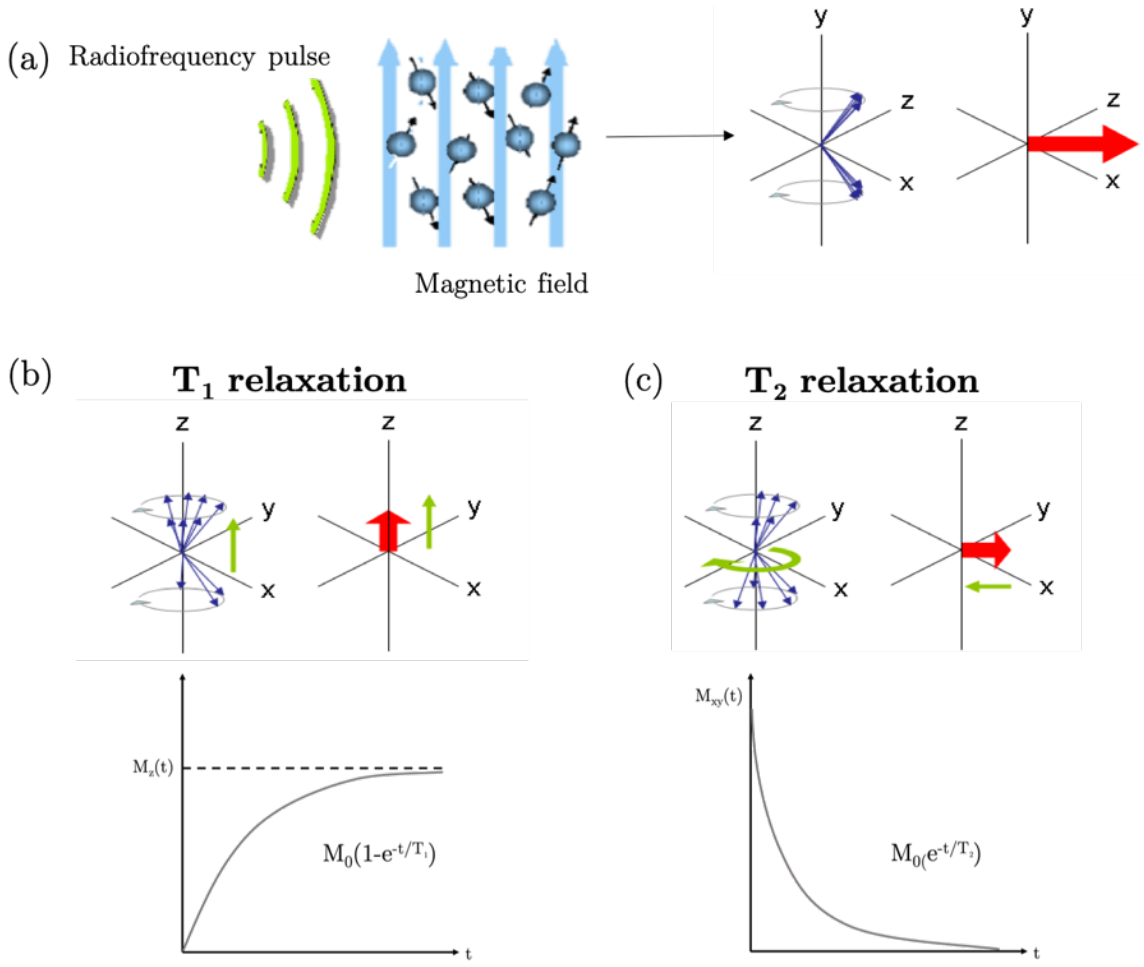

Figure 1.3: (a) Basis of nuclear magnetic resonance, (b) T_1 relaxation mechanism, and (c) T_2 relaxation mechanism. After adequate data collection enabled by magnetic resonance gradients and posterior processing, an image is reconstructed making use of a discrete Fourier Transform.[44]

The term relaxation is used to describe the process by which the system returns to equilibrium after the radiofrequency pulse. Relaxation merges two mechanisms: longitudinal (T_1) and transversal (T_2) relaxation times. T_1 determines the speed at which longitudinal magnetisation is recovered (Figure 1.3b) and T_2 measures how fast the transversal magnetisation (originated by the radiofrequency pulse) is lost (Figure 1.3c).

In vivo, when the proton density is similar, contrast between adjacent tissues is low and often requires a contrast agent in order to better discriminate the area of interest. Contrast agents in MRI are substances that induce a change in the local magnetic field of their surrounding protons with subsequent modification of the local relaxation times.[45] Contrast agents reducing T_1 relaxation time produce a brightened image (Figure 1.4a, MR angiography in which aorta, carotids and heart chambers of a mouse are clearly visible) and T_2 contrast agents produce a darkening of the tissues in which they accumulate (Figure 1.4b, T_2-weighted

MRI of the liver of a mouse). The capacity of changing these relaxation times is measured by the relaxivities, magnitude commonly used to evaluate the suitability of a contrast agent. These relaxivities are calculated by plotting change in relaxation rate ($1/T_1$ and $1/T_2$) at different contrast agent concentrations. The slopes of the best fit line joining theses points represent r_1 and r_2 respectively.

Traditional T_1 contrast agents are mainly gadolinium-based.[46,47] Gadolinium is a lanthanide metal with paramagnetic properties and its free ionic form (Gd^{3+}) is extremely toxic. For this reason, Gd^{3+} is chelated with suitable ligands that are able to form stable complexes with it. The chemistry of this chelate (linear or macrocyclic) determines the risk of transmetallation and potential toxicity. It is well-known that gadolinium-based chelates show significant toxicity in conditioned or diseased patients; importantly in patients with renal disfunction.[48,49] Moreover, gadolinium-based contrast agents often have a small molecular weight and usually extravasate rapidly after injection, excluding them from applications requiring long circulating times.

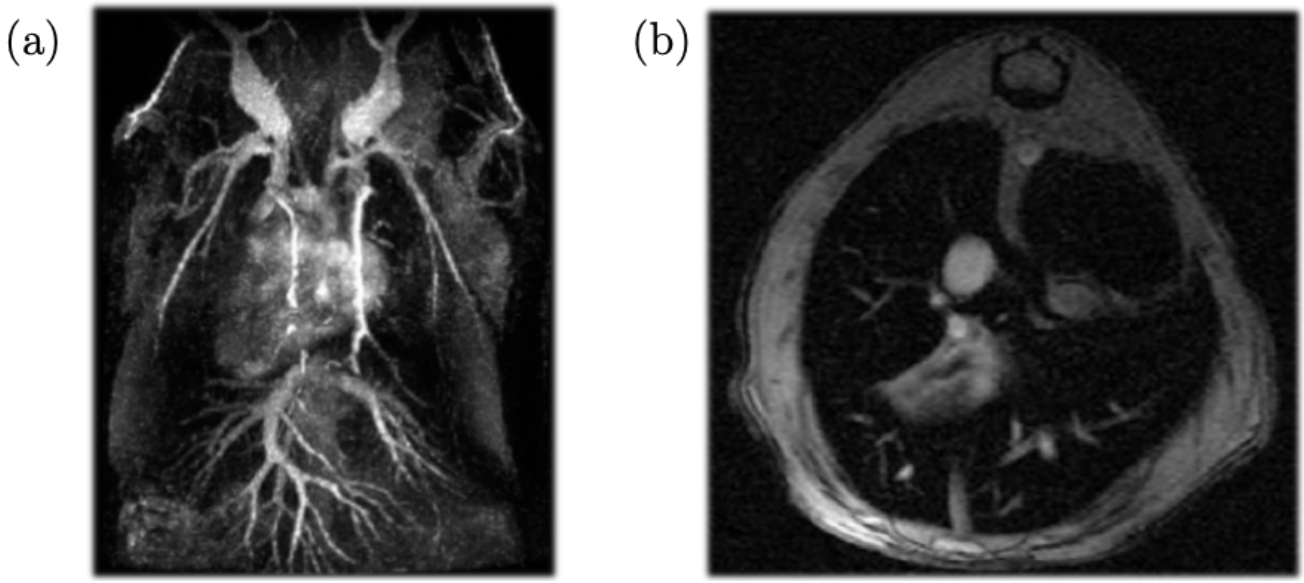

Figure 1.4: (a) T_1-weighted MR image, and (b) T_2-weighted MR image.

These toxicity and short circulation time issues could be solvented by the use of nanoparticle-based T_1 MRI contrast agents. Nanomaterials present unique properties owing to their size. At the nanoscale, quantum effects dominate material behaviour, conferring NPs size-dependent behaviour as well as an increased reactivity due to their large surface-to-volume ratio, as we will see in the next section.

1.2 Nanotechnology and nanomedicine

1.2.1. Nanotechnology

Nanotechnology is a blend of scientific, engineering and technological disciplines which has impacted on global concerns such as energy, environment, information technology, chemical and healthcare. It deals with the creation and application of materials, devices and systems at atomic, molecular and supramolecular levels

of dimensions lying in the range of 0.1 to 100 nm (1 nm = 10^{-9} m) (Figure 1.5). The US National Nanotechnology Initiative defined nanotechnology, in year 2000, as "the study of materials and systems whose structures and components exhibit unique physical, chemical, and biological properties in fundamentally new and useful ways due to their nanoscale size".[50]

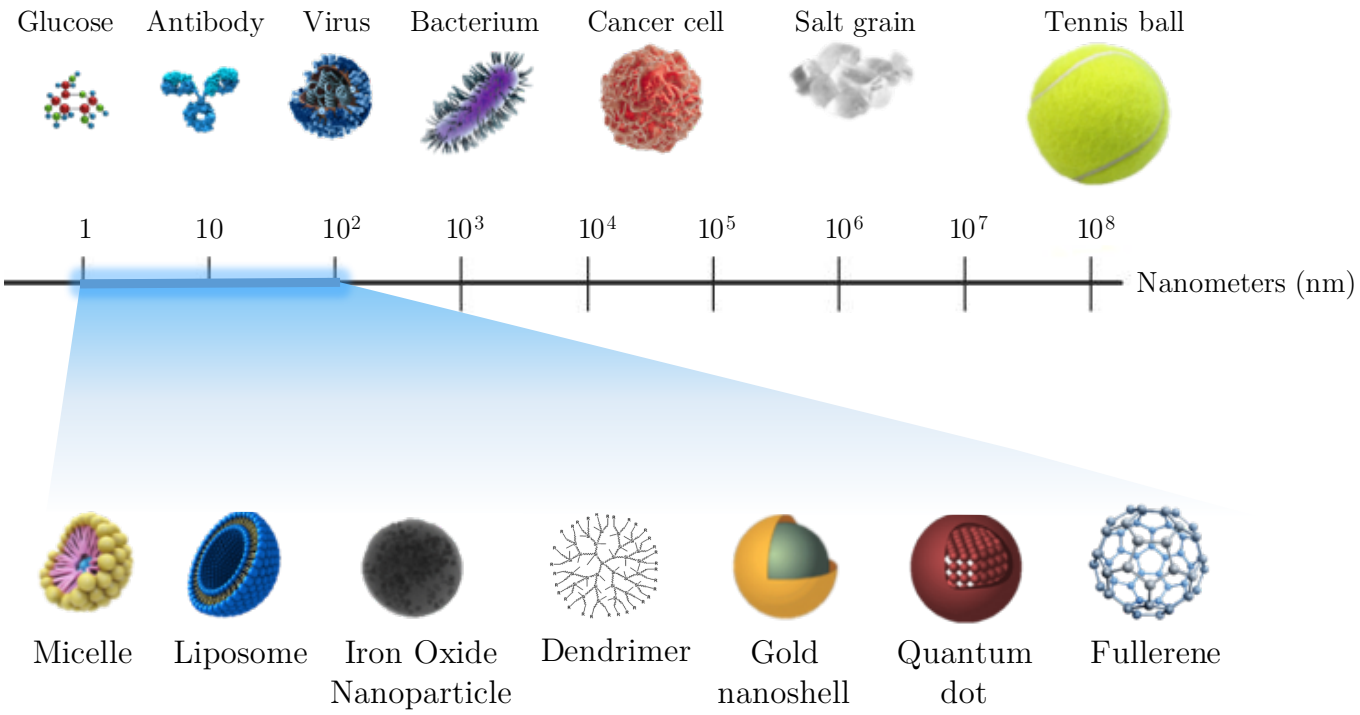

Figure 1.5: Comparison of the nanoscale to other biomolecules and elements.

A nanoparticle (NP) is defined as a chemical compound in the mesoscopic scale, with at least one dimension less than 100 nm with new or improved properties, due to its nanoscale size, with respect to the bulk material. There are numerous examples of these: gold NPs, iron oxide NPs, quantum dots, polymeric NPs, upconverting NPs and many others. Chemical and physical properties of materials are altered at the nanoscale. There are two main reasons accounting for these changes: quantum effects and increased surface-to-volume ratio. In this scale range, quantum effects dominate matter behaviour, hence properties are size-dependent. Fluorescence, electrical conductivity, chemical reactivity and melting point change with particle size. Descriptive examples of this effect are quantum dots (QDs), whose optoelectronic properties change with size. As size increases, so does emission wavelength. This enables a wide scope of tailorable properties for NPs according to desired applications. The second important reason is the increase in surface-to-volume ratio. Surface area per volume increases, which enables a greater amount of material to get in touch with surrounding media. This results in an increased reactivity, which makes their use as catalysts rather suitable. This is also of great help in NP functionalisation, as larger surfaces and higher reactivity will ease this purpose. Therefore, nanoparticles can be conjugated with different chemical species and high yield giving high ligand pay-loads, difficult to obtain otherwise. Finally, a large surface will enable multifunctionalisation

and addition of multiple molecules in one-pot reaction, extending its use in distinct applications with the same nanoparticle (imaging techniques, specific targeting or drug delivery).

1.2.2 Nanomedicine

Nanomedicine is defined by the National Institute of Health as an offshoot of nanotechnology that seeks to apply the discipline to diagnosis, monitoring, treatment and control of biological systems.[51] Nanotechnology offers the possibility of dealing with biological problems in a revolutionary way. For example while conventional procedures, such as surgery, radiotherapy or chemotherapy aim to eliminate damaged cells more rapidly or in larger quantities than healthy cells; nanomedicine only pursuits damaged cell elimination or repair by recognition of specific targeted cells, leaving healthy cells untouched.[52–54] Furthermore, it endows the possibility of combining diagnostics and therapy, designated as "theranostics".[55,56] Applications include the combination of molecular imaging probes and targeted drug delivery. There are numerous nanostructures valid for these purposes: liposomes, dendrimers, nanobots, nanotubes and nanoparticles. Amongst all kinds, and iron oxide nanoparticles are arguably one of the most popular choices for biomedical purposes. They have been used in many clinical trials and approved by FDA for several applications.[57,58] These NPs present specific physicochemical properties which make them an exceedingly interesting topic of study and therefore, will be the main subject of study throughout this thesis.

1.2.3 Iron oxide nanoparticles (IONPs)

Iron oxide nanoparticles are biocompatible and minimally toxic. They are typically composed of an iron oxide core and a coating or surfactant. The core is usually composed of magnetite ($(Fe^{II}Fe^{III}_2)O_4$) and/or maghemite (Fe_2O_3). These are ternary iron oxides with cubic inverse spinel structure. Due to the aforementioned increased surface-to-volume ratio, these NPs also present high surface energy, which they try to minimise with subsequent aggregation. To prevent this, nanoparticles are stabilised with a surface coating that provides colloidal stability and plays a key role in the physicochemical properties and eventually in the *in vivo* pharmacokinetics. It will also enable NP functionalisation, with peptides, proteins, antibodies or other imaging modality tracer; hence its choice is crucial. The coating is generally composed of organic molecules, such as polymers and small molecules and must present affinity towards the core surface in order to ensure strong bonding and stability. In addition to their biocompatibility, IONPs exhibit another compelling property of great relevance for biomedical applications: superparamagnetic behaviour due to their nanometric size, albeit bulk iron oxides usually behave as a ferromagnetic material. Ferromagnetic materials present multiple magnetic domains that may align under the influence of an external magnetic field, yielding large saturation magnetisation values. However, when the external magnetic field is removed, the material still presents remanent magnetisation, showing magnetic hysteresis loops (Figure 1.6).[59]

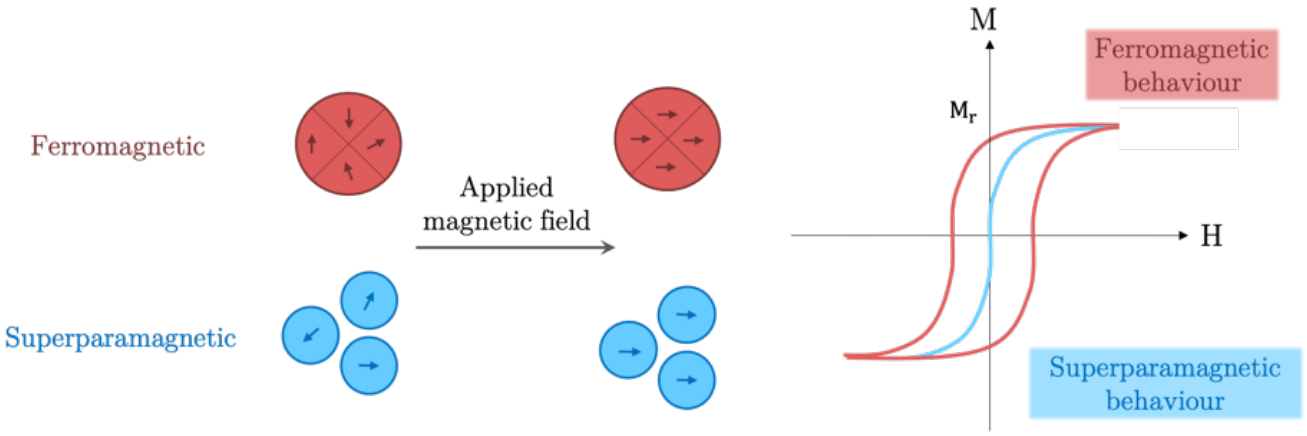

Figure 1.6: Ferromagnetic and superparamagnetic behaviours. H represents external magnetic field applied, M magnetisation and M_r remanent magnetisation.

Nanometric size induces a mono-domain behaviour, allowing magnetic moment alignment upon exposure to the external applied magnetic field. However, in this case the absence of the external magnetic field, leaves magnetic moments randomly oriented, leading IONPs to behave as non-magnetic materials. Therefore, IONPs behave as a paramagnetic material but reach saturation magnetisation values comparable to the of ferromagnetic ones (Figure 1.6). This characteristic, present in the nanoscale, has impulsed the use of IONPs in diverse applications in biomedicine, such as magnetic hyperthermia,[60,61] drug delivery,[62,63] sensors,[64,65] magnetic particle imaging[66,67] and especially as contrast agents for magnetic resonance imaging.[68,69] Its use as contrast agent in magnetic resonance imaging (MRI) is undoubtedly within the most relevant.

As contrast agents for MRI, they have been traditionally used as T_2 contrast agents, due to their superparamagnetic behaviour and large magnetic moment, which is converted into large transversal relaxivity values and a dark signal *in vivo*.[70,71] They have been used in many applications including tumour and myocardial infarction detection.[72–74] As their main elimination route is via the liver and spleen to posteriorly be degraded to become part of the iron reservoir of the patient, they have also been used for diagnosis of diseases related to the liver.[75] Until a few years ago, there were several commercial iron oxide formulations used as T_2 contrast agents: Endorem®, Feridex®, Resovist®, Combidex®, Sinerem®, Clariscan®, and Lumirem® are some examples of them. Nevertheless, the production of many of them have been discontinued for diverse reasons.[76,77] The dark, negative signals produced by T_2 contrast agents, complicate the diagnosis of certain diseases and pathologies. Organs such as the lungs and pathologies like atherosclerosis, among others, naturally darkened in MR images. Hence if the probe generates a dark signal in an already dark background image, discrimination of condition, disease or organ is confusing and complex. For this reason, in recent years, there has been a great amount of research focusing on the development of IONPs for T_1- or positive-contrast. Extremely small IONPs, behaving as a paramagnetic rather than a superparamagnetic material providing positive contrast are a good choice. By virtue of their extremely small core, most Fe^{3+} ions are on the surface of the nanoparticle core, having 5 unpaired electrons each. A good T_1 contrast agent

must present a large longitudinal relaxivity value (r_1), and a low transversal relaxivity (r_2) value that yields a small r_2/r_1 ratio. This low r_2/r_1 ratio ensures the T_1 MRI effect dominates over the T_2 effect in the relaxation process so positive contrast can be obtained.

The synthetic method selected is crucial for IONPs to have the desired features. The general IONP synthetic method can be classified as aqueous and non-aqueous. Aqueous methods include coprecipitation, hydrothermal synthesis and sol-gel synthesis. These methods yield rather amorphous iron oxide cores but physiologically stable in a single step. Non-aqueous methods however, generate iron oxide cores with significantly better crystallinity and size homogeneity but in organic solvents, meaning a further step is needed to stabilise the nanoparticles in physiological media before they can be used for *in vivo* applications.

Microwave-assisted synthesis of IONPs is a relatively novel method, nevertheless it has been used in a great number of NP syntheses. Microwave-assisted synthesis offers two key advantages in IONP synthesis over traditional methods: a significantly lower reaction time and a stable and homogeneous heating. The dielectric heating prevents temperature gradients often occurring in traditional methods, yielding homogeneous nanoparticle samples and increasing the reproducibility of the synthesis. This method offers flexibility that enables the synthesis in a wide variety of synthetic conditions to produce nanoparticles with multiple shapes, sizes and hence, different physicochemical and magnetic properties. Reaction times span from a few seconds to several hours. Using this method, our group obtained in 10 minutes at 100 ºC, iron oxide nanoparticles with small cores of around 2.5 nm coated with (FTIC)-dextran and dextran 6kDa as organic coating and decent relaxometric properties for T_1-weighted MRI (r_1=5.7 $mM^{-1}s^{-1}$ and r_2/r_1=3.8 at 1.5 T) .[9,78] Later on, our group improved the approach using sodium citrate instead of dextran as coating, achieving with the same reaction time and tuning temperature to 120 ºC a r_1 value of 11.9 $mM^{-1}s^{-1}$ with a r_2/r_1 ratio of 1.9.[6] The possibility of combining the alluring properties of IONPs for T_1-weighted MRI with the other imaging modalities is eased by the tailorability of this microwave-drive synthesis.

1.3 Iron oxide nanoparticles for multimodal molecular imaging

Using nanoparticles in PET imaging brings advantages to both the molecular imaging and nanomedicine fields. The most important ones are the pharmacokinetics and the multifunctionality nanoparticles offer. The pharmacokinetics of traditional (small molecule) PET tracers are frequently complicated to control. Incorporating the radioisotope into the IONP, the pharmacokinetics will be that of the nanoparticle, easily modifiable, and not that of the traditional tracer. Nanoparticles act as hosts to multifunctional probes, for example having the possibility of combining PET/fluorescence/MRI probes and targeting vectors in a single functionalised IONP. Furthermore, combined used of IONPs and PET emitters allow a fast, easy and reliable IONP quantitative whole-body biodistribution evaluation, certainly not possible to obtain otherwise. The combination of IONPs for T_1-weighted MRI and the clear signal offered by PET drove our group to inquire into the synthesis of multimodal PET/T_1-MRI IONPs using MW-assisted synthesis.

Two key issues must be considered when combining IONPs with a positron emitter: radioisotope choice and nanoparticle radiolabelling method. Regarding radioisotope selection, there are examples in the literature of IONPs radiolabelled with ^{64}Cu, ^{89}Zr, ^{124}I, ^{18}F, ^{11}C, and ^{68}Ga.[79–87] Among them, ^{68}Ga is a promising choice. As previously mentioned, its short half-life (67.8 min) matches the biodistribution time of IONPs and there is no need for a cyclotron, as it is produced in a benchtop generator. With respect to the radiolabelling strategy, surface labelling usually prevails. This can be done using a chelating ligand or taking advantage of the affinity of the radiometal towards the nanoparticle surface. Most examples in the literature include a chelating agent: 1,4,7,10-tetraazacyclododecane-1,4,7,10-tetraacetic acid (DOTA);[88] 1,4,7-triazacyclononane-1,4,7-triacetic (NOTA);[87,89] 1,4,7-triazacyclononane,1-glutaric acid-4,7-acetic acid (NODAGA);[90] and 2,3-dicarboxypropane-1,1-diphosphonic acid (DPD),[91] a tetradentate ligand. A chelator-free strategy was developed in 2014 by Madru *et al.*[86] However, this approach presents some major drawbacks such as high risk of transmetallation *in vivo*, low radiolabelling yields and lengthy protocols not suitable for short half-life radioisotopes.[82,92,93]

An alternative to the surface labelling is the incorporation of the radioisotope into the nanoparticle core. This strategy, denoted as core-doping, involves the incorporation of the radioisotope at the same time that the nanoparticle is synthesised. A careful radioisotope choice and correct synthesis protocol enables the incorporation of the radioisotope in the crystal structure of the IONP. This approach prevents the detaching of the radioisotope *in vivo*, conferring the nanotracer an excellent radiochemical stability. A key aspect is the synthetic method: time goes by and the radioisotope decays. A fast synthesis method is required, reason for which microwave-assisted synthesis is ideal to carry this radiolabelling method in a short reaction time.

There are some examples of core-doped IONPs in the literature: Zeng *et al.* radiolabelled IONPs with ^{111}In.[94] Weissleder *et al.* and Chouly *et al.* core-doped IONPs with ^{59}Fe to study the IONP pharmacokinetics and toxicity.[95,96] Cedrowska *et al.* core-doped IONPs with ^{225}Ac to combine radiotherapy and magnetic hyperthermia in breast cancer.[97] However, it was not until a few years ago when Wong e*t al.* applied a microwave-assisted synthesis for the production and core-doped radiolabelling of IONPs.[98] In this study, they managed to incorporate ^{64}Cu in the core of dextran-coated IONPs in 5 minutes for PET/T_2-MRI. Later, in 2016, our group developed ^{68}Ga core-doped IONPs in 10 minutes using microwave technology.[9] The radiolabelling yield obtained by our group in this study (93%) is almost three-fold the radiolabelling yield obtained in the ^{64}Cu incorporation to IONPs carried out by Wong *et al.*, that was 33%. This implies a significant improvement in the method, as in this study, microwave-assisted synthesis of ^{68}Ga core-doped IONPs was fast and with a high efficiency. As an example of the multiple potential applications of these nanoparticles, they were conjugated to an integrin-binding peptide and used *in vivo* to visualise tumours in mice by PET and T_1-weighted MRI.

Therefore, in view of these precedents, our approach during this thesis was to synthesise using microwave technology nanoradiotracers with improved relaxometric properties suitable for T_1-weighted MRI and PET.

2. Hypothesis and objectives

This thesis combines the use of nanotechnology and radiochemistry to synthesise iron oxide-based tracers for the diagnosis of different pathologies by molecular imaging.

We will use iron oxide nanoparticles as T_1 contrast agents for MRI and for PET imaging. For this, we will dope the core of IONPs with ^{68}Ga. This will enable multimodal imaging by PET and MRI. Furthermore, our IONPs will be doped with copper in their core to study how this affects their relaxometric properties.

We will synthesise the nanoparticles via a microwave-driven protocol that will allow a rapid and simple incorporation of dopant metals, with ^{68}Ga for their use as T_1 MRI/PET dual contrast agents and Cu to study its effect on relaxometric properties for T_1 MRI.

Once nanoparticles have been characterised, they will be functionalised with the corresponding biomolecule to study and detect biological phenomena *in vivo* by their use as tracer in PET and/or their contrast capability in MRI.

The main objectives of this thesis are:

1. To optimise the microwave-driven synthesis of iron oxide nanoparticles doped with ^{68}Ga for their use as dual T_1 MRI/PET contrast agents
2. Studying the effect of a dopant metal, copper, in the relaxometric properties and contrast capabilities of the iron oxide nanoparticles synthesised by microwave-assisted synthesis.
3. To study the physicochemical, magnetic and relaxometric properties of prepared nanoparticles.
4. The *in vivo* evaluation of the synthesised samples as probes in T_1-MRI and PET/T_1-MRI.
5. To use the newly produced nanoparticles for the early diagnosis and characterisation of atherosclerosis.

3. Main contributions and discussion

3.1 Microwave assisted synthesis of citrate-coated ^{68}Ga core-doped iron oxide nanoparticles (Article 1)

Among synthetic routes for T_1-IONPs, microwave (MW) eases the production of highly uniform samples in extremely short times, with higher reproducibility than other types of syntheses.[99–101] Our group previously synthesised an iron oxide-based radiotracer nanoplatform using a rapid and efficient procedure to integrate ^{68}Ga in the core of IONPs, preventing many drawbacks presented by traditional radiolabelling methods.[9] Dextran-coated iron oxide nanoparticles doped with ^{68}Ga in the core were successfully used to target $\alpha_v\beta_3$ receptors in tumours in a subcutaneous melanoma mouse model by PET and positive contrast MRI. For this, ^{68}Ga core-doped IONPs coated with dextran were functionalised with a cyclic RGD peptide.

Although dextran has been broadly used in IONP synthesis, we wanted to inquire into using other molecules to coat our ^{68}Ga core-doped IONPs. Avoiding problems associated to the intravenous injection of nanoparticles coated with a neutral surfactant molecule. Citric acid is a biocompatible short-chained tri-carboxylic acid molecule that coordinates with the NP surface upon one or two carboxylate moieties, leaving expose at least one carboxylic group that increase NP hydrophilicity and provide functional groups for further functionalisation.[102,103] This molecule has been widely used in the stabilisation of NPs for biomedical applications, as it provides colloidal stability and homogeneity.[104–108] We thereby selected citric acid as coating for the modification of the previous one-step fast microwave synthesis of ^{68}Ga core-doped IONPs previously developed in the group. Microwave-assisted synthesis together with the use of citric acid as a surfactant results in ^{68}Ga core-doped IONPs with extremely small cores that produce signal in T_1-weighted MRI and PET: ^{68}Ga-IONP. These citrate-coated ^{68}Ga-IONPs have been successfully used by our group for the *in vivo* detection and quantification of inflammation in mice using PET, using a peptide which is antagonist of formyl peptide receptor 1 (FPR-1) to direct nanoparticles to target site;[109] for the *in vivo* detection of thrombi in mice using bioorthogonal chemistry with a pretargeted approach with an antibody targeting activated platelets (CD41 antibody);[110] and as hybrid contrast agent for PET and *ex vivo* T_1 MRI for atherosclerosis detection in mice by pretargeted imaging with an antibody targeting oxidised phospholipids (E-06 antibody).[111]

Our citrate-coated ^{68}Ga-IONPs not only overcome limitations presented by other IONPs used as T_2 contrast agents for MRI, but also provide signal in a second imaging modality: PET. The use of microwave technology allows a rapid (ready-to-use NPs in 20 minutes, including purification step) and reproducible synthesis alongside the incorporation in a single synthetic step of the PET isotope in the NP core. This is especially significant when working with short half-lived radioisotopes as is the case of ^{68}Ga. The radiolabelling yield (92%) is also an outstanding advantage with respect to traditional radiolabelling approaches and triples the radiolabelling yield obtained by the pioneers of this NP radiolabelling method.[112] Core-doping offers a further advantage: reducing the potential transmetallation or radioisotope detachment *in vivo*, guaranteeing

signal observed in PET is provided by the radiolabelled IONPs. Furthermore, ^{68}Ga not incorporated in NP core during the synthesis is discarded during the gel filtration purification step, ensuring there is no free ^{68}Ga contributing to PET signal.

Suitable circulating times for imaging purposes are endorsed by their stability in physiological conditions, preventing aggregation and prompt elimination. The remarkable longitudinal relaxivity value (r_1) obtained in addition to the low r_2/r_1 ratio makes them an ideal contrast agent for T_1-MRI, that together with the high radiolabelling yield and specific activity, will enable the *in vivo* use of a ^{68}Ga-IONP reduced dose that will suit both PET and MR imaging.

^{68}Ga-IONPs are the perfect example of the potential synergy that nanotechnology and radiochemistry can offer. This new tool can be used *in vivo* for the multimodal detection, by a combination of anatomical and functional imaging techniques, of molecular and cellular processes in a non-invasive way.

Video Article

Synthesis of ^{68}Ga Core-doped Iron Oxide Nanoparticles for Dual Positron Emission Tomography /(T_1)Magnetic Resonance Imaging

Irene Fernández-Barahona[1], Jesús Ruiz-Cabello[2], Fernando Herranz[1], Juan Pellico[3]

[1]Nanobiotechnology, Molecular Imaging and Metabolomics Lab, Centro Nacional de Investigaciones Cardiovasculares Carlos III (CNIC)

[2]CIC biomaGUNE and CIBER de Enfermedades Respiratorias (CIBERES). Ikerbasque, Basque Foundation for Science, Universidad Complutense de Madrid (UCM)

[3]Advanced Imaging Unit, Centro Nacional de Investigaciones Cardiovasculares Carlos III (CNIC), CIBER de Enfermedades Respiratorias (CIBERES)

Correspondence to: Fernando Herranz at fherranz@iqm.csic.es, Juan Pellico at jpellico@cnic.es

URL: https://www.jove.com/video/58269
DOI: doi:10.3791/58269

Keywords: Biology, Issue 141, Iron oxide nanoparticles, ^{68}Ga, positron emission tomography, magnetic resonance imaging, microwave synthesis, citric acid

Date Published: 11/20/2018

Citation: Fernández-Barahona, I., Ruiz-Cabello, J., Herranz, F., Pellico, J. Synthesis of ^{68}Ga Core-doped Iron Oxide Nanoparticles for Dual Positron Emission Tomography /(T_1)Magnetic Resonance Imaging. *J. Vis. Exp.* (141), e58269, doi:10.3791/58269 (2018).

Abstract

Here, we describe a microwave synthesis to obtain iron oxide nanoparticles core-doped with ^{68}Ga. Microwave technology enables fast and reproducible synthetic procedures. In this case, starting from $FeCl_3$ and citrate trisodium salt, iron oxide nanoparticles coated with citric acid are obtained in 10 min in the microwave. These nanoparticles present a small core size of 4.2 ± 1.1 nm and a hydrodynamic size of 7.5 ± 2.1 nm. Moreover, they have a high longitudinal relaxivity (r_1) value of 11.9 $mM^{-1}{\cdot}s^{-1}$ and a modest transversal relaxivity value (r_2) of 22.9 $mM^{-1}{\cdot}s^{-1}$, which results in a low r_2/r_1 ratio of 1.9. These values enable positive contrast generation in magnetic resonance imaging (MRI) instead of negative contrast, commonly used with iron oxide nanoparticles. In addition, if a $^{68}GaCl_3$ elution from a $^{68}Ge/^{68}Ga$ generator is added to the starting materials, a nano-radiotracer doped with ^{68}Ga is obtained. The product is obtained with a high radiolabeling yield (> 90%), regardless of the initial activity used. Furthermore, a single purification step renders the nano-radiomaterial ready to be used *in vivo*.

Video Link

The video component of this article can be found at https://www.jove.com/video/58269/

Introduction

The combination of imaging techniques for medical purposes has triggered the quest for different methods to synthesize multimodal probes[1,2,3]. Due to the sensitivity of positron emission tomography (PET) scanners and the spatial resolution of MRI, PET/MRI combinations seem to be one of the most attractive possibilities, providing anatomical and functional information at the same time[4]. In MRI, T_2-weighted sequences can be used, darkening the tissues in which they accumulate. T_1-weighted sequences may also be used, producing the brightening of the specific accumulation location[5]. Among them, positive contrast is often the most adequate option, as negative contrast makes it much harder to differentiate signal from endogenous hypointense areas, including those often presented by organs such as the lungs[6]. Traditionally, Gd-based molecular probes have been employed to obtain positive contrast. However, Gd-based contrast agents present a major drawback, namely their toxicity, which is critical in patients with renal problems[7,8,9]. This has motivated research in the synthesis of biocompatible materials for their use as T_1 contrast agents. An interesting approach is the use of iron oxide nanoparticles (IONPs), with an extremely small core size, that provide positive contrast[10]. Due to this extremely small core (~2 nm), most of the Fe^{3+} ions are on the surface, with 5 unpaired electrons each. This increases longitudinal relaxation time (r_1) values and yields much lower transversal/longitudinal (r_2/r_1) ratios compared to traditional IONPs, producing the desired positive contrast[11].

To combine IONPs with a positron emitter for PET, there are two key issues to take into account: radioisotope election and nanoparticle radiolabeling. Regarding the first issue, ^{68}Ga is an alluring choice. It has a relatively short half-life (67.8 min). Its half-life is suitable for peptide labeling since it matches common peptide biodistribution times. Moreover, ^{68}Ga is produced in a generator, enabling the synthesis in bench modules and avoiding the need for a cyclotron nearby[12,13,14]. In order to radiolabel the nanoparticle, surface-labeling radioisotope incorporation is the prevalent strategy. This can be done using a ligand that chelates ^{68}Ga or taking advantage of the affinity of the radiometal toward the surface of the nanoparticle. Most examples in the literature concerning IONPs use a chelator. There are examples of the use of heterocyclic ligands such as 1,4,7,10-tetraazacyclododecane-1,4,7,10-tetraacetic acid (DOTA)[15], 1,4,7-triazacyclononane-1,4,7-triacetic acid (NOTA)[16,17], and 1,4,7-triazacyclononane,1-glutaric acid-4,7-acetic acid (NODAGA)[18], and the use of 2,3-dicarboxypropane-1,1-diphosphonic acid (DPD), a tetradentate ligand [19]. Madru *et al.*[20] developed a chelator-free strategy in 2014 to label IONPs using a chelator-free method used by another group posteriorly[21].

However, major drawbacks of this approach include a high risk of *in vivo* transmetalation, low radiolabeling yields, and lengthy protocols unsuitable for short-lived isotopes[22,23,24]. For this reason, Wong *et al.*[25] developed the first example of core-doped nanoparticles, managing to incorporate ^{64}Cu in the core of the IONPs in a 5-min synthesis using microwave technology.

Here, we describe a rapid and efficient procedure to incorporate the radionuclide into the core of the nanoparticle, eluding many of the drawbacks presented by traditional methods. For this purpose, we propose the use of a microwave-driven synthesis (MWS), which reduces reaction times considerably, increases yields, and enhances reproducibility, critically important parameters in IONP synthesis. The refined performance of MWS is due to dielectric heating: rapid sample heating as molecular dipoles try to align with the alternating electric field, being polar solvents and reagents more efficient for this type of synthesis. In addition, the use of citric acid as a surfactant, together with microwave technology, results in extremely small nanoparticles, producing a dual T_1-weighted MRI/PET[26] signal, herein denoted as ^{68}Ga Core-doped iron oxide nanoparticles (^{68}Ga-C-IONP).

The protocol combines the use of microwave technology, $^{68}GaCl_3$ as positron emitter, iron chloride, sodium citrate, and hydrazine hydrate, resulting in dual T_1-weighted MRI/PET nanoparticulate material in hardly 20 min. Moreover, it yields consistent results over a range of ^{68}Ga activities (37 MBq, 111 MBq, 370 MBq, and 1110 MBq) with no significant effects on the main physicochemical properties of the nanoparticles. The reproducibility of the method using high ^{68}Ga activities extends the field of possible applications, including large animal models or human studies. In addition, there is a single purification step included in the method. In the process, any excess of free gallium, iron chloride, sodium citrate, and hydrazine hydrate are removed by gel filtration. Total free isotope elimination and the purity of the sample ensure no toxicity and enhance imaging resolution. In the past, we have already demonstrated the usefulness of this approach in targeted molecular imaging[27,28].

Protocol

1. Reagent Preparation

1. **0.05 M HCl**
   1. Prepare 0.05 M HCl by adding 208 µL of 37% HCl to 50 mL of distilled water.

2. **High-performance liquid chromatography eluent**
   1. Prepare high-performance liquid chromatography (HPLC) eluent by dissolving 6.9 g of sodium dihydrogen phosphate monohydrate, 7.1 g of disodium hydrogen phosphate, 8.7 g of sodium chloride, and 0.7 g of sodium azide in 1 L of water. Mix well and check the pH. Pass the eluent through a 0.1-µm cutoff sterile filter and degas before use. Acceptance range: pH 6.2 - 7.0 (if not, adjust with NaOH [1 M] or HCl [5 M]).

2. Synthesis of Citrate-coated Iron Oxide Nanoparticles

1. Dissolve 75 mg of $FeCl_3 \cdot 6H_2O$ and 80 mg of citric acid trisodium salt dihydrate in 9 mL of water.
   NOTE: These quantities provide 12 mL of final purified nanoparticles ([Fe] ~1.4 $mg \cdot mL^{-1}$). Quantities can be scaled down to obtain a final volume of 2.5 mL.
2. Put the mixture in the microwave-adapted flask.
3. Load a dynamic protocol in the microwave. Set the temperature to 120 °C, the time to 10 min, the pressure to 250 psi, and the power to 240 W.
4. Add 1 mL of hydrazine hydrate to the reaction.
   NOTE: Hydrazine hydrate starts iron reduction. Therefore, a change in the appearance of the solution, from light yellow to brown, is observed.
5. Start the microwave protocol.
6. Meanwhile, rinse a gel filtration desalting column with 20 mL of distilled water.
7. Once the protocol has finished, allow the flask to cool at room temperature.
8. Pipette 2.5 mL of the final mixture onto the column and discard the flow-through.
   NOTE: The microwave stops the protocol at 60 °C; the nanoparticles can be added directly to the gel filtration column at 60 °C.
9. Add 3 mL of distilled water to the column and collect the nanoparticles in a glass vial.
   NOTE: Nanoparticles can be stored at room temperature for 1 week. After this time, nanoparticle aggregation appears, increasing their hydrodynamic size.

3. Synthesis of ^{68}Ga Core-doped Iron Oxide Nanoparticles (^{68}Ga-C-IONP)

1. Put 75 mg of $FeCl_3 \cdot 6H_2O$ and 80 mg of citric acid trisodium salt dihydrate into the microwave-adapted flask.
2. Elute the $^{68}Ge/^{68}Ga$ generator using the recommended volume and concentration of HCl, according to the vendor (in our case, 4 mL of 0.05 M HCl). After the injection of that volume in the self-shielded generator, (4 mL of) $^{68}GaCl_3$ is obtained, ready to use without further processing.
   NOTE: Follow the corresponding radioactivity safety measures for steps 3.2 - 3.12. ^{68}Ga is a positron and gamma emitter isotope. The use of the appropriate safety measures to avoid exposure to radiation by the operator is crucial. Researchers must follow an ALARA (as low as reasonably achievable) protocol using typical shielding and radionuclide-handling procedures. Moreover, the use of a ring, body badges, and a contamination detector is mandatory.
3. Add 4 mL of $^{68}GaCl_3$ to the microwave-adapted flask. This volume can be smaller, depending on the generator activity and desired activity of final nanoparticles.
4. Pipette 5 mL of distilled water into the flask and mix well.
5. Load a dynamic protocol in the microwave. Set the temperature to 120 °C, the time to 10 min, the pressure to 250 psi, and the power to 240 W.

6. Add 1 mL of hydrazine hydrate to the reaction.
   NOTE: Hydrazine hydrate starts iron reduction. Therefore, a change in the appearance of the solution, from light yellow to brown, is observed.
7. Start the microwave protocol.
8. Meanwhile, rinse a gel filtration desalting column with 20 mL of distilled water.
9. Once the protocol has finished, allow the flask to cool at room temperature.
10. Pipette 2.5 mL of the final mixture onto the column and discard the flow-through.
    NOTE: The microwave stops the protocol at 60 °C; the nanoparticles can be directly added to the gel filtration column at 60 °C.
11. Add 3 mL of distilled water to the column and collect the nanoparticles in a glass vial.
12. Calculate radiolabeling efficiency using a NaI well-type detector. This parameter typically measures the activity of the ^{68}Ga incorporated in the reaction. After synthetic and purification processes, the activity of the purified sample is measured. Because of the short half-life of ^{68}Ga, the initial activity has to be corrected at time (t). Normalization with time follows the standard equation:
    $N_T = N_0 \cdot e^{-\lambda t}$
    Here,
    N_T: Counts at time (t)
    N_0: Counts at time (t) = 0
    λ: Decay constant
    t: Elapsed time

$$\text{Radiolabeling efficiency} = \frac{\text{MBq purified product (at time = t)}}{\text{MBq initial radioactivity (corrected at time = t)}} \text{ x } 100$$

    NOTE: Radiolabeling efficiency should be between 90% - 95%.

4. Analysis of ^{68}Ga Core-doped Iron Oxide Nanoparticles (^{68}Ga-C-IONP)

1. **Dynamic light scattering**
   1. Use dynamic light scattering (DLS) to measure the hydrodynamic size of ^{68}Ga-C-IONP. Pipette 60 µL of the sample into a cuvette and perform three size measurements per sample. To ensure reproducibility, this should be repeated with several nanoparticle batches.

2. **Colloidal stability**
   1. Assess the colloidal stability of ^{68}Ga-C-IONP by measuring the hydrodynamic size of the sample after incubation in different buffers (PBS, saline, and mouse serum) for different times, ranging from 0 to 24 h. Incubate 500 µL of the sample in each buffer at 37 °C. At the selected times, take 60-µL aliquots and pipette them into DLS cuvettes to measure their hydrodynamic size.

3. **Electron microscopy**
   1. Analyze the core size of ^{68}Ga-C-IONP using transmission electron microscopy (TEM) and annular dark-field imaging (STEM-HAADF) (ref TEM protocol: NIST - NCL Joint Assay Protocol, PCC-X, Measuring the Size of Nanoparticles Using Transmission Electron Microscopy).

4. **Gel filtration radio-chromatogram**
   1. Fractionate the elution into 500-µL aliquots during the gel-filtration purification step and measure the radioactivity present in each one using an activimeter; thus, rendering a gel-filtration chromatogram.

5. **Radiochemical stability of ^{68}Ga-C-IONP**
   1. Incubate ^{68}Ga-C-IONP in mouse serum for 30 min at 37 °C (repeated 3x). After that time, purify the nanoparticles by ultrafiltration and measure the radioactivity present in the nanoparticles and filtrate. No activity should be detected in the different filtrates.

6. **Relaxometry**
   1. Measure longitudinal (T_1) and transverse (T_2) relaxation times in a relaxometer at 1.5 T and 37 °C. Four different concentrations of ^{68}Ga-C-IONP (2 mM, 1 mM, 0.5 mM, and 0.25 mM) should be measured. Plot relaxation rates (r_1=1/T_1, r_2=1/T_2) against iron concentration. The slope of the curve obtained renders r_1 and r_2 values.

7. **MR and PET phantom images**
   1. Acquire *in situ* MR (T_1-weighted sequence) and PET phantom images for a series of dilutions of ^{68}Ga-C-IONP (0 mM, 1 mM, 6.5 mM, and 9.0 mM) to observe the increasing signal in correlation with the PET activity and MRI.

Representative Results

^{68}Ga-C-IONP were synthesized by combining $FeCl_3$, $^{68}GaCl_3$, citric acid, water, and hydrazine hydrate. This mixture was introduced into the microwave for 10 min at 120 °C and 240 W under controlled pressure. Once the sample had cooled down to room temperature, the nanoparticles were purified by gel filtration to eliminate unreacted species ($FeCl_3$, citrate, hydrazine hydrate) and free ^{68}Ga (**Figure 1**).

The hydrodynamic size of ^{68}Ga-C-IONP was measured using dynamic light scattering (DLS). This revealed a narrow size distribution (PDI 0.2) and mean hydrodynamic size of 7.9 nm. Measurements of five different syntheses proved method reproducibility (**Figure 2a**). The zeta potential of several ^{68}Ga-C-IONP syntheses was measured to analyze nanoparticle surface charge; the mean value obtained was -36.5 mV. ^{68}Ga-C-IONP was incubated in different media at 37 °C during different times to ensure nanoparticle stability in biological solutions. The hydrodynamic size was measured at different times, revealing ^{68}Ga-C-IONP hydrodynamic size suffers no significant changes, meaning the sample is stable in different buffers and serums (**Figure 2b**). Because of the fast heating achieved using microwave technology, nanoparticles present ultra-small core sizes of about 4 nm. Electron microscopy images revealed homogeneous core sizes and the absence of aggregation (**Figure 2c**). A gel filtration chromatogram of ^{68}Ga-C-IONP shows a main radioactivity peak corresponding to the nanoparticles, followed by a reduced peak that corresponds to free ^{68}Ga (**Figure 2d**). The radiolabeling yield calculated after sample purification was 92%. This excellent radiolabeling yield was translated into a specific activity relative to an iron amount of 7.1 GBq/mmol Fe. The potential of ^{68}Ga-C-IONP as a contrast agent for MRI was checked by measuring longitudinal (r_1) and transversal (r_2) relaxation times. These were measured for five different ^{68}Ga-C-IONP syntheses at 37 °C and 1.5 T. An excellent mean r_1 value of 11.9 $mM^{-1}{\cdot}s^{-1}$ and a modest r_2 value of 22.9 $mM^{-1}{\cdot}s^{-1}$ were obtained, yielding an average r_2/r_1 ratio of 1.9, meaning ^{68}Ga-C-IONP is ideal for T_1-weighted MRI (**Figure 2e**). To confirm this hypothesis, the capability of ^{68}Ga-C-IONP to produce T_1 contrast in an MRI and PET signal was checked with the acquisition of PET and MR phantom images at different ^{68}Ga-C-IONP concentrations. As the iron concentration increases, so does the positive contrast in MR phantom. An increasing iron concentration implies an increasing ^{68}Ga concentration as well; hence, the PET signal is increasingly intense (**Figure 2f**).

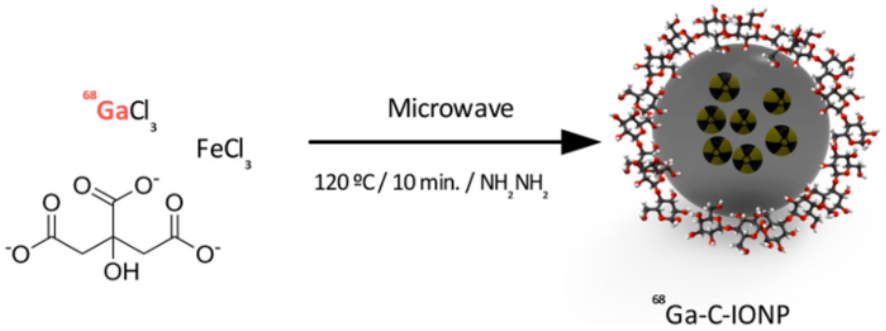

Figure 1: Synthetic steps followed in the protocol. Precursors are added in a microwave flask and introduced into the microwave upon hydrazine hydrate addition at 120 °C for 10 minutes, after which nanoparticles are obtained. Please click here to view a larger version of this figure.

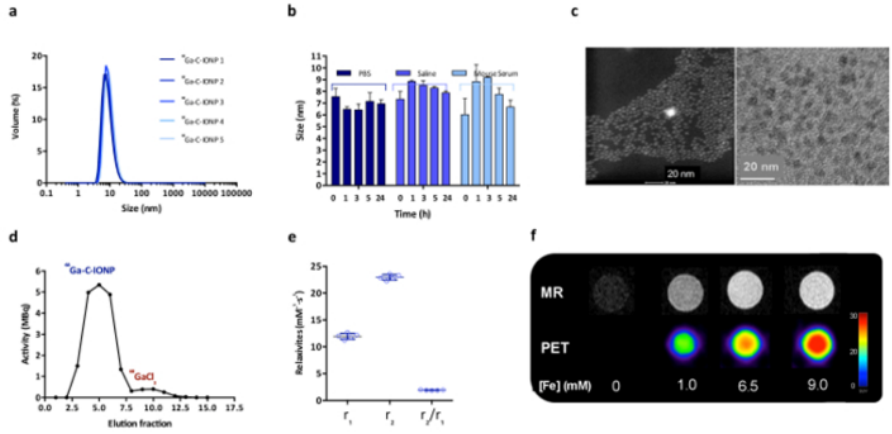

Hydrodynamic Size	Core Size	Zeta Potential	r_1	r_2	r_2/r_1	Radiolabeling Yield	Specific Activity
7.9 nm	4.2 nm	-36.5 mV	11.9 $mM^{-1}{\cdot}s^{-1}$	22.9 $mM^{-1}{\cdot}s^{-1}$	1.9	92%	7.1 GBq/mmol Fe

Figure 2: ^{68}Ga-C-IONP characterization. (**a**) This panel shows the hydrodynamic size distribution (volume weighted) of five different syntheses of ^{68}Ga-C-IONP. (**b**) This panel shows the hydrodynamic size (maximum peak in volume, mean ± SD) of ^{68}Ga-C-IONP in PBS, saline, and mouse serum (from t = 0 h to t = 24 h). (**c**) These are STEM-HAADF (left) and TEM (right) images of ^{68}Ga-C-IONP. The scale bars are 20 nm. (**d**) This panel shows a gel filtration radio-chromatogram. (**e**) This panel shows the longitudinal (r_1) and transversal (r_2) relaxivity values, and the r_2/r_1 ratio for five ^{68}Ga-C-IONP syntheses (mean ± SD). (**f**) These are MR and PET phantom images of different ^{68}Ga-C-IONP concentrations. (**g**) This is a table summarizing the main ^{68}Ga-C-IONP characteristics. Please click here to view a larger version of this figure.

Discussion

Iron oxide nanoparticles are a well-established contrast agent for T_2-weighted MRI. However, due to the drawbacks of this type of contrast for the diagnosis of certain pathologies, T_1-weighted or bright contrast is many times preferred. The nanoparticles presented here not only overcome these limitations by offering positive contrast in MRI but also offer a signal in a functional imaging technique, such as PET, *via* ^{68}Ga incorporation in their core. Microwave technology enhances this reproducible nanoparticle synthesis, considerably reducing the reaction time to a total of approximately 20 minutes (including a purification step). It also allows radioisotope incorporation at once in the core of the nanoparticle; suppressing an extra step required in a surface-labeling approach that would markedly extend the reaction time. This is a major advantage, especially when working with short half-live isotopes as ^{68}Ga ($t_{1/2}$ = 68.8 min). Moreover, the radiolabeling yield obtained (92%) is almost threefold the one obtained by the pioneering study using this nanoparticle-radiolabeling approach (Wong *et al.*[25]). This also represents a considerable improvement with respect to previous approaches, as in less than 20 minutes intrinsically radiolabeled nanoparticles with an excellent radiolabeling yield can be obtained; thus, eliminating *in vivo* radioisotope detachment or transmetalation risk and ensuring that the PET signal obtained comes from the nano-radiotracer and not from free ^{68}Ga. This will ease their potential use as contrast agents.

As ^{68}Ga-C-IONP are stable in different media at physiological temperature, no aggregation *in vivo* will take place; therefore presenting long blood circulating times. The gel filtration purification step eliminates the free ^{68}Ga fraction that has not been incorporated into nanoparticle cores, ensuring the PET signal is entirely provided by the ^{68}Ga-C-IONP. The outstanding r_1 value, together with the low r_2/r_1 ratio, the high radiolabeling yield, and specific activity, will allow the ^{68}Ga-C-IONP dose that is required to obtain an appropriate signal in PET and contrast in MRI to be diminished.

The nano-radiotracer presented here demonstrates that the combination of nanotechnology and radiochemistry can render a new tool that can be used for the *in vivo* detection of biological processes or diverse pathologies by means of PET and T_1-weighted MRI. It has already been used successfully in the detection by PET and MRI of angiogenesis in a murine model using RGD peptide as targeting moiety[27]. ^{68}Ga-C-IONP has also been employed, combined with a formyl peptide receptor 1 (FPR-1) antagonist, to target neutrophils in the detection of lung inflammation by PET in a non-invasive manner[28].

Disclosures

The authors have nothing to disclose.

Acknowledgements

This study was supported by a grant from the Spanish Ministry for Economy and Competitiveness (MEyC) (grant number: SAF2016-79593-P) and from the Carlos III Health Research Institute (grant number: DTS16/00059). The CNIC is supported by the Ministerio de Ciencia, Innovación y Universidades) and the Pro CNIC Foundation and is a Severo Ochoa Centre of Excellence (MEIC award SEV-2015-0505).

References

1. Jennings, L. E., Long, N. J. 'Two is better than one'--probes for dual-modality molecular imaging. *Chemical Communications.* (Cambridge, UK). (24), 3511-3524 (2009).
2. Lee, S., Chen, X. Dual-modality probes for *in vivo* molecular imaging. *Molecular Imaging.* **8** (2), 87-100 (2009).
3. Louie, A. Multimodality Imaging Probes: Design and Challenges. *Chemical Reviews.* **110** (5), 3146-3195 (2010).
4. Judenhofer, M. S. *et al.* Simultaneous PET-MRI: a new approach for functional and morphological imaging. *Nature Medicine.* **14** (4), 459-465 (2008).
5. Burtea, C., Laurent, S., Vander Elst, L., Muller, R. N. Contrast agents: magnetic resonance. *Handbook of Experimental Pharmacology.* (185 Pt 1), 135-165 (2008).
6. Zhao, X., Zhao, H., Chen, Z., Lan, M. Ultrasmall superparamagnetic iron oxide nanoparticles for magnetic resonance imaging contrast agent. *Journal of Nanoscience and Nanotechnology.* **14** (1), 210-220 (2014).
7. Cheng, W. *et al.* Complementary Strategies for Developing Gd-Free High-Field T 1 MRI Contrast Agents Based on Mn III Porphyrins. *Journal of Medicinal Chemistry.* **57** (2), 516-520 (2014).
8. Kim, H.-K. *et al.* Gd-complexes of macrocyclic DTPA conjugates of 1,1′-bis(amino)ferrocenes as high relaxivity MRI blood-pool contrast agents (BPCAs). *Chemical Communications.* **46** (44), 8442 (2010).
9. Sanyal, S., Marckmann, P., Scherer, S., Abraham, J. L. Multiorgan gadolinium (Gd) deposition and fibrosis in a patient with nephrogenic systemic fibrosis--an autopsy-based review. *Nephrology, Dialysis, Transplantation: Official Publication of the European Dialysis and Transplant Association - European Renal Association.* **26** (11), 3616-3626 (2011).
10. Hu, F., Jia, Q., Li, Y., Gao, M. Facile synthesis of ultrasmall PEGylated iron oxide nanoparticles for dual-contrast T1- and T2-weighted magnetic resonance imaging. *Nanotechnology.* **22**, 245604 (2011).
11. Kim, B. H. *et al.* Large-Scale Synthesis of Uniform and Extremely Small-Sized Iron Oxide Nanoparticles for High-Resolution T 1 Magnetic Resonance Imaging Contrast Agents. *Journal of the American Chemical Society.* **133** (32), 12624-12631 (2011).
12. Banerjee, S. R., Pomper, M. G. Clinical applications of Gallium-68. *Applied Radiation and Isotopes.* **76**, 2-13 (2013).
13. Breeman, W. A. P. *et al.* 68Ga-labeled DOTA-Peptides and 68Ga-labeled Radiopharmaceuticals for Positron Emission Tomography: Current Status of Research, Clinical Applications, and Future Perspectives. *Seminars in Nuclear Medicine.* **41** (4), 314-321 (2011).
14. Morgat, C., Hindié, E., Mishra, A. K., Allard, M., Fernandez, P. Gallium-68: chemistry and radiolabeled peptides exploring different oncogenic pathways. *Cancer Biotherapy & Radiopharmaceuticals.* **28** (2), 85-97 (2013).

15. Moon, S.-H. *et al.* Development of a complementary PET/MR dual-modal imaging probe for targeting prostate-specific membrane antigen (PSMA). *Nanomedicine: Nanotechnology, Biology and Medicine.* **12** (4), 871-879 (2016).
16. Kim, S. M. *et al.* Hybrid PET/MR imaging of tumors using an oleanolic acid-conjugated nanoparticle. *Biomaterials.* **34** (33), 8114-8121 (2013).
17. Yang, B. Y. *et al.* Development of a multimodal imaging probe by encapsulating iron oxide nanoparticles with functionalized amphiphiles for lymph node imaging. *Nanomedicine.* **10** (12), 1899-1910 (2015).
18. Comes Franchini, M. *et al.* Biocompatible nanocomposite for PET/MRI hybrid imaging. *International Journal of Nanomedicine.* **7**, 6021 (2012).
19. Karageorgou, M. *et al.* Gallium-68 Labeled Iron Oxide Nanoparticles Coated with 2,3-Dicarboxypropane-1,1-diphosphonic Acid as a Potential PET/MR Imaging Agent: A Proof-of-Concept Study. *Contrast Media & Molecular Imaging.* **2017**, 1-13 (2017).
20. Madru, R. *et al.* (68)Ga-labeled superparamagnetic iron oxide nanoparticles (SPIONs) for multi-modality PET/MR/Cherenkov luminescence imaging of sentinel lymph nodes. *American Journal of Nuclear Medicine and Molecular Imaging.* **4** (1), 60-69 (2013).
21. Lahooti, A. *et al.* PEGylated superparamagnetic iron oxide nanoparticles labeled with 68Ga as a PET/MRI contrast agent: a biodistribution study. *Journal of Radioanalytical and Nuclear Chemistry.* **311** (1), 769-774 (2017).
22. Lee, H.-Y. *et al.* PET/MRI dual-modality tumor imaging using arginine-glycine-aspartic (RGD)-conjugated radiolabeled iron oxide nanoparticles. *Journal of Nuclear Medicine.* **49** (8), 1371-1379 (2008).
23. Patel, D. *et al.* The cell labeling efficacy, cytotoxicity and relaxivity of copper-activated MRI/PET imaging contrast agents. *Biomaterials.* **32** (4), 1167-1176 (2011).
24. Choi, J. *et al.* A Hybrid Nanoparticle Probe for Dual-Modality Positron Emission Tomography and Magnetic Resonance Imaging. *Angewandte Chemie International Edition.* **47** (33), 6259-6262 (2008).
25. Wong, R. M. *et al.* Rapid size-controlled synthesis of dextran-coated, 64Cu-doped iron oxide nanoparticles. *ACS Nano.* **6** (4), 3461-3467 (2012).
26. Osborne, E. A. *et al.* Rapid microwave-assisted synthesis of dextran-coated iron oxide nanoparticles for magnetic resonance imaging. *Nanotechnology.* **23** (21), 215602 (2012).
27. Pellico, J. *et al.* Fast synthesis and bioconjugation of 68 Ga core-doped extremely small iron oxide nanoparticles for PET/MR imaging. *Contrast Media & Molecular Imaging.* **11** (3), 203-210 (2016).
28. Pellico, J. *et al.* In vivo imaging of lung inflammation with neutrophil-specific 68Ga nano-radiotracer. *Scientific Reports.* **7** (1), 13242 (2017).

3.2 Copper-doped extremely small iron oxide nanoparticles with large longitudinal relaxivity: applications in MRA and targeted T_1-MRI (Article 2)

As previously mentioned, the development of iron oxide nanoparticles for T_1 MRI aims to combine the large longitudinal relaxivities of Gd-based contrast agents with the appealing properties that nanoparticles present: tailorable properties and hence pharmacokinetics, reduced toxicity and the possibility of multifunctionalisation with a wide variety of moieties for further imaging modalities, therapy, etc.

A good T_1 contrast agent must fulfill two key conditions: a large r_1 value and a low r_2/r_1 ratio. In order to achieve this, the typical approach is to reduce the IONP core size, so they behave as a paramagnetic material rather than as a superparamagnetic one. In a study carried out by our group, we demonstrated it is possible to tune the relaxometric properties of IONPs by modifying the surface chemistry of the nanoparticles, switching from T_1 to T_2 contrast.[6] A further alternative, explored here, is to dope the IONP cores with different metals. There are examples of metal core doping using copper, nickel, zinc and different combinations of them that increase the r_2 values and other examples with Gd or Mn as the dopant metal which increase the r_1 value.[113–119] The examples in the literature of copper doping yield nanomaterials suitable for use as T_2 contrast agents.[112,120] To our knowledge, there are no examples of copper doping of nanoparticles for T_1-weighted MRI. In this work, we studied how the doping of IONP cores with different amounts of copper affects their relaxometric properties and contrast capabilities for a substantial improvement of their performance in T_1-weighted MRI .

We synthesised three samples with different and increasing initial amounts of copper salt in the synthesis precursors. This yielded nanoparticles with 1.7 mol%, 4 mol % and 28 mol% copper, indicating our microwave-assisted synthesis is a suitable approach for IONP core doping with copper. Their physicochemical properties indicate they are suitable for *in vivo* use, as they are stable and have a non-toxic composition.

The study of the relaxometric properties of the sample reveals all samples are suitable for T_1-weighted MRI having high r_1 values and low r_2/r_1 ratios. However, Although the 2 samples with the lowest amount have an improved r_1 value with respect to non-doped IONPs, it is not so for the sample with the highest copper doping amount. The magnetic measurements of this sample suggest a core-shell structure, having the major part of the copper atoms in the surface of the NP core. This conformation reduces the inner sphere relaxation mechanism, as a small amount of iron atoms are in contact with the surrounding water protons, explaining the lower r_1 value this sample presents with respect to the other two copper doped samples. Both Cu1.7NP and Cu4NP have outstanding r_1 values, in the case of Cu4NP, even similar to gadolinium- or manganese-based nanoparticles. Furthermore, low amount of copper doping induces a reduction in magnetisation but samples still have enough iron atoms on the surface for the inner relaxation mechanism to be dominant. As copper doping in the Cu1-7NP sample is minimal, this phenomenon is visible to a greater extent in the Cu4NP sample which presents the highest r_1 value.

In vivo experiments in magnetic resonance angiography with the three copper doped samples revealed positive contrast with Cu4NP and Cu1.7NP, as expected form the relaxometric values. Signal is clearer for Cu4NP, attributable to the higher r_1 value of this sample and it lower r_2/r_1 ratio. Cu4NP provides remarkable images with detailed vasculature visible up to 30 minutes post injection. As predicted from the relaxometric values obtained, Cu28NP shows poor contrast capability, as it presents the lowest r_1 value and a shorter circulation time than the other two samples, as this sample presents lower *in vivo* stability than the two samples doped with smaller copper amounts.

With the purpose of verifying the use of Cu4NP as a contrast agent, targeted MRI was carried out comparing both undoped IONPs with Cu4NP. Angiogenesis targeting in tumours using RGD as a directing vector shows specific NP accumulation in the tumour denoted by the increase in the signal, which is clearly higher for Cu4NP, by virtue of its larger r_1 value and lower r_2 than undoped IONPs.

ACS OMEGA

Article

Cite This: ACS Omega 2019, 4, 2719−2727

http://pubs.acs.org/journal/acsodf

Cu-Doped Extremely Small Iron Oxide Nanoparticles with Large Longitudinal Relaxivity: One-Pot Synthesis and in Vivo Targeted Molecular Imaging

Irene Fernández-Barahona,[†,○] Lucía Gutiérrez,[§] Sabino Veintemillas-Verdaguer,[∥] Juan Pellico,[†,‡] María del Puerto Morales,[∥] Mauro Catala,[⊥] Miguel A. del Pozo,[⊥] Jesús Ruiz-Cabello,[#,∇,○] and Fernando Herranz*[,†,‡]

[†]Instituto de Química Médica, CSIC, Juan de la Cierva 3, 28006 Madrid, Spain

[‡]Centro Nacional de Investigaciones Cardiovasculares Carlos III (CNIC) and CIBERES, 28029 Madrid, Spain

[§]Departamento de Química Analítica, Instituto de Nanociencia de Aragón, Universidad de Zaragoza, Instituto de Ciencia de Materiales de Aragón (ICMA/CSIC) y CIBER-BBN, 50018 Zaragoza, Spain

[∥]Instituto de Ciencia de Materiales de Madrid, CSIC, Sor Juana Inés de la Cruz 3, Cantoblanco, 28049 Madrid, Spain

[⊥]Centro Nacional de Investigaciones Cardiovasculares Carlos III (CNIC), 28029 Madrid, Spain

[#]CIC biomaGUNE, Paseo de Miramón 182, 20014 Donostia/San Sebastián, Spain

[∇]Ikerbasque, Basque Foundation for Science, 48013 Bilbao, Spain

[○]Universidad Complutense de Madrid and Centro de Investigación Biomédica en Red de Enfermedades Respiratorias (CIBERES), 28029 Madrid, Spain

Supporting Information

ABSTRACT: Synthesizing iron oxide nanoparticles for positive contrast in magnetic resonance imaging is the most promising approach to bring this nanomaterial back to the clinical field. The success of this approach depends on several aspects: the longitudinal relaxivity values, the complexity of the synthetic protocol, and the reproducibility of the synthesis. Here, we show our latest results on this goal. We have studied the effect of Cu doping on the physicochemical, magnetic, and relaxometric properties of iron oxide nanoparticles designed to provide positive contrast in magnetic resonance imaging. We have used a one-step, 10 min synthesis to produce nanoparticles with excellent colloidal stability. We have synthesized three different Cu-doped iron oxide nanoparticles showing modest to very large longitudinal relaxivity values. Finally, we have demonstrated the in vivo use of these kinds of nanoparticles both in angiography and targeted molecular imaging.

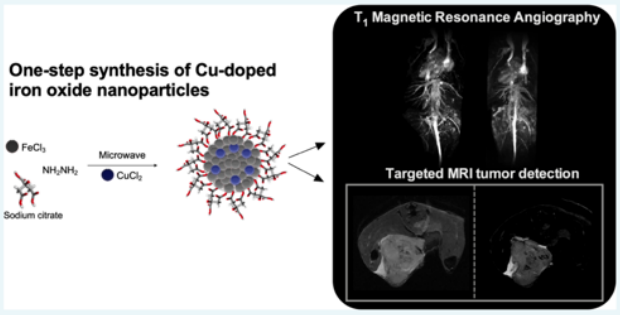

1. INTRODUCTION

The reduction of transverse relaxation time (T_2) and the longitudinal relaxation time (T_1) of water protons are the two main types of contrasts generated in magnetic resonance imaging (MRI). The first approach produces a darkening of the areas in the image where the probe has accumulated, whereas the second renders a brightening of the image. For technical and physiological reasons, a T_1-based contrast is preferred by radiologists and physicians for diagnostic purposes. From the imaging point of view, this is a key aspect, being one of the main reasons why "traditional" iron oxide nanoparticles (IONPs), for T_2-weighted imaging, have not been established as an alternative in the clinical practice. The quest for new iron oxide nanoparticle-based probes for magnetic resonance imaging (MRI) has traditionally focused on the obtainment of transverse relaxivity values (r_2) as large as possible.[1] Over the last years, the attention has moved to the development of IONPs as "positive" contrast agents, showing large longitudinal relaxivity values (r_1). The rationale behind this approach is trying to get the best of both worlds: commonly used contrast agents in MRI, Gd chelates, and nanoparticles. In other words, to have a good, easy to spot, signal in MRI without a noticeable toxicity, multifunctionalization, and the possibility of easily tuning the pharmacokinetics of the probe. Two aspects are crucial for a good T_1-based contrast agent: a large r_1 value and a small r_2/r_1 ratio. The most

Received: October 30, 2018
Accepted: January 22, 2019
Published: February 6, 2019

DOI: 10.1021/acsomega.8b03004
ACS Omega 2019, 4, 2719−2727

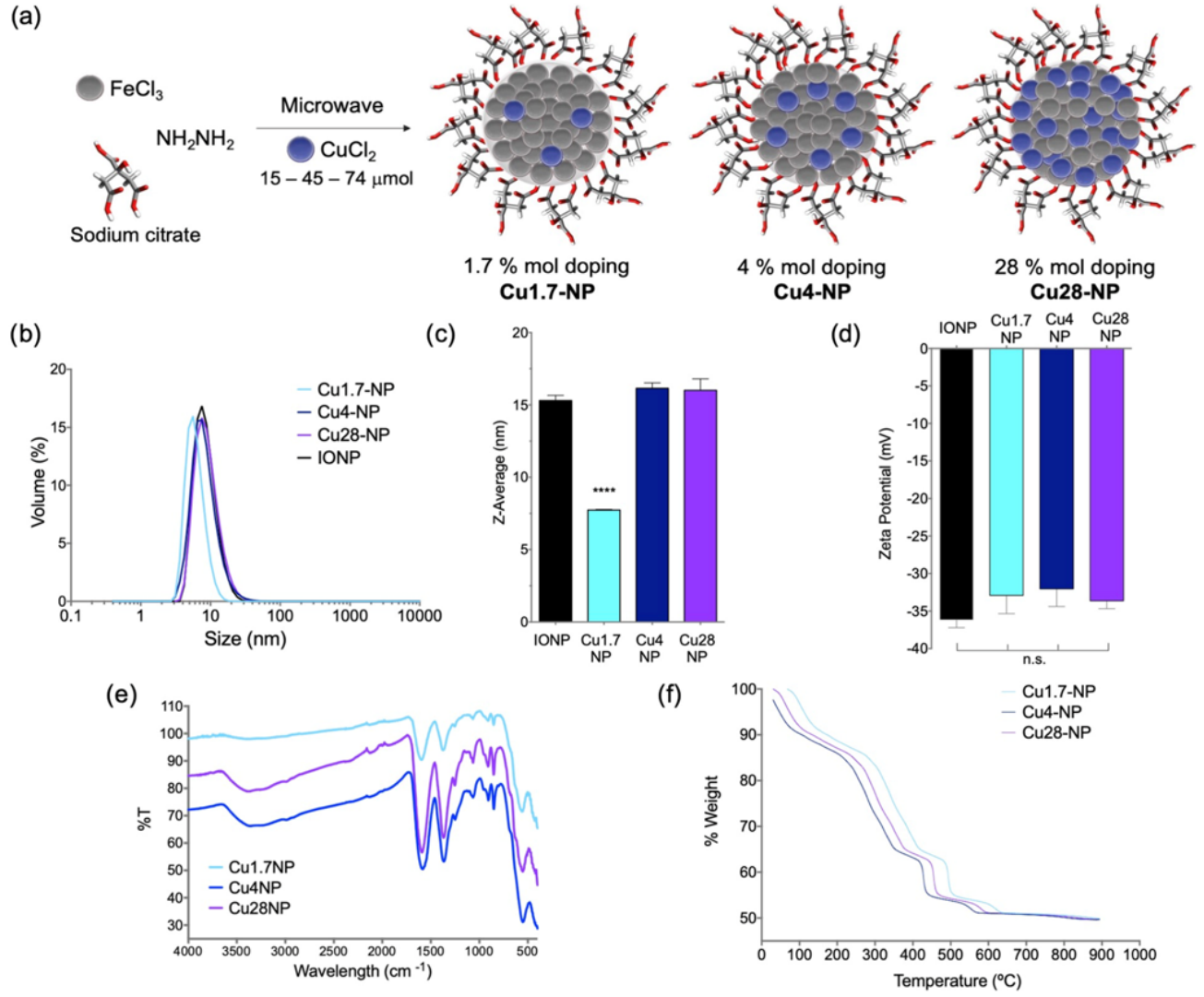

Figure 1. (a) Synthetic scheme for Cu1.7-NP, Cu4-NP, and Cu28-NP; (b) hydrodynamic size distribution, measured by dynamic light scattering (DLS); (c) *Z*-average size (mean with standard deviation, $N = 5$, $P = 0.0001$) and (d) ζ-potential for iron oxide nanoparticles (IONPs), Cu1.7-NP, Cu4-NP, and Cu28-NP; and (e) Fourier transform infrared (FTIR) spectra and (f) thermogravimetric curves for Cu1.7-NP, Cu4-NP, and Cu28-NP.

common approach to obtain IONPs as T_1 contrast agents is by reducing the core size. Due to the large surface effects, IONPs become more paramagnetic than superparamagnetic and the inner-sphere relaxation mechanism of water protons dominates.[2] Alternatively, it is possible to modify the chemistry of the coating molecules on the nanoparticles to obtain T_1-weighted contrast out of IONPs in vivo.[3] A third option is the core doping of the IONPs with different metals: a few examples describe an increase of the r_2 values (using Co, Ni, Zn, or combinations of them)[4−7] and fewer for positive contrast (mainly with Mn or Gd as the doping metal).[8−10] The use of Cu as a dopant, alone or in combination with other metals, in iron oxide nanoparticles, is limited, compared, for example, to its use as a dopant in ZnO nanoparticles. Cu doping effect has been studied in catalysis,[11] sensor performance,[12,13] and in the magnetic properties of the nanomaterial.[14−16] The use of Cu as a dopant for molecular imaging is limited, with one example, in combination with Co, using nanorods for MRI[17] and one example where the ^{64}Cu radioisotope is used for positron emission tomography.[18] Interestingly, in both cases, the relaxometric properties of the nanomaterials make them suitable exclusively for T_2-weighted MRI (dark contrast). Furthermore, there are no studies on the use of Cu doping as a way to obtain nanoparticles for positive contrast MRI.

The use of microwave-driven synthesis (MWS) for the production of nanomaterials is a versatile and highly reproducible approach. We have demonstrated how this methodology can produce, in extremely short times, homogeneous nanoparticles with excellent properties for molecular imaging.[3,19] However, in the production of nanoparticles for T_1-weighted MRI, the use of MWS is far from common. Most of the syntheses used for the production of T_1 nanoparticles are characterized by time-consuming protocols,[8−10,20,21] multistep approaches,[9,10,22−26] or the use of organic solvents.[22−26]

Here, we have studied the effect of Cu doping of iron oxide nanoparticles on their relaxometric properties. In a 10 min,

DOI: 10.1021/acsomega.8b03004
ACS Omega 2019, 4, 2719−2727

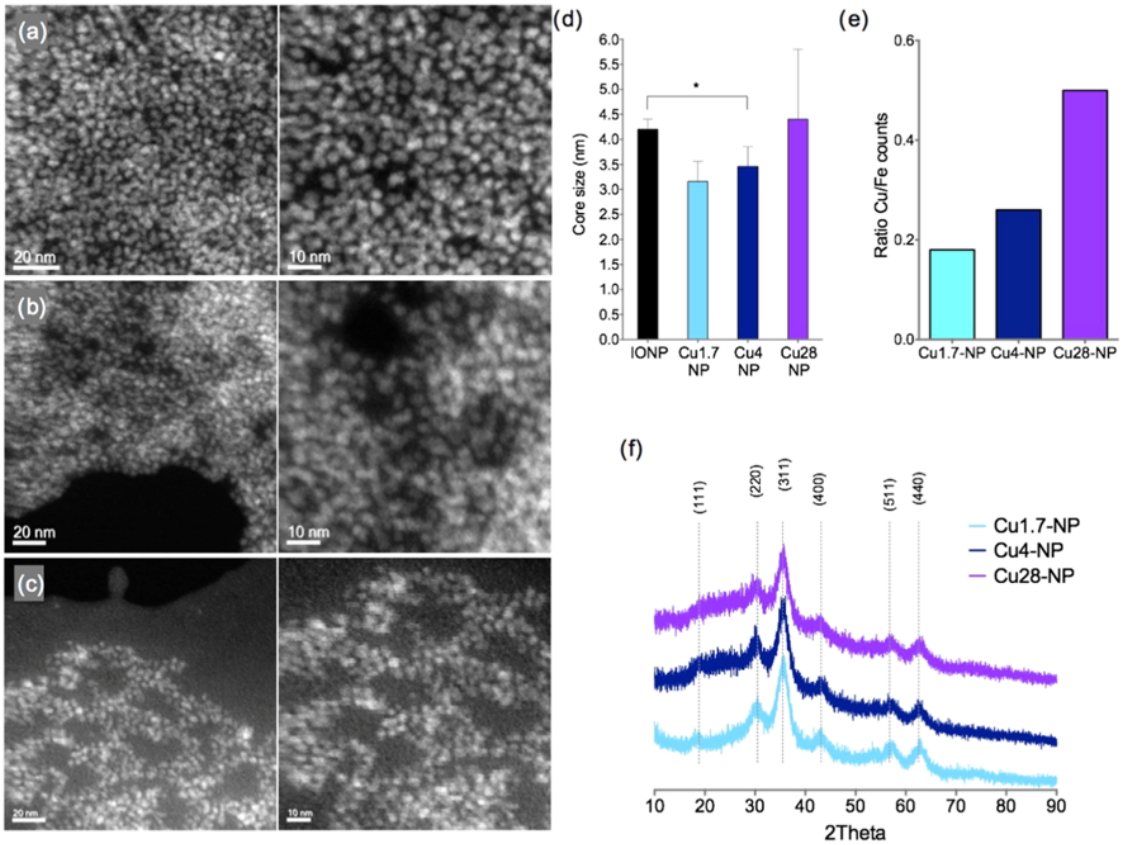

Figure 2. Selected STEM-HAADF images of (a) Cu1.7-NP, (b) Cu4-NP, and (c) Cu28-NP; (d) core size measured by STEM (mean with standard deviation, $N = 30$, $P = 0.01$); (e) ratio of Cu/Fe counts in EDX; and (f) XRD profiles for the three samples.

one-pot synthesis, we have produced Cu core-doped IONP (Cu-NP) with the largest longitudinal relaxivity value described so far, at clinically relevant magnetic fields. We have fully characterized the new nanomaterial and demonstrated its suitability for in vivo use in angiography and targeted molecular imaging for the enhanced diagnosis of tumors in animal models.

2. RESULTS AND DISCUSSION

2.1. One-Pot Microwave-Driven Synthesis of Cu-Doped Hydrophilic Iron Oxide Nanoparticles. Microwave synthesis of nanoparticles is a reliable, reproducible, and extremely fast way for the production of small iron oxide nanoparticles (IONPs). We recently used this approach to tune the relaxivity values of extremely small iron oxide nanoparticles, from T_2 agents to T_1 agents.[3] Here, we have synthesized three different iron oxide nanoparticles with an increasing amount of Cu core doping (Figure 1a). In a typical synthesis, we mixed $FeCl_3$, sodium citrate, and hydrazine with different amounts of $CuCl_2$ (15, 45, and 74 μmol); after 10 min of heating at 120 °C, we purified the nanoparticles by size exclusion chromatography. After purification, we quantified the amount of Cu in the samples by inductively coupled plasma mass spectrometry (ICP-MS): 1.7 mol % (sample Cu1.7-NP), 4 mol % (sample Cu4-NP), and 28 mol % (sample Cu28-NP).

2.2. Physicochemical Characterization of Cu-Doped Iron Oxide Nanoparticles. Hydrodynamic size distributions (Figure 1b) are narrow for all of the samples. Samples IONP, Cu4-NP, and Cu28-NP show the same size distribution, whereas for the sample with the lowest amount of Cu (Cu1.7-NP), the size is smaller. This is confirmed by plotting the *Z*-average values for each sample (Figure 1c). Sample Cu1.7-NP shows a much smaller size (7.7 ± 0.6 nm) than the other nanoparticles in this study; values for IONP, Cu4-NP, and Cu28-NP are 15.0 ± 1.0, 16.1 ± 0.7, and 16.0 ± 1.5 nm, respectively. ζ-Potential measurements show no significant differences between samples (Figure 1d) with homogeneous values around −34 mV as expected for citrate-coated nanoparticles.

FTIR spectra for the three Cu-doped samples show the expected bands (Figure 1e); bands corresponding to citrate coating appear at 1580, 1380, and 1090 cm^{-1}. The band with maxima at 1580 cm^{-1} is wider for Cu28-NP (from 1460 to 1720 cm^{-1}), most likely due to the presence of the Cu−O band that normally appears at around 1640 cm^{-1}. A strong band due to iron oxide is observed in all three spectra at 560 cm^{-1}. Further analysis in the region between 800 and 400 cm^{-1} shows at least a band at a higher wavelength than 600 cm^{-1}, indicating that the sample is mainly composed of maghemite rather than magnetite.[3] Thermogravimetric analysis shows the same curves for the three samples. We found three different steps at around 120, 380, and 480 °C; this mass loss in a stepwise manner is typical of citrate-coated nanoparticles.[27] All samples show a thick organic layer, about 50% of weight loss, which ensures their colloidal stability and the availability of carboxylic groups for bioconjugation.

Electron microscopy of these samples is often difficult; a small core and a thick organic layer complicate acquiring quality images. The same happens with X-ray diffraction

DOI: 10.1021/acsomega.8b03004
ACS Omega 2019, 4, 2719−2727

(XRD), which normally produces broad peaks difficult to identify. To ameliorate this issue, we treated the samples (Cu1.7-NP, Cu4-NP, and Cu28-NP), prior analysis, with the enzyme citrate lyase. This enzyme catalyzes the reversible aldol cleavage of citrate to oxaloacetate and acetate. Our hypothesis was that by cleaving citrate the organic layer would be at least partially reduced so scanning transmission electron microscopy (STEM) images would be better and XRD peaks would be more clearly defined. Figure 2 shows selected STEM-HAADF images of the three samples (more images are shown in the Supporting Information). Images reveal small cores for all of them, similar to IONPs produced with this approach.[3] We can observe individual, dispersed nanoparticles, for all three samples. The core size of the nanoparticles, measured by STEM, also shows that Cu1.7-NP has the lowest value (3.2 ± 0.9 nm) and Cu4-NP has a similar core size (3.5 ± 0.8 nm), whereas IONP (4.2 ± 1.0 nm) and Cu28-NP (4.4 ± 2.9 nm) show the largest values. Interestingly, Cu28-NP, the sample with the largest amount of Cu, shows a much higher heterogeneity than the other nanoparticles in the core size (Figure 2d), which is also reflected in the quality of the images (Figure 2c). Energy dispersive X-ray (EDX) analysis of the samples confirms the results obtained by ICP-MS, an increase in the Cu/Fe ratio from Cu1.7-NP to Cu28-NP (Figure 2e).

The effect of the enzyme is noticeable in the quality of the XRD spectra. A comparison with previous data on IONP, without enzymatic treatment, clearly shows that now the peaks are more defined and easier to identify.[3] The increase in Cu doping results in a slight displacement of the main peak (311) toward larger angles and the decrease of the intensity in the peaks.[15] Using the Scherrer equation, we calculated the crystallite sizes for the three nanoparticles: 2.9 nm for Cu1.7-NP; 3.5 nm for Cu4-NP; and 3.4 nm for Cu28-NP, in good agreement with the core sizes measured by STEM. The field-dependent magnetization data (Figure 3a) show negligible coercivity values for all of the samples, confirming their superparamagnetic behavior. The incorporation of increasing amounts of Cu significantly reduces the saturation magnetization of the sample, even for the smallest amounts of Cu.

Saturation magnetization values are 76.6 ± 0.3 emu g^{-1} Fe + Cu for Cu1.7-NP, 56.2 ± 0.3 emu g^{-1} Fe + Cu for Cu4-NP, and 43.8 ± 0.4 emu g^{-1} Fe + Cu for Cu28-NP, showing the dilution effect given by the increasing proportion of copper. However, if we express the saturation magnetization on iron basis, we obtain 78.2 ± 0.3 emu g^{-1} Fe for Cu1.7-NP, 58.4 ± 0.3 emu g^{-1} Fe for Cu4-NP, and 63.3 ± 0.4 emu g^{-1} Fe for Cu28-NP. This unexpected high value for Cu28-NP supports the core−shell structure for this sample where the excess of Cu is mainly located on the surface of the nanoparticle core. The temperature dependence of the out-of-phase susceptibility shows maxima located in the range between 15 and 22 K for all samples, together with maxima in the in-phase susceptibility at slightly higher temperatures (data not shown) typical of the relaxation procedure of nanoparticles (Figure 3b). The location of the out-of-phase susceptibility is influenced by the size distribution, composition, and aggregation (dipolar interactions) of the particles. A mixture of factors affects our results; the increase in the Cu amount (that would probably reduce the saturation magnetization values and the temperature location of the susceptibility maxima) is associated with an increase in the particle size (Figures 1 and 2) that would have the opposite effect. The negligible out-of-phase susceptibility values at temperatures above 100 K indicate

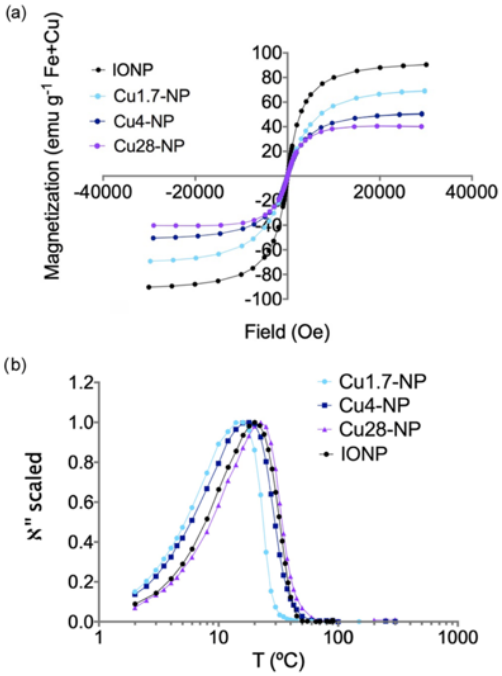

Figure 3. (a) Magnetization curves at 298 K and (b) temperature dependence of AC magnetic susceptibility for IONP, Cu1.7-NP, Cu4-NP, and Cu28-NP.

the superparamagnetic behavior of these particles at room temperature, in agreement with the negligible coercivity observed in the field-dependent magnetization data.

2.3. Relaxometric Characterization of Cu-Doped Nanoparticles. After this comprehensive physicochemical characterization, we focused on our main goal, that is, the study of the effect on the relaxometric values of Cu core doping. Figure 4a−c shows the plot of averaged points for r_2 and r_1 for the three nanoparticles. In all cases, we observe a good linear fitting of the measured points and a good reproducibility. A comparison of the relaxometric values for the three Cu-doped nanoparticles (Figure 4d−f) shows some remarkable results. The longitudinal relaxivity (r_1, Figure 4d) shows that sample Cu4-NP has a large r_1 value (15.7 ± 0.6 mM^{-1} s^{-1}), significantly larger than that for iron oxide nanoparticles (11.9 ± 0.3 mM^{-1} s^{-1}). The r_2 value is also larger for Cu4-NP; however, the r_2/r_1 ratio is pretty low (2.1), in summary, excellent conditions for T_1-weighted magnetic resonance imaging. Sample Cu1.7-NP also shows an improved performance in the longitudinal relaxivity (13.6 ± 0.3 mM^{-1} s^{-1}), compared to that of IONP. The transversal relaxivity value is similar to that for Cu4-NP, and the r_2/r_1 ratio is slightly larger. These properties make Cu1.7-NP also an optimal contrast agent for T_1-weighted imaging, second only to the excellent results for Cu4-NP. Finally, the sample with the largest amount of Cu shows poor performance as an MRI contrast agent. The r_1 value (8.5 ± 1.3 mM^{-1} s^{-1}) is much smaller than the value for IONP, and the r_2/r_1 ratio is the largest for the series (2.4). The relaxometric study shows that, under tested conditions, a 4 mol % doping provides the best properties for an improved T_1 contrast. A large doping percentage, as in Cu28-NP, renders nanoparticles with worse T_1 contrast than that of nanoparticles without doping.

DOI: 10.1021/acsomega.8b03004
ACS Omega 2019, 4, 2719−2727

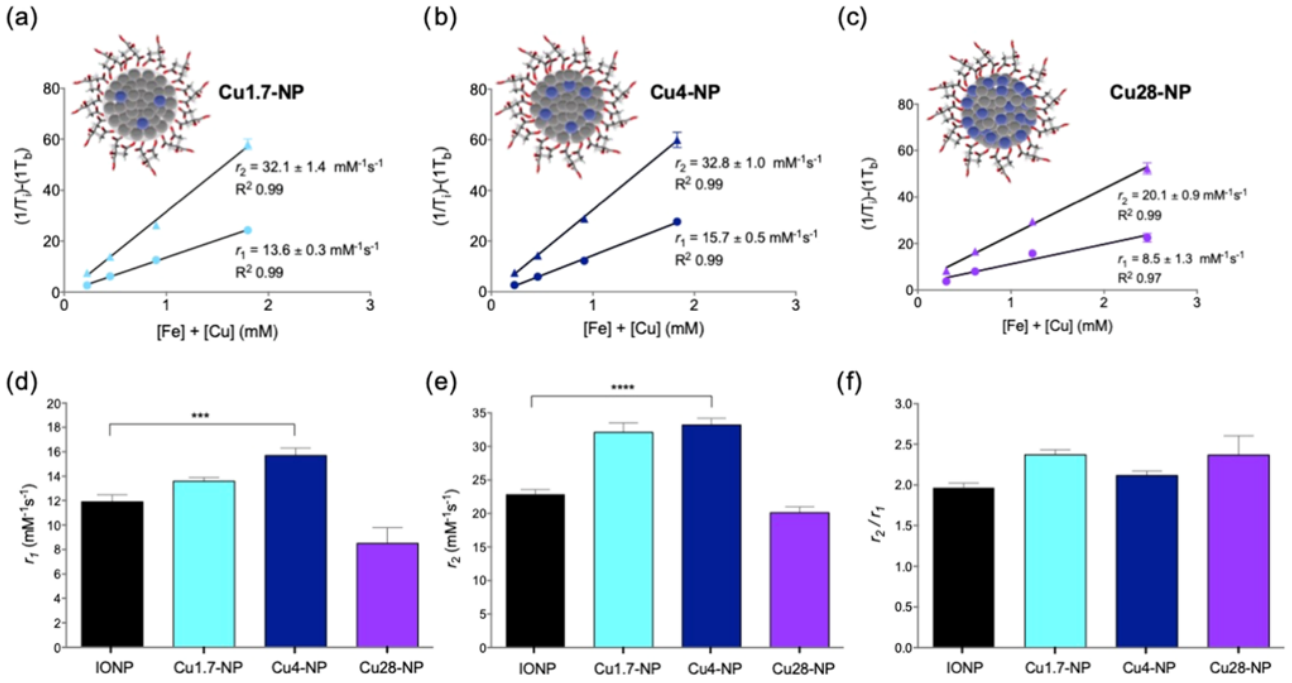

Figure 4. Plots of relaxation rates, T_1 and T_2, against iron and copper concentration for (a) Cu1.7-NP, (b) Cu4-NP, and (c) Cu28-NP. Plots of (d) r_1 (mean with standard deviation, $N = 5$, $P = 0.001$), (e) r_2 (mean with standard deviation, $N = 5$, $P = 0.0001$), and (f) r_2/r_1 for IONP, Cu1.7-NP, Cu4-NP, and Cu28-NP.

Table 1. Relaxometric Properties of Nanoparticles with Large r_1 Values (> 4 mM^{-1} s^{-1})

name	composition	r_1 (mM^{-1} s^{-1})/field (T)	r_2 (mM^{-1} s^{-1})/field (T)	r_2/r_1	core size (nm)	H_D (nm)	references
MnIO	diethylene glycol−BSA−Mn−iron oxide	8.24/0.55	17.95/0.55	2.2	5.0	5.9	9
DIO−Cu	dextran−iron oxide−Cu	17.1/1.4	135.8/1.4	7.9	5.3	45.7	18
$MnFe_2O_4$	polymers−Mn−iron oxide	6.61/4.7	35.92/4.7	5.4	2.2	5.6	8
MION	dextran−iron oxide	16.5/0.47	34.8/0.47	2.1	4.6	20	28
PO−PEG−IO	phosphine oxide−PEG−iron oxide	4.78/3	17.5/3	3.7	2.2	15	25
Fe_2O_3−citrate	citric acid−iron oxide	14.5/1.4	66.9/1.4	4.6	4.8	18	24
PEG_{1100}−IO	PEG_{1100}−iron oxide	13/1.4	42/1.4	3.2	2.8	10	22
Fe_3O_4@SiO_2(Gd−DTPA)	silica−iron oxide−Gd	4.2/3	17.4/3	4.1	27		29
UMIONS	polymers−iron oxide	8.3/4.7	35.1/4.7	4.2	3.3	7.5	20
SPIONS	carboxyPEG−iron oxide	19.7/1.5	39.5/1.5	2.0	5.4	10	21
IONP	citric acid−iron oxide	11.9/1.5	22.9/1.5	1.9	4.2	15.0	3
Cu4-NP	citric acid−Cu-doped iron oxide	15.7/1.5	32.8/1.5	2.1	3.5	16.1	this work

Magnetic measurements suggest a core−shell structure for Cu28-NP, with most of the Cu atoms on the surface; this explains the small r_1 value since Cu atoms on the surface would reduce the contribution of the inner-sphere relaxation mechanism. In Cu1.7-NP, we see an improvement in the T_1 signal but lower than for the 4% doping conditions. It seems that around this doping percentage we obtained the appropriate reduction of the magnetization, keeping enough Fe atoms on the surface. The 1.7% doping is too small to see the full effect, whereas the 28% doping seems too large to keep the desirable relaxometric properties of the iron oxides prepared this way. Surface coating thickness is a key parameter to improve r_1 values, as we have demonstrated before.[3] Cu4-NP coating is thinner than IONP coating; this feature also contributes to increase the longitudinal relaxivity value (Figure S4). The r_1 values shown by Cu4-NP are similar to or larger than those of many clinical Gd- and Mn-based compounds, and Cu4-NP has a low r_2/r_1 ratio.[30] We can compare these results with those of nanoparticles for T_1-weighted MRI published in recent years (Table 1). This table includes not only iron oxide nanoparticles but also Gd- and Mn-based compounds. The performance of an MRI contrast agent for T_1-weighted imaging is based on the r_1 value and the r_2/r_1 ratio. The larger the r_1 value and the smaller the r_2/r_1 ratio, the better. Considering this, Cu4-NPs are one of the best suited nanoparticles for positive contrast MRI thus far reported. These nanoparticles have one of the largest r_1 values and one of the smallest r_2/r_1 ratios. It is noteworthy how the combination of citric acid and iron oxide can produce nanoparticles with large r_1 values but poor r_2/r_1 ratios.[24] One of the few examples of iron oxide nanoparticles doped with Cu shows good relaxometric properties but for T_2-weighted imaging, confirming the nanoparticles must be considered as a whole to optimize the MRI performance. SPIONS[21] and MION[28] show remarkable properties as T_1 agents, with large r_1 values. However, this is usually achieved

DOI: 10.1021/acsomega.8b03004
ACS Omega 2019, 4, 2719−2727

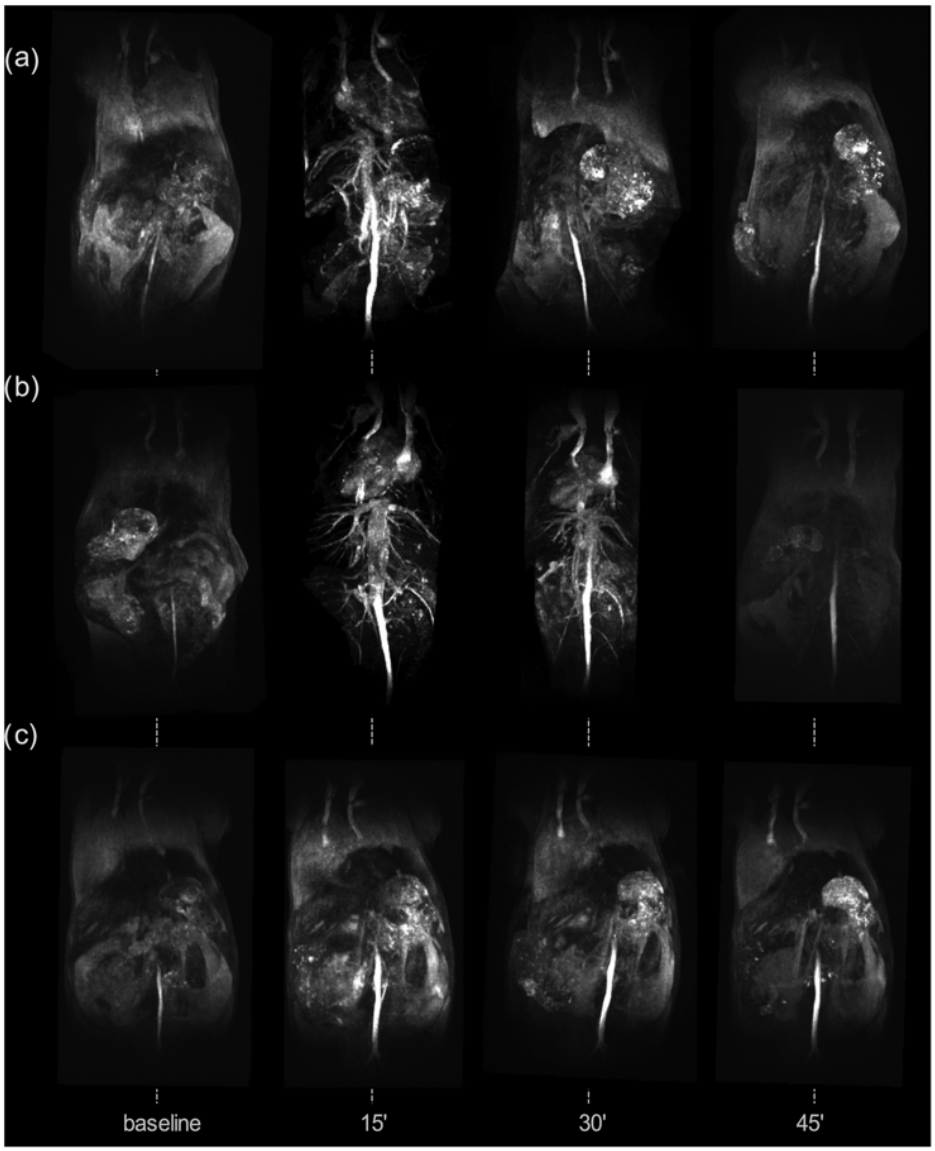

Figure 5. MRI (T_1-weighted imaging) body angiography in healthy mice, before and after the intravenous injection, 0.04 mmol Fe kg^{-1}, of (a) Cu1.7-NP, (b) Cu4-NP, and (c) Cu28-NP.

after a lengthy and time-consuming synthesis and purification. This can compromise the reproducibility and is certainly not the best scenario for clinical translation. These nanoparticles also show a relatively thin organic layer that could complicate their stability under physiological conditions. In the case of Cu4-NP, we achieved one of the best relaxometric properties, in one single step and with a thick organic coating, ensuring their colloidal stability under most relevant physiological conditions.

2.4. Magnetic Resonance Angiography with Cu-Doped Nanoparticles. A good contrast agent for in vivo magnetic resonance imaging must have excellent relaxometric properties. This alone is insufficient, and appropriate in vivo behavior, factors like pharmacokinetics and colloidal stability under physiological conditions, must be checked; for this, the best test is an in vivo image. We carried out magnetic resonance angiography with Cu1.7-NP, Cu4-NP, and Cu28-NP (Figure 5) to check the potential of their T_1 signals. We acquired images before nanoparticle injection (baseline) and 15, 30, and 45 min post injection. The differences between the nanoparticle samples are clear. Angiography with Cu4-NP provides high-quality images with fine details of the vasculature up to 30 min post injection.

The use of Cu1.7-NP provides positive contrast after 15 min, although the signal is not that clear as that for Cu4-NP; then, the signal becomes weaker after 30 min of circulation. We attribute this difference to the r_1 and r_2/r_1 values for Cu4-NP since the circulating time for Cu1.7-NP is similar to that for Cu4-NP (Figure S5), discarding a rapid renal elimination as the cause for this difference. Angiographic images with Cu28-NP show the poorest results due to the smaller r_1 value, half of that for Cu4-NP, and a shorter circulation time.

2.5. Tumor Detection by Magnetic Resonance Imaging: Comparison between IONP and Cu4-NP. We have shown that Cu4-NPs provide an excellent signal in angiographic MRI with adequate in vivo behavior. We wanted to verify the use of this new contrast agent using actively targeted molecular imaging and compare it with the undoped

DOI: 10.1021/acsomega.8b03004
ACS Omega 2019, 4, 2719−2727

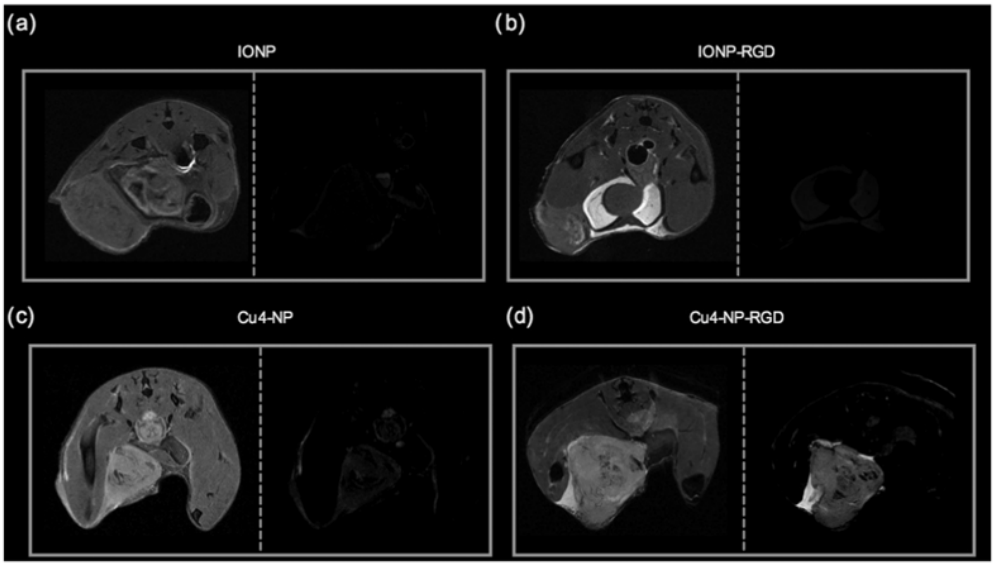

Figure 6. Magnetic resonance imaging of breast tumor-bearing mice allografts 1 h after the intravenous injection of 0.05 mmol Fe kg^{-1} of (a) IONP, (b) IONP−RGD, (c) Cu4-NP, and (d) Cu4-NP−RGD. Left panels show normal contrast images, and right panels are obtained after setting the muscle intensity to 0 to highlight the possible increase in the tumor signal. All MRI images were acquired (see the Experimental Section) with the same parameters.

nanoparticles, IONPs. We designed a classical experiment, that is, targeting vascular angiogenesis toward integrin $\alpha_v\beta_3$ in tumor models using RGD peptide as a vector. We conjugated the peptide on the surface of both IONP and Cu4-NP, which are similar in terms of chemical composition and thickness of the organic layer. Using EDC/sulfoNHS to activate carboxylic groups on the surface, we bound the RGD peptide by amide formation with citric acid carboxylate groups. We measured the hydrodynamic size and ζ-potential for the RGD-functionalized nanoparticles (Figure S6), showing a different value of 31.9 nm for Cu4-NP−RGD and 37.3 nm for IONP−RGD. ζ-Potential values are the same in both cases, suggesting a similar functionalization of the surface (−12.9 mV for Cu4-NP−RGD vs −12.0 mV for IONP−RGD). After RGD quantification on the nanoparticle surface (Bradford assay), we obtained a value of 16.1 RGD molecules per IONP and 15.9 molecules of RGD per Cu4-NP. We performed in vivo MRI experiments in mouse breast cancer allograft models, after the intravenous injection of four different nanoparticles, IONP, Cu4-NP, IONP−RGD, and Cu4-NP−RGD.

Figure 6 shows the MR data obtained 1 h after the intravenous injection of the different NPs. We show images with the normal contrast (left panels in each image) and also setting the muscle contrast intensity to 0 (right panels in each image) to better appreciate the possible increase in the tumor signal. Differences are dramatic. First, we can discard the accumulation of the nanoparticles in the tumor due to the enhanced permeability and retention effect since there is no significant signal in the tumor after the injection of either IONP (Figure 6a) or Cu4-NP (Figure 6c). The situation is different after the injection of the functionalized NPs. The image after the injection of IONP−RGD shows a modest increase in the tumor signal (Figure S7); however, when muscle pixels are set to 0, the tumor is barely distinguishable from this reference. The situation is completely different for Cu4-NP−RGD. Figure 6d (left panel) clearly shows an increase in the signal compared to that from the muscle and also when compared to that in Figure 6c. This signal increase is even more clearly displayed when the muscle intensity is set to 0; the tumor is clearly observable owing to a 30% increase in the MRI signal (Figure S6). The difference in hydrodynamic size between IONP−RGD and Cu4-NP−RGD (Figure S6) can contribute to this difference but in a minor proportion. The main reason for this outstanding result obtained with Cu4-NP−RGD is the very large r_1 value obtained, significantly larger than the r_1 value for the undoped nanoparticles. To further explain this, we measured the relaxivity values for Cu4-NP and IONP at 7 T. We measured r_1 values of 2.7 mM^{-1} s^{-1} for Cu4-NP and 2.8 mM^{-1} s^{-1} for IONP. However, the r_2 values are 38.7 mM^{-1} s^{-1} for Cu4-NP and 88.5 mM^{-1} s^{-1} for IONP. These values permit us to get a good T_1 contrast at a high field with Cu4-NP samples but not with IONP because of the large r_2 value, explaining the large differences observed at 7 T in vivo for tumor detection.

3. CONCLUSIONS

The search for better contrast agents for magnetic resonance imaging has implications for both basic and translational research. The synthesis and application of nanoparticles for positive contrast are particularly interesting since these will boost the use of nanomaterials in this imaging technique, key for many clinical applications. In this work, we show for the first time how the use of Cu, as a dopant, enhances the positive contrast in vivo performance of iron oxide nanoparticles. We have fully characterized the nanoparticles and demonstrated the in vivo use of this nanomaterial, both as a blood pool contrast agent and for targeted molecular imaging, which is key for further development and applications. The relaxometric values, the type of synthesis, and the in vivo performance make Cu4-NP a remarkable candidate for future clinical translation.

4. EXPERIMENTAL SECTION

4.1. Synthesis of IONP−Citrate Samples. A mixture of $FeCl_3{\cdot}6H_2O$ (75 mg) and citric acid trisodium salt (80 mg) was dissolved in water (9 mL). Subsequently, hydrazine

DOI: 10.1021/acsomega.8b03004
ACS Omega 2019, 4, 2719−2727

monohydrate (1 mL) was added and the mixture was rapidly introduced into the microwave. Samples were heated under vigorous stirring at 240 W for 10 min at 120 °C. Once this step was completed, nanoparticles were purified through a gel filtration column (PD10) to eliminate unreacted species and stored in glass vials for further characterization.

4.2. Synthesis of Cu-NP−Citrate Samples. A mixture of $FeCl_3{\cdot}6H_2O$ (75 mg), citric acid trisodium salt (80 mg), and $CuCl_2$ (2, 6, or 10 mg) was dissolved in water (9 mL). Subsequently, hydrazine monohydrate (1 mL) was added and the mixture was rapidly introduced into the microwave. Samples were heated under vigorous stirring at 240 W for 10 min at 120 °C. Once this step was completed, nanoparticles were purified through a gel filtration column (PD10) to eliminate unreacted species and stored in glass vials for further characterization.

4.3. Cu-NP Treatment with Citrate Lyase. Citrate lyase (300 μL, 40 mg mL^{-1} in PBS 1×) was added to 1 mL of each Cu-NP sample. The mixture was kept under vigorous stirring for 90 min at room temperature. Once this step was completed, samples were purified by ultrafiltration using 10 kDa cutoff filters and resuspended in water.

4.4. Synthesis of IONP−RGD. The cycloRGD peptide was covalently attached to carboxyl groups in the citrate coating by EDC/sulfoNHS chemistry, yielding IONP−RGD. 1-Ethyl-3-(3-dimethylaminopropyl)carbodiimide hydrochloride (EDC, 12 mg) and 15 mg of *N*-hydroxysulfosuccinimide (NHS) were added to 5 mL of IONP. The mixture was stirred at room temperature for 30 min and posteriorly purified by ultrafiltration using 30 kDa cutoff filters. Filtered nanoparticles were diluted in buffer 4-(2-hydroxyethyl)-1-piperazineethanesulfonic acid (HEPES) pH 8 to 1.8 mL and 1 mg of cycloRGD was then added and mixture stirred at room temperature for 60 min. Once this step was completed, the sample was purified by ultrafiltration and resuspended in saline.

4.5. Synthesis of Cu-NP−RGD. CycloRGD was covalently attached to carboxyl groups in the citrate coating by EDC/sulfoNHS chemistry, yielding Cu-NP−RGD. 1-Ethyl-3-(3-dimethylaminopropyl)carbodiimide hydrochloride (EDC, 12 mg) and 15 mg of *N*-hydroxysulfosuccinimide (NHS) were added to 5 mL of Cu-NP. The mixture was stirred at room temperature for 30 min and posteriorly purified by ultrafiltration using 30 kDa cutoff filters. Filtered nanoparticles were diluted in buffer HEPES, pH 8, to 1.8 mL and 1 mg of cycloRGD was then added, and the mixture stirred at room temperature for 60 min. Once this step was completed, the sample was purified by ultrafiltration and resuspended in saline.

4.6. IONP and Cu-NP Hydrodynamic Size and ζ-Potential Measurements. Hydrodynamic size and ζ-potential of samples were measured using dynamic light scattering (DLS). A Zetasizer Nano ZS (Malvern Instruments) was used to this end. This device is equipped with a He−Ne laser operating at 633 nm and 4 mW and an avalanche photodiode detector.

4.7. MRI Relaxation Properties of IONP and Cu-NP. Relaxometric properties of the samples were assessed by measuring longitudinal and transverse relaxation times. Four concentrations of each nanoparticle sample were selected, and longitudinal and transversal relaxation times of each one were measured using a Bruker Minispec mq60 contrast agent analyzer at 1.5 T and 37 °C. The r_1 and r_2 values were plotted against the Fe concentration (0, 0.25, 0.5, 1, and 2 mM).

4.8. In Vivo MRI Acquisition. MRI equipment used in this study was an Agilent/Varian scanner (Agilent, Santa Clara, CA) equipped with a DD2 console and an actively shielded 205/120 gradient insert coil with 130 mT m^{-1} maximum gradient strength, a TX/RX volume quadrature coil, and a ^1H circularly polarized transmit−receive volume coil of 35 mm inner diameter and 30 mm active length built by Neos Biotec (Pamplona, Spain). For angiography study, mice weighing 30 g were anesthetized with 2% isoflurane and oxygen before being placed on a thermoregulated (38 °C) mouse bed. An ophthalmic gel was applied in the eyes to prevent retinal damage due to drying. The three-dimensional gradient echo with magnetization transfer contrast (MTC) prepulse MRA was performed with the following parameters: min TR, 12.64 ms; min TE, 2.32 ms; flip angle, 20°; two averages; acquisition matrix, 256 × 192 × 128; MTC flip angle, 810°; duration, 6 ms; and offset frequency, 2000 Hz. For tumor MRI experiments, axial T_1-weighted spin echo images were acquired with the following parameters: TR, 2072 ms; TE, 27.9 ms; NA, 8; matrix, 256 × 256; FOV, 30 × 30 mm^2; 20 consecutive 0.5 mm slices; and spectral width, 125 000 Hz.

■ ASSOCIATED CONTENT

Supporting Information

The Supporting Information is available free of charge on the ACS Publications website at DOI: 10.1021/acsomega.8b03004.

Mice tumor allograft model; physicochemical data of prepared nanoparticles; STEM-HAADF images of Cu1.7-NP, Cu4-NP, and Cu28-NP; TGA curves for Cu1.7-NP, Cu4-NP, Cu28-NP, and IONP; T_1 and T_2 values measured by relaxometry; *Z*-average and ζ-potential values; and percentage of increase in MRI signal intensity (PDF)

■ AUTHOR INFORMATION

Corresponding Author

*E-mail: fherranz@iqm.csic.es.

ORCID

Lucía Gutiérrez: 0000-0003-2366-3598
Sabino Veintemillas-Verdaguer: 0000-0002-3015-1470
María del Puerto Morales: 0000-0002-7290-7029
Fernando Herranz: 0000-0002-3743-0050

Author Contributions

The manuscript was written through contributions of all authors. All authors have given approval to the final version of the manuscript.

Notes

The authors declare no competing financial interest.

■ ACKNOWLEDGMENTS

This study was supported by grants from the Spanish Ministry for Economy and Competitiveness (MEyC) (SAF2016-79593-P, MAT2017-88148-R, and SAF2017-84494-C2-R), Comunidad de Madrid (S2017/BMD-3875), and Instituto de Salud Carlos III (DTS16/00059). L.G. received financial support from the Ramoń y Cajal subprogram (RYC-2014-15512). J.R.-C. acknowledges funding from the Programa Red Guipuzcoana de Ciencia, Tecnología e Información (2018-CIEN-000058-01). I.F.-B. thanks Comunidad de Madrid (B2017/BMD-3875). This work was performed under the Maria de Maeztu

DOI: 10.1021/acsomega.8b03004
ACS Omega 2019, 4, 2719−2727

3.3 Early multimodal diagnosis of atherosclerosis: HAP-multitag, a PET and T_1-MRI contrast nanotracer for the longitudinal characterisation of vascular calcification in atherosclerosis (Article 3)

Atherosclerosis is a chronic inflammatory disease affecting blood vessel walls throughout the body which leads to arterial wall thickening and luminal narrowing.[121,122] Sites with low or variable shear stress, near branching and inner curvatures are most susceptible for atherosclerotic plaque formation.[123] This silent disease remains the leading cause of death in western societies, even though there has been a great progress in prevention and diagnosis over the last decades. It accounts for 23.3 million deaths every year and is the underlying primary cause of acute coronary syndrome and cerebral vascular accident.[124–128] Atherosclerotic plaque is composed by a complex conglomerate of lipids, cholesterol, calcium, macrophages and several other cellular and molecular blood components. Arterial wall gradually thickens to form a plaque that results in arterial lumen narrowing.[129] This causes a drop in the amount of blood supplied to surrounding tissue, commonly affecting the heart and the brain. Vascular microcalcifications are associated to plaque rupture, leading to a potential cardiac event; or playing a role in plaque stabilisation through the formation of macrocalcifications in advanced plaque development.[122,130] Hydroxyapatite (HAP) is the main component of microcalcifications in atherosclerotic plaque, with calcium oxalate monohydrate and β-tricalcium phosphate also present in a minor proportion. The significance of these microcalcifications has triggered the development of imaging probes to detect them *in vivo*. The two main approaches followed to image microcalcifications are [^{18}F]FNa, which is the gold standard in the clinics for PET imaging of microcalcifications, and bisphosphonate-based tracers. Bisphosphonate (BP) -based tracers bind a broader spectrum of calcium salts than [^{18}F]FNa, that only bind HAP. Both types of tracers differ in the accumulation mechanism. On the one hand, ^{18}F in [^{18}F]FNa substitutes a hydroxyl group from the HAP matrix. On the other hand, in BP-based probes, the BP moiety coordinates the Ca atom. The main drawback of both types of probes is the high uptake they present in bone, which often complicates vasculature discrimination.[131] This limitation is overcome in large animal models and humans by selecting regions of interest (ROIs) in image acquisition or post-processing steps, however this is not practical for small animal models where vasculature is extremely small and PET resolution flawed. For this reason, examples in the literature of microcalcification detection in mouse models exclusively include breast cancer and chronic tuberculosis.[132–134] Imaging modality is another key aspect in vascular microcalcification detection. Current probes are mostly based on PET, that offers outstanding sensitivity but poor spatial resolution. The combination of PET and MRI seems the most favourable, since it brings together PET's unparalleled sensitivity with the excellent resolution provided by MRI, with a higher morphological soft tissue contrast and eliminates the ionising radiation dose the patient is exposed to during CT. [135,136]

In this paper we propose the use of a bisphosphonate-based PET/MRI nanotracer, based in our citrate-coated ^{68}Ga-IONPs, termed HAP-multitag, to visualise microcalcifications at different plaque development stages in a murine model. For that, our citrate-coated ^{68}Ga core-doped IONPs were functionalised with

alendronate via EDC/sulfoNHS chemistry. Exhaustive characterisation of the functionalised nanoparticles was carried out indicating successful alendronate binding and that HAP-multitag is radiochemically stable and with adequate relaxometric properties for T_1 MRI. The interaction of HAP-multitag with calcium salts that are often present in vascular microcalcifications were studied *in vitro* to confirm the specific binding capabilities of HAP-multitag to calcium. These confirmed the interactions for HAP-multitag but not for non-functionalised ^{68}Ga-IONPs and revealed high nanotracer binding even at low calcium salt concentrations. *In vivo* PET and MR imaging experiments revealed HAP-multitag is able to detect microcalcifications in mice with atherosclerosis. HAP-multitag accumulation is dependent on plaque progression due to mice age and feeding on HFD and hence in plaque calcification stage. It is low in mice 12 weeks old, as the amount of microcalcifications is small and not enough to show a significant HAP-multitag uptake. As mice grow older and reach 16 weeks, there is an increase in HAP-multitag accumulation, indicating the presence of increasing microcalcifications. As mice grow older and microscopic calcium deposits grow reducing their active surface, HAP-multitag uptake is decreased, as can be seen in mice 24 and 26 weeks old. Maximum HAP-multitag uptake is the earliest reported to our knowledge, in mice 16 weeks old under a high fat diet.

The *in vitro* affinity of HAP-multitag for calcium salts translates into an *in vivo* uptake dependent upon mice age and therefore calcification stage of atherosclerotic plaque. We characterised this interaction *in vitro* and *in vivo*, showing a massive uptake in the atherosclerotic lesion identified by PET and positive contrast MRI. This is the first time, that we know of, that atherosclerosis is detected in animals as young as these using positive contrast with iron oxide nanoparticles. This is particularly relevant since obtaining positive contrast in circulating nanoparticles, MR angiography, is considerably easier than demonstrating this bright signal in a localised spot due to the accumulation of the probe.

ACS APPLIED MATERIALS & INTERFACES

September 29, 2021
Volume 13
Number 38
pubs.acs.org/acsami

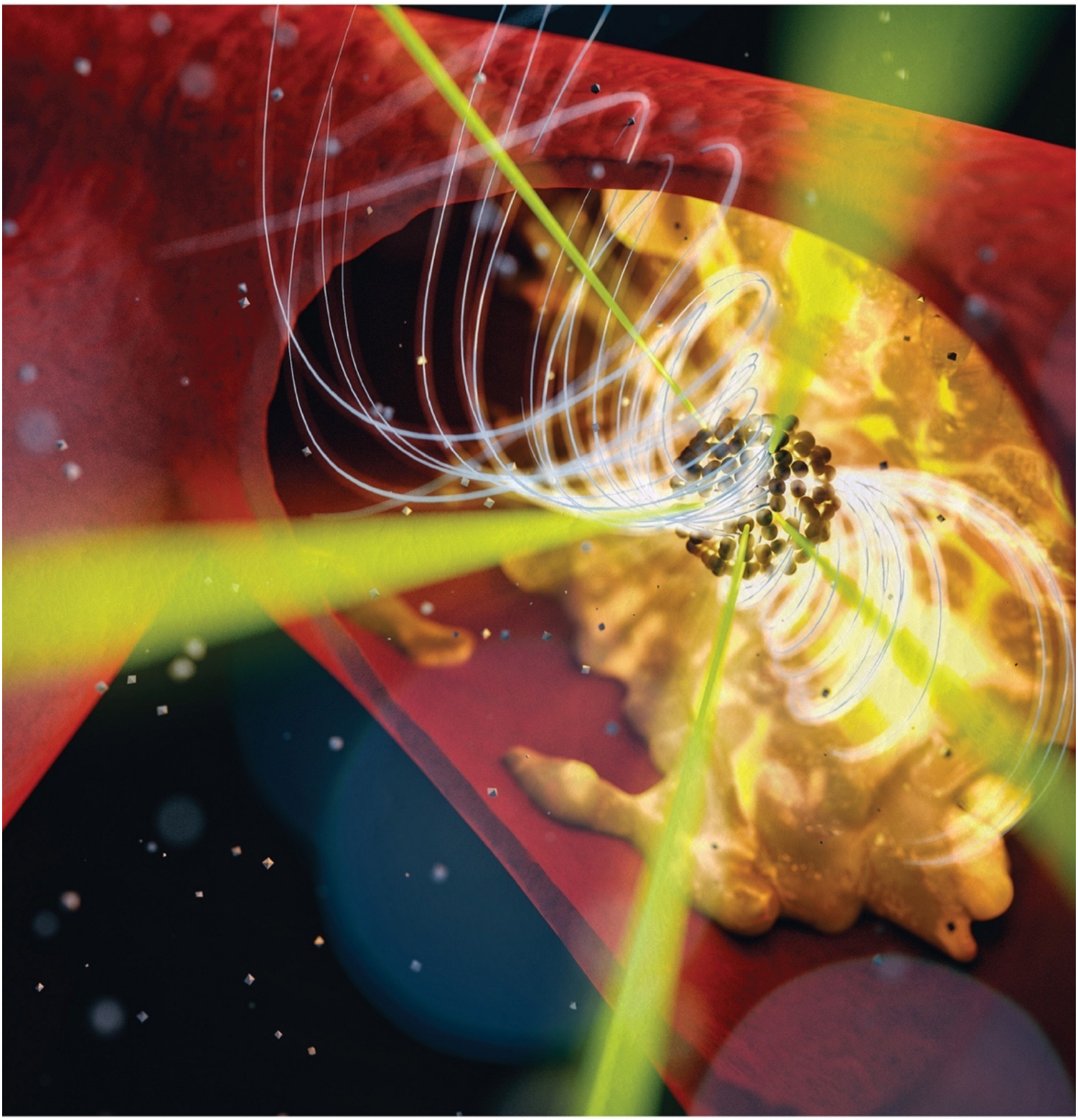

ACS Publications
Most Trusted. Most Cited. Most Read.

www.acs.org

ACS APPLIED MATERIALS & INTERFACES

www.acsami.org

Research Article

HAP-Multitag, a PET and Positive MRI Contrast Nanotracer for the Longitudinal Characterization of Vascular Calcifications in Atherosclerosis

Juan Pellico,[○] Irene Fernández-Barahona,[○] Jesús Ruiz-Cabello, Lucía Gutiérrez, María Muñoz-Hernando, María J. Sánchez-Guisado, Irati Aiestaran-Zelaia, Lydia Martínez-Parra, Ignacio Rodríguez, Jacob Bentzon, and Fernando Herranz*

Cite This: *ACS Appl. Mater. Interfaces* 2021, 13, 45279−45290

Read Online

ACCESS | Metrics & More | Article Recommendations | Supporting Information

ABSTRACT: Vascular microcalcifications are associated with atherosclerosis plaque instability and, therefore, to increased mortality. Because of this key role, several imaging probes have been developed for their *in vivo* identification. Among them, [^{18}F]FNa is the gold standard, showing a large uptake in the whole skeleton by positron emission tomography. Here, we push the field toward the combined anatomical and functional early characterization of atherosclerosis. For this, we have developed hydroxyapatite (HAP)-multitag, a bisphosphonate-functionalized ^{68}Ga core-doped magnetic nanoparticle showing high affinity toward most common calcium salts present in microcalcifications, particularly HAP. We characterized this interaction *in vitro* and *in vivo*, showing a massive uptake in the atherosclerotic lesion identified by positron emission tomography (PET) and positive contrast magnetic resonance imaging (MRI). In addition, this accumulation was found to be dependent on the calcification progression, with a maximum uptake in the microcalcification stage. These results confirmed the ability of HAP-multitag to identify vascular calcifications by PET/(T_1)MRI during the vulnerable stages of the plaque progression.

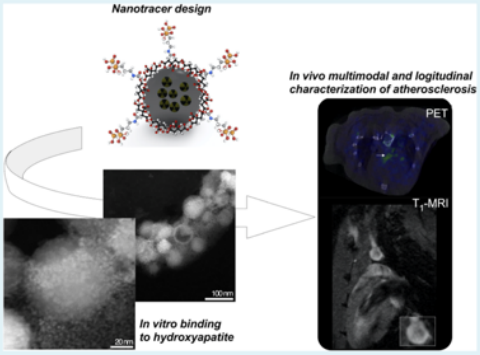

KEYWORDS: *vascular calcifications, nanotracer, PET/MRI, hydroxyapatite, atherosclerosis*

INTRODUCTION

Atherosclerosis is a complex chronic inflammatory disease of the blood vessel wall in which plaques build up inside the arteries and is the leading cause of cardiovascular diseases. It is well known that the formation of calcified nodules is an important process in atherosclerosis development, often after a first inflammation step.[1] These microcalcifications are associated with plaque rupture, leading to a cardiac event, or with plaque stabilization through the formation of macroscopic crystals (macrocalcifications) later in plaque development.[1,2] Atherosclerosis microcalcifications are mainly composed of a mixture of hydroxyapatite (HAP), calcium oxalate monohydrate, and β-tricalcium phosphate, with HAP as the major component.[3] Due to the relevance of these microcalcifications, several imaging probes have been developed in the past years. There are two main approaches to develop tracers for *in vivo* detection of calcifications: the use of [^{18}F]FNa and bisphosphonate-based tracers. [^{18}F]FNa is the gold standard for positron emission tomography (PET) detection of calcifications in the clinical scenario owing to the favorable pharmacokinetic profile and the lack of toxic effects.[4] On the other hand, the [^{18}F]FNa only binds to HAP, while bisphosphonate-based (BP) tracers or nanoparticles recognize a broader spectrum of calcium salts, relevant in several diseases.[5−8] The mechanism of accumulation in calcifications is different for both types of tracers: in the case of [^{18}F]FNa, ^{18}F substitutes one hydroxyl group in the HAP matrix, forming fluorapatite, while when using BP-based probes, the bisphosphonate moiety coordinates with the Ca atom. When using [^{18}F]FNa or BP-based tracers, one of the main drawbacks is the high uptake they show in the bone, increasing the off-target signal, often complicating vasculature differentiation.[9] If the main focus is atherosclerosis, using a tracer for which the bone signal is minimized is highly desirable for imaging purposes. This limitation is overcome in humans and large animal models by selecting regions of interest (ROIs) in the imaging acquisition or post-processing steps. However, this strategy is impractical in small animal models where the vasculature is extremely small and PET resolution, even when

Received: July 15, 2021
Accepted: September 9, 2021
Published: September 16, 2021

Scheme 1. Microwave Two-Step Synthesis of ^{68}Ga-IONP-Alendronate (HAP-Multitag Probe)

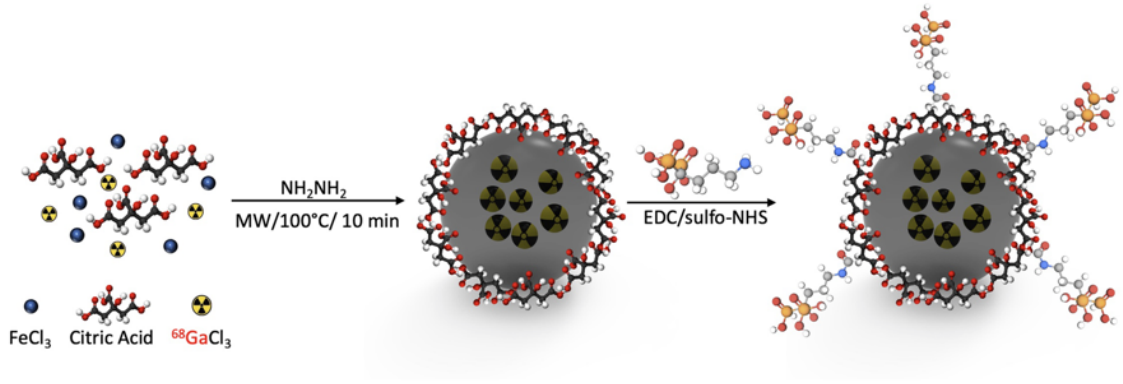

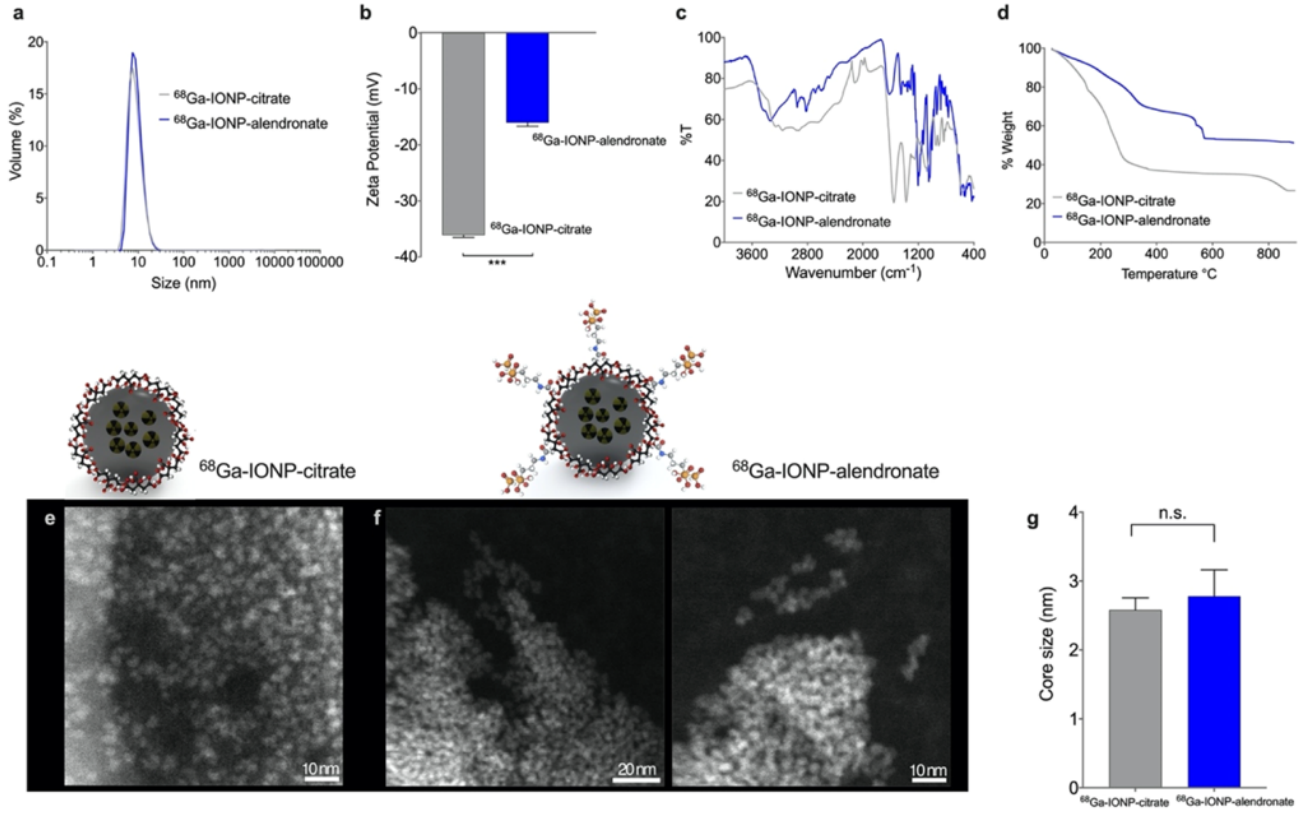

Figure 1. (a) DLS measurements for ^{68}Ga-IONP-citrate and ^{68}Ga-IONP-alendronate; (b) *Z*-potential (mV) of ^{68}Ga-IONP-citrate and ^{68}Ga-IONP-alendronate, $N = 3$, $^{***}P < 0.001$; (c) FTIR spectra of ^{68}Ga-IONP-citrate and ^{68}Ga-IONP-alendronate; (d) TGA of ^{68}Ga-IONP-citrate and ^{68}Ga-IONP-alendronate; (e) selected STEM-HAADF image of ^{68}Ga-IONP-citrate; (f) selected STEM-HAADF image of ^{68}Ga-IONP-alendronate; and (g) core size measured for ^{68}Ga-IONP-citrate and ^{68}Ga-IONP-alendronate. $N = 50$ per sample, n.s., $P > 0.46$.

combined with computed tomography (CT), is flawed. Examples of microcalcification detection in mice have been exclusively described in breast cancer and chronic tuberculous models.[10−12]

A second key aspect is the imaging modality. Current probes for vascular calcification detection are mainly based on nuclear imaging techniques, particularly PET. This technique offers unparalleled sensitivity but poor spatial resolution. For this reason, PET scanners are combined with CT and, more recently, with magnetic resonance imaging (MRI) scanners, providing detailed functional and anatomical information with micron resolution.[13] The combination of PET with MRI is arguably the most convenient since it pieces together the extraordinary sensitivity of PET with the excellent resolution of MRI.[14,15] The development of this technology is associated with the design of novel probes, providing signals in both imaging techniques. Among the different chemical compounds used to produce dual PET/MRI probes, iron oxide nanoparticles (IONPs) possess several advantages and one major drawback. IONPs are biocompatible and easy to produce, and there are a large variety of possible coatings to tune their bioconjugation and biodistribution.[16] IONPs have a single drawback for this application; however, it is a major one: the typical signal they provide is T_2-based, negative, or dark. This option complicates *in vivo* uptake identification, particularly in regions where an endogenous dark signal is present, like

https://doi.org/10.1021/acsami.1c13417
ACS Appl. Mater. Interfaces 2021, 13, 45279−45290

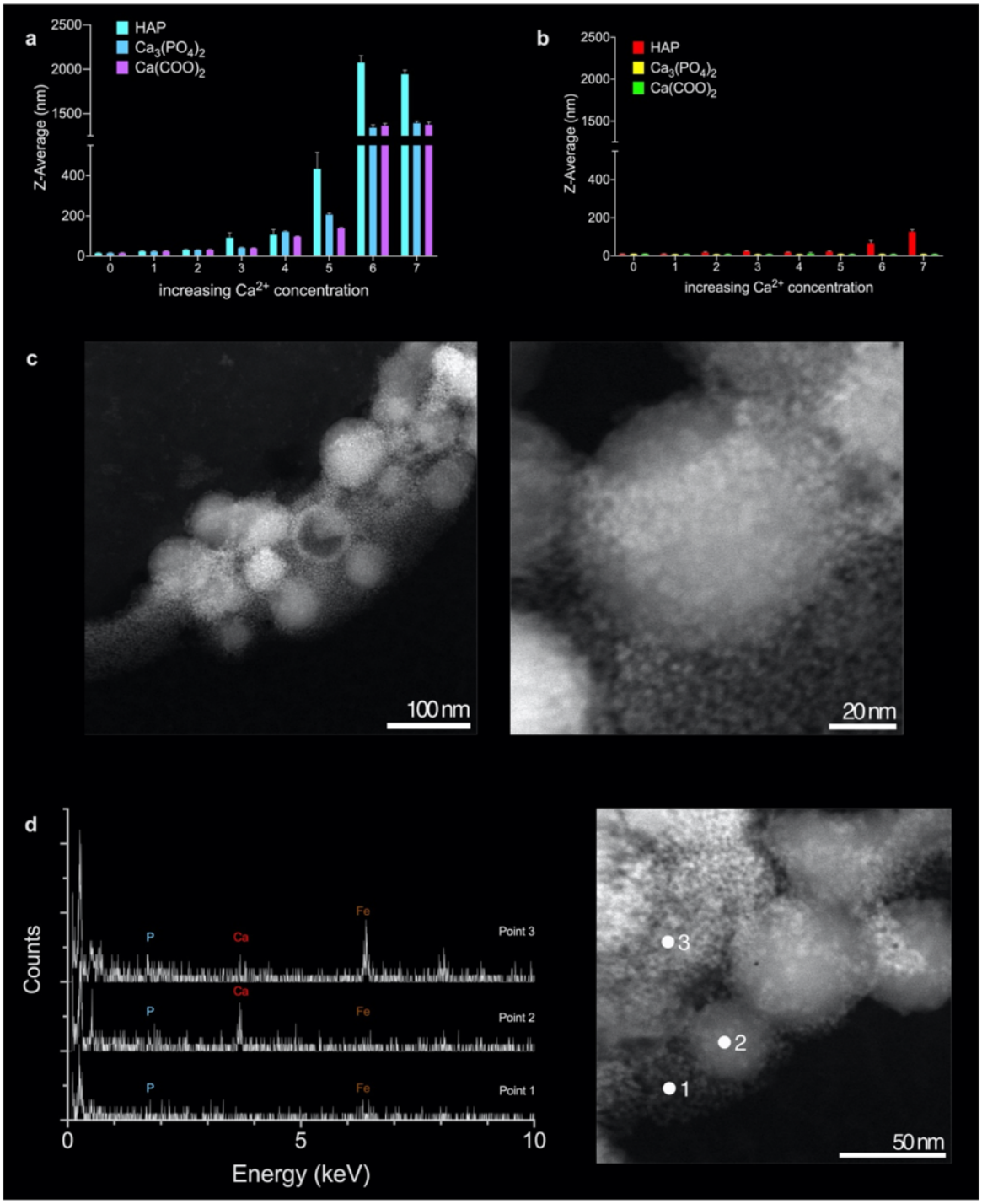

Figure 2. (a) Change in hydrodynamic size for ^{68}Ga-IONP-alendronate upon the increase in the concentration of HAP, β-tricalcium phosphate, and calcium oxalate monohydrate; (b) change in hydrodynamic size for ^{68}Ga-IONP-citrate upon the increase in the concentration of HAP, β-tricalcium phosphate, and calcium oxalate monohydrate; (c) STEM-HAADF images for the combination of ^{68}Ga-IONP-alendronate with HAP; (d) EDX spectra for the three points indicated, in red, in the STEM-HAADF image.

calcified vascular areas. This problem has drastically limited their use, especially in the clinical area, in molecular imaging or multimodal approaches. This void has boosted the quest for IONPs providing positive contrast in MRI, with several examples in the literature where positive contrast is achieved by tuning the core size,[17,18] coating thickness,[19] or core composition.[20] Most of the time, the positive contrast is demonstrated by *in vivo* MR angiography. The dilution and sample redispersion in a large blood volume reduce the T_2 effect, favoring the generation of positive contrast. However, examples of positive contrast in which IONPs accumulate in a specific tissue or organ are scarce.[20]

Here, we use bisphosphonate-based ^{68}Ga-core-doped IONPs that we termed HAP-multitag, with several key

https://doi.org/10.1021/acsami.1c13417
ACS Appl. Mater. Interfaces 2021, 13, 45279−45290

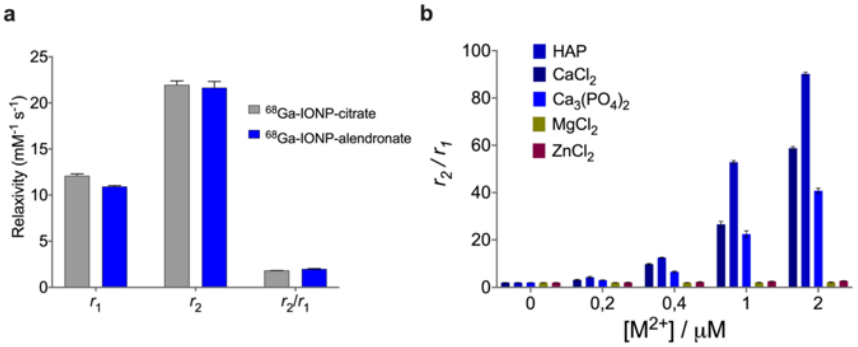

Figure 3. (a) r_1, r_2, and r_2/r_1 ratio for ^{68}Ga-IONP-citrate and ^{68}Ga-IONP-alendronate and (b) r_2/r_1 ratio of ^{68}Ga-IONP-alendronate incubated with different concentrations of calcium, magnesium, and zinc salts.

features: they provide a simultaneous signal in PET and —positive contrast—MRI. HAP-multitag binds predominantly to HAP and other calcium salts relevant to vascular calcification, as demonstrated *in vitro* by different techniques. *In vivo*, HAP-multitag accumulation in atherosclerotic lesions can be monitored by PET and positive contrast MRI techniques. Finally, the accumulation is dependent on the stage of lesion development, which further demonstrates the ability of HAP-multitag to diagnose and longitudinally characterize atherosclerotic lesions by PET/(T_1)MRI in mice.

RESULTS AND DISCUSSION

Synthesis and Characterization of ^{68}Ga-IONP-Alendronate. We synthesized HAP-multitag (^{68}Ga-IONP-alendronate) in a two-step synthetic procedure (Scheme 1). First, a microwave-driven protocol rendered ^{68}Ga-core-doped IONPs coated with citric acid (^{68}Ga-IONP-citrate). This methodology, previously reported by our group, produces ^{68}Ga-nanoparticles with high radiolabeling yield, high radiochemical purity and stability, and large r_1 values, ensuring a remarkable response in both PET and positive contrast MRI.[21] Then, we coupled the bisphosphonate moiety (alendronate sodium) by *N*-(3-dimethylaminopropyl)-*N*′-ethylcarbodiimide hydrochloride (EDC)/sulfo-NHS chemistry.[22]

After purification by size-exclusion chromatography, we analyzed the physicochemical properties of the radiolabeled nanoparticles. Dynamic light scattering (DLS) measurements show no differences between ^{68}Ga-IONP-citrate and ^{68}Ga-IONP-alendronate samples (Figure 1a), indicating no aggregation after the bioconjugation step, as expected for these hydrophilic nanoparticles when using EDC and sulfo-NHS as coupling agents. *Z*-potential measurement shows a significant reduction in the value of the superficial charge for ^{68}Ga-IONP-alendronate (Figure 1b). The integration of the bisphosphonate moiety into the nanoparticle was confirmed by Fourier transform infrared (FTIR) spectroscopy (Figure 1c). The ^{68}Ga-IONP-alendronate spectrum shows a new area with multiple peaks of strong intensity between 1250 and 900 cm^{-1} corresponding to the vibration modes of P═O and P−OH groups and new weaker peaks between 2700 and 2200 cm^{-1} attributed to the O−H stretches of the O═P−OH groups.[23] Thermogravimetric analysis (TGA) (Figure 1d) further confirms the conjugation of alendronate to the surface of ^{68}Ga-IONP-citrate, with the step between 540 and 590 °C corresponding to the covalent bond between citric acid and alendronate. According to TGA, the reduction in the organic coating, around 18%, can be attributed to the loss of citrate molecules from the surface in the second reaction and purification steps. This result (together with some exchange of citrate molecules by bisphosphonate moieties, exposing free amines) would also explain the reduction in the negative charge observed for ^{68}Ga-IONP-alendronate in comparison to ^{68}Ga-IONP-citrate. Using TGA information for ^{68}Ga-IONP-alendronate, we calculated that each nanoparticle has been functionalized with approximately 140 molecules of alendronate. Finally, we studied ^{68}Ga-IONP-citrate and ^{68}Ga-IONP-alendronate by electron microscopy. Since these nanoparticles consist of an extremely small iron oxide core and a large organic coating, electron microscopy images are not easily obtained.

Using scanning transmission electron microscopy high-angle annular dark-field imaging (STEM-HAADF), it is possible to observe the small iron oxide cores without apparent aggregation for ^{68}Ga-IONP-citrate (Figure 1e) and ^{68}Ga-IONP-alendronate (Figure 1f). Analysis of the core sizes shows similar sizes for both nanoparticles, 2.6 ± 0.3 nm for ^{68}Ga-IONP-citrate, and 2.8 ± 0.7 nm for ^{68}Ga-IONP-alendronate.

Qualitative Assessment of the Binding between ^{68}Ga-IONP-Alendronate and Calcium Salts. To assess the interaction between ^{68}Ga-IONP-alendronate and calcium salts, we chose those normally present in the microcalcifications structure, that is, HAP, calcium oxalate monohydrate, and *β*-tricalcium phosphate. First, we used DLS; by measuring the hydrodynamic size of the nanoparticles with increasing amounts of the calcium salts, it is possible to assess whether they are interacting or not.[24,25] We incubated ^{68}Ga-IONP-alendronate with the aforementioned salts and measured their hydrodynamic size (Figure 2a), and a similar procedure was followed with ^{68}Ga-IONP-citrate (Figure 2b). The *Z*-average value clearly shows the aggregation of ^{68}Ga-IONP-alendronate as the concentration of each salt increases. This is particularly true for HAP, which shows a very large hydrodynamic size value, around 2000 nm, for the highest concentration of the calcium salt. Similarly, the interaction with the other two salts, $Ca_3(PO_4)_2$ and $Ca(COO)_2$, is clearly reflected in the aggregation of the nanoparticles. As a control, we performed the same titrations but using ^{68}Ga-IONP-citrate. In this case (Figure 2b), there is no aggregation when using the same calcium salts, as reflected in the constant value of hydrodynamic size (Figure 2a,b has the same scale in the *Y*-axis for better comparison). In fact, the size measured for the highest concentration of HAP with ^{68}Ga-IONP-citrate reflects the presence of the HAP nanoparticles (with a size around 300 nm) rather than an interaction between the calcium salt and

https://doi.org/10.1021/acsami.1c13417
ACS Appl. Mater. Interfaces 2021, 13, 45279−45290

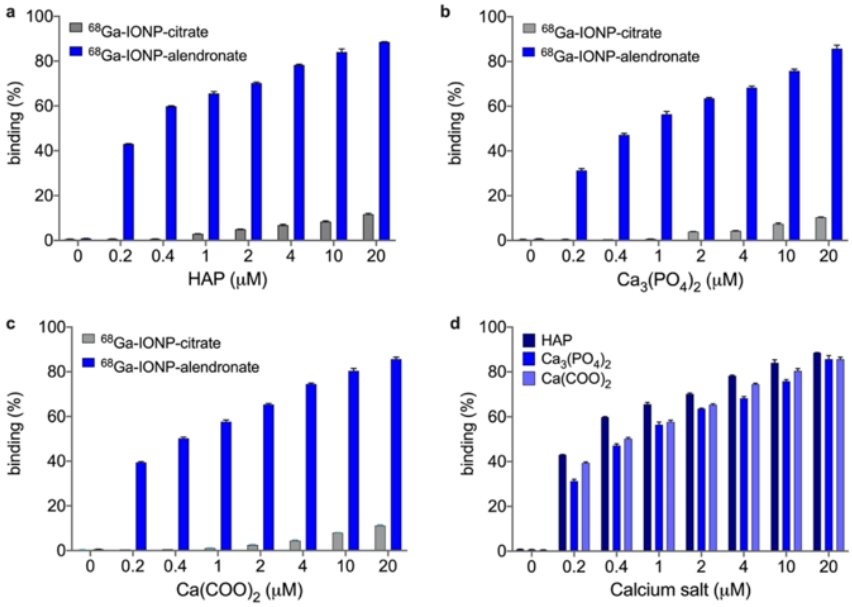

Figure 4. Percentage of binding between ^{68}Ga-IONP-citrate and ^{68}Ga-IONP-alendronate and (a) HAP, (b) $Ca_3(PO_4)_2$, and (c) $Ca(COO)_2$; (d) comparison of the binding between ^{68}Ga-IONP-alendronate and the three calcium salts (60 min of incubation).

the citrate nanoparticles. This result is further demonstrated by the quantitative analysis (see below).

Then, we used STEM-HAADF to analyze the interaction between ^{68}Ga-IONP-alendronate and HAP. Figure 2c shows the large HAP particles surrounded by the much smaller, ^{68}Ga-IONP-alendronate nanoparticles, indicating their affinity toward the salt (more images in Figure S1). Zooming in the image, it is possible to see a single HAP particle completely surrounded by the much smaller ^{68}Ga-IONP-alendronate nanoparticles. This was further confirmed by energy-dispersive X-ray microanalysis (EDX) analysis. Analyzing three different points, we can see the presence of Fe and P, when only ^{68}Ga-IONP-alendronate is studied (point 1), the presence of large amounts of Ca when HAP with few surrounding ^{68}Ga-IONP-alendronate particles is studied (point 2), also with Fe and P, and finally the presence of Fe, Ca, and P, in point 3, where many aggregated ^{68}Ga-IONP-alendronate nanoparticles surround an HAP particle.

Relaxometry. Relaxometry of ^{68}Ga-IONP-alendronate was carried out to confirm the positive contrast capabilities of the nanotracer and to assess the selectivity toward Ca^{2+} salts. Figure 3a shows the r_1, r_2, and r_2/r_1 values for ^{68}Ga-IONP-citrate and ^{68}Ga-IONP-alendronate, measured at 1.5 T. As expected, both nanotracers show positive contrast features with large r_1 values and small r_2 values, which produces r_2/r_1 values smaller than 2. At 1.5 T, the ^{68}Ga-IONP-alendronate r_1 value was 10.9 ± 0.1 mM^{-1} s^{-1}, while the r_2 value was 22.0 ± 0.4 mM^{-1} s^{-1}, rendering a r_2/r_1 ratio of 1.98 ± 0.05. Figure 3b shows the r_2/r_1 ratio for ^{68}Ga-IONP-alendronate as a function of the metal concentration for different salts. As expected, titration with Ca^{2+} salts produces an increase in the r_2/r_1 due to the aggregation of the nanotracer; while this reduces the T1 capabilities of the nanotracer, it would only be a problem for concentrations much larger than those we can find *in vivo*, as will be shown in the MRI experiments. Finally, the r_2/r_1 values when using Mg^{2+} or Zn^{2+} remain unchanged, confirming the well-known selectivity of bisphosphonate-functionalized nanoparticles toward Ca^{2+}.

Quantitative Assessment of the Binding between ^{68}Ga-IONP-Alendronate and Calcium Salts. Next, we quantitively assessed the interaction between ^{68}Ga-IONP-alendronate and ^{68}Ga-IONP-citrate with the three calcium salts often present in vascular calcifications: HAP, $Ca_3(PO_4)_2$, and $Ca(COO)_2$ (Figure 3). For this, we covalently attached to the surface of the nanotracers a fluorescent dye (Alexa 647). The nanotracers were incubated with the different salts and purified by ultrafiltration, and the fluorescence of the supernatant was quantified at each point. The percentage of binding was calculated using the initial and final fluorescence intensities of the supernatant (see the Experimental Section).

These titrations confirm several aspects: first, in agreement with the DLS data, the interaction between ^{68}Ga-IONP-citrate and the different salts is negligible, a mere 11% for the largest HAP concentration (20 μM). On the contrary, titrations with ^{68}Ga-IONP-alendronate clearly show a strong interaction, explaining the large aggregation observed in DLS and electron microscopy. For example, for a low concentration of HAP of 0.2 μM, the percentage of binding is already 43%; almost half of the nanotracer sample has bound the salt at this concentration (Figure 4a). Similarly, for the other salts (Figure 4b,c), there is large binding of the alendronate nanotracer without an appreciable interaction with the citrate nanoparticles. Finally, a similar profile was observed for the interaction of ^{68}Ga-IONP-alendronate with $Ca_3(PO_4)_2$ and ^{68}Ga-IONP-alendronate with $Ca(COO)_2$ (Figure 4d), with a slightly stronger interaction with HAP. For example, for the lowest calcium concentration, the percentages of binding are 43% with HAP, 31% with $Ca_3(PO_4)_2$, and 39% with $Ca(COO)_2$, confirming that this nanotracer presents a broad spectrum of interactions with calcium salts and not just limited to HAP, as is the case for [^{18}F]FNa.

Biodistribution of ^{68}Ga-IONP-Alendronate, HAP-Multitag. After characterizing the *in vitro* interaction between ^{68}Ga-IONP-alendronate and the selected calcium salts, we tested its performance to diagnose atherosclerosis. First,

https://doi.org/10.1021/acsami.1c13417
ACS Appl. Mater. Interfaces 2021, 13, 45279−45290

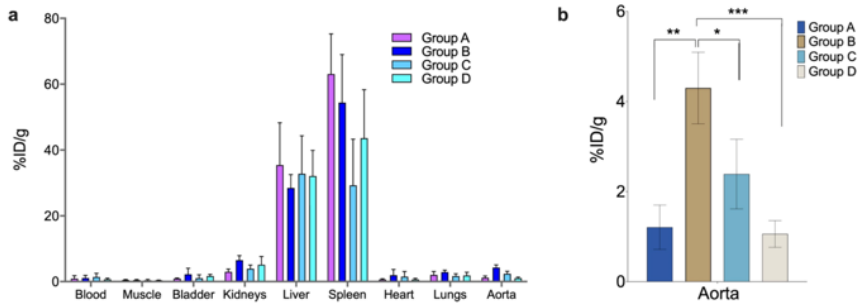

Figure 5. (a) Distribution of HAP-multitag measured in a gamma counter expressed as the percentage injected dose per gram (%ID/g) in ApoE$^{-/-}$ mice (N = 5) of groups A–D; (b) aorta uptake of HAP-multitag showing significant differences between mice groups. *P < 0.05, **P < 0.01, ***P < 0.001, one-way ANOVA; error bars indicate s.d., N = 5.

biodistribution experiments were conducted to evaluate whether HAP-multitag has any affinity toward atherosclerotic plaques in mice. Atherosclerotic ApoE$^{-/-}$ mice were selected as the disease model. The development of hypercholesterolemia triggering aortic and carotid artery lesions throughout ApoE$^{-/-}$ mice aging and high fat diet is well established.[26] A longitudinal study was carried out in mice between 12 and 26 weeks of age. In addition, mice were fed with high-cholesterol diet from 8 weeks old onward to accelerate atherosclerosis progression.[27] A complete biodistribution study was performed in a gamma counter after intravenous injection of ^{68}Ga-IONP-alendronate in ApoE$^{-/-}$ mice. We studied four different groups: 12 weeks old and fed 4 weeks with a high-fat cholesterol diet (HFD) (group A), 16 weeks old and 8 weeks HFD (group B), 24 weeks old and 16 weeks HFD (group C), and 26 weeks old and 18 weeks HFD (group D) (Figure 5a). Main organs, blood, and perfused aortas were evaluated in five mice of each group. Uptake values, calculated as the percentage of injected dose per gram of tissue, showed the liver and spleen as the organs with the highest accumulation. This is an expected result since biodistribution and clearance studies of IONPs have demonstrated the liver and spleen as the main uptake organs.[28]

Aortas show an important uptake with significant differences following mice aging and hence atherosclerosis progression (Figure 5b). Negligible blood circulation of the nanoparticles (<1.5 %ID/g) and the aortas' perfusion, prior to the measurement, ensure that the signal measured in the aorta is due to nanoparticle uptake. Figure 5b shows the uptake of the nanoparticles in the aorta depending on the mice's age. The HAP-multitag uptake is similar for the youngest and oldest mice, with a maximum for 16 weeks old mice. This observation may have important consequences for atherosclerosis characterization. First, this profile appears to follow the reported calcification process: initially, the amount of microcalcifications is too low to show a significant uptake—at 12 weeks; then, as more microcalcifications accumulate, an increase in the nanotracer uptake is observed—at 16 weeks; finally, the growth of the calcified deposits, and the concurrent reduction of the active surface, translates in a reduction of the nanotracer uptake, a process well known for other tracers.[4] Similarly, [^{18}F]FNa uptake appears to be inversely dependent on calcification growth.[29,30] Second, the maximum uptake for HAP-multitag is the earliest reported, allowing for very early diagnosis of atherosclerosis. For comparison, the maximum uptake for [^{18}F]FNa is reported in ApoE$^{-/-}$ mice at 30 weeks old under high fat diet.[31]

***In Vivo* Multimodal Imaging of Atherosclerosis with HAP-Multitag.** *PET/CT Imaging.* Encouraged by the biodistribution results, we tested the ability of the HAP-multitag probe to diagnose atherosclerosis by *in vivo* imaging by first using PET/CT. HAP-multitag was intravenously injected in group B ApoE$^{-/-}$ mice, and images recorded 90 min post injection. Spots of nanotracer uptake are observed in the aortic arch and the aorta (Figures 6a and S2). PET/CT images were also obtained in group D ApoE$^{-/-}$ mice for comparison. Contrary to what we see in young mice, these mice showed negligible uptake in the specific ROIs (Figure 6b), agreeing with the biodistribution results we have previously shown. Compared to [^{18}F]FNa and other BP-based tracers, bone uptake of HAP-multitag is negligible (Figures 6a and S2). Uptake of HAP-multitag was also compared with the use of ^{68}Ga-IONP-citrate as a nanotracer control. Figure 6b shows the percentage of injected dose per gram of tissue when using HAP-multitag or ^{68}Ga-IONP-citrate in groups B and C ApoE$^{-/-}$ mice (those groups with the highest uptake of the nanotracer). As expected, ^{68}Ga-IONP-citrate does not accumulate in groups B and D ApoE$^{-/-}$ mice since they lack the microcalcification targeting capabilities.

Nanotracer uptake was also confirmed by *ex vivo* PET imaging of excised aortas after *in vivo* experiments. Signaling spots are clearly identified throughout the aorta, predominantly in the aortic arch and the renal bifurcation (Figure 6c). To confirm whether the uptake is related to vascular calcifications, *ex vivo* fluorescence images were obtained using OsteoSense. This is a commercial dye, showing fluorescence in the near-infrared region, which includes a bisphosphonate moiety and is the gold standard for *ex vivo* microcalcification detection by fluorescence techniques.[32,33] Following the manufacturer instructions, *ex vivo* fluorescence imaging was conducted 24 h post intravenous injection of OsteoSense in group B ApoE$^{-/-}$ mice (n = 5, Figure S3). Comparing the *ex vivo* PET signal (Figure 6c) with the fluorescence signal from OsteoSense (Figure 6d), there is a perfect match between the different spots showing uptake of the probes, confirming the presence of microcalcifications in the sites where there is a clear uptake of HAP-multitag. The uptake of HAP-multitag in the aorta and its colocalization with microcalcification areas are further studied by histology. First, we compared the accumulation in aorta samples between groups B and D ApoE$^{-/-}$ mice (Figures 6e and S4). While iron is clearly present in group B, as blue spots due to Perls' Prussian Blue staining, there are no spots in group D. Then, we analyzed the colocalization between iron deposits in group B and microcalcifications to confirm the driving force for the uptake of the

https://doi.org/10.1021/acsami.1c13417
ACS Appl. Mater. Interfaces 2021, 13, 45279–45290

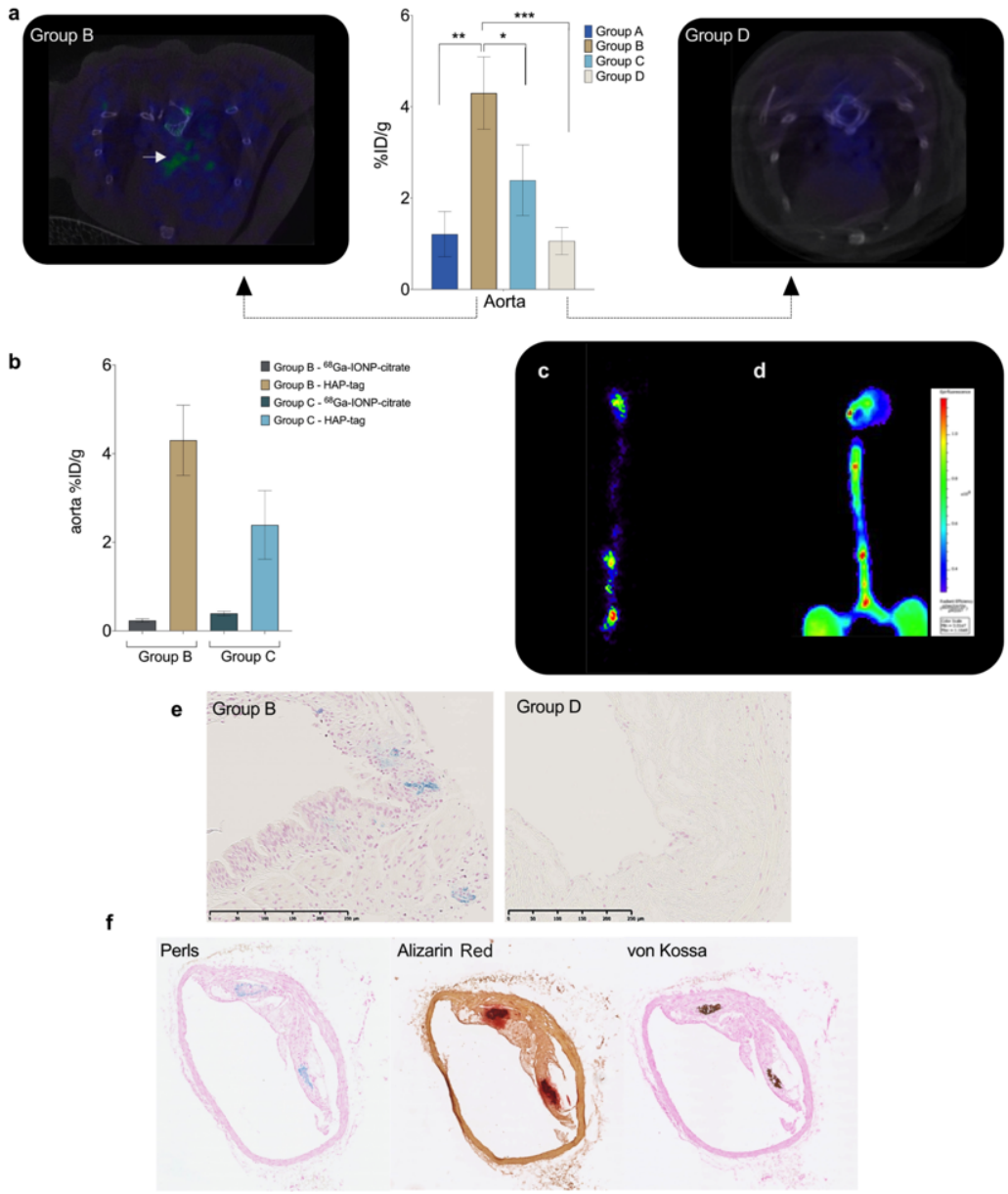

Figure 6. (a) Aorta uptake of HAP-multitag (the graph corresponds to Figure 5b, included here to compare uptake with images) and PET/CT images of group B and group D ApoE$^{-/-}$ mice 90 min post i.v. injection with HAP-multitag; (b) uptake of nanotracers, expressed as the percentage injected dose per gram (%ID/g), in ApoE$^{-/-}$ mice (N = 5) of groups B and C using ^{68}Ga-IONP-citrate or HAP-multitag; error bars indicate s.d., N = 5. (c) *Ex vivo* PET imaging of a group B ApoE$^{-/-}$ mouse aorta 90 min post i.v. injection with HAP-multitag; (d) *ex vivo* fluorescence imaging of a group B ApoE$^{-/-}$ mouse aorta 24 h post i.v. injection of OsteoSense 680EX; (e) Perls' Prussian Blue staining of aorta sections from group B and group D ApoE$^{-/-}$ mice, both injected with HAP-multitag (scale bar is 250 μm). (f) Histology of the Group B ApoE$^{-/-}$ mice aortas stained with Perls' Prussian Blue, Alizarin Red, and von Kossa.

nanotracer. Figure 6f shows the results of triple stained aortas from a group B ApoE$^{-/-}$ mouse. We detected iron accumulation with Perls and microcalcifications with Alizarin Red and von Kossa. The colocalization between iron deposits and microcalcifications is clearly visible (more images in Figure S5), confirming the mechanism of accumulation for HAP-multitag.

Magnetic Resonance Imaging. Finally, the HAP-multitag performance, as a positive contrast tracer in MRI, was evaluated. As extensively revised, nanoparticles with r_2/r_1 ratios below 4 have a high capability to provide positive MRI contrast.[17,19] Therefore, the low ratio for HAP-multitag (Figure 3a) ensures its performance as a positive imaging probe in MRI. However, even with low ratios, the *in vivo* performance in large magnetic fields and with the accumulation in a particular tissue is more challenging.

In vivo imaging using non-functionalized ^{68}Ga-IONP-citrate was conducted in group A, group B, and group D ApoE$^{-/-}$ mice with no significant contrast enhancement observed in the aortic arch of these groups (Figures 7d–f and S6). Then, MRI was carried out using HAP-multitag as the nanotracer. In the case of group A and group D ApoE$^{-/-}$ mice, some brightening

https://doi.org/10.1021/acsami.1c13417
ACS Appl. Mater. Interfaces 2021, 13, 45279–45290

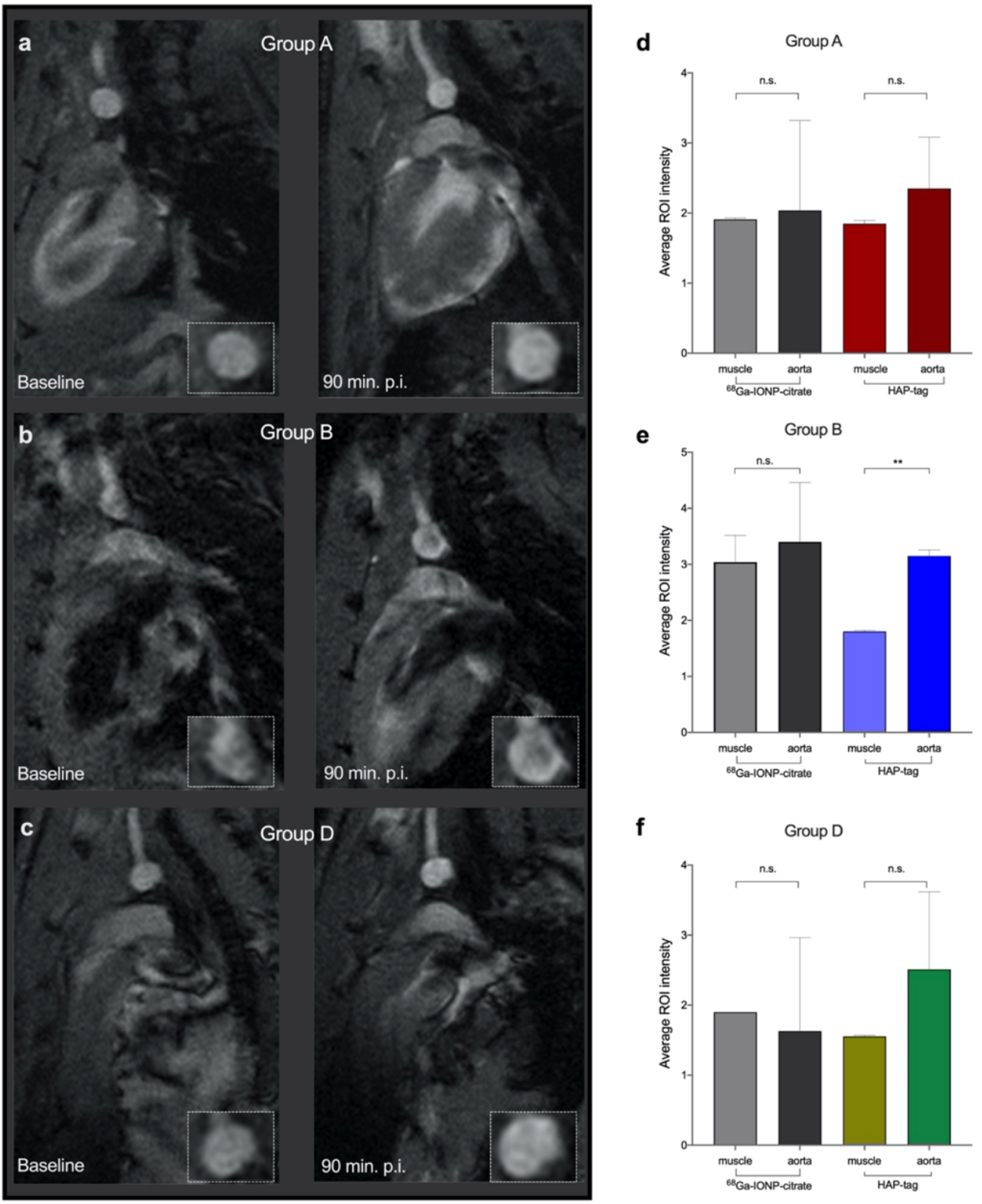

Figure 7. T_1-weighted MRI before (baseline) and 90 min after i.v. injection of HAP-multitag for (a) group A ApoE$^{-/-}$, (b) group B ApoE$^{-/-}$, and (c) group D ApoE$^{-/-}$; average ROI intensity (n = 10 per mouse) in the muscle and aorta 90 min after i.v. injection of ^{68}Ga-IONP-citrate or HAP-multitag in ApoE$^{-/-}$ mice (n = 3) for (d) group A ApoE$^{-/-}$, (e) group B ApoE$^{-/-}$, and (f) group D ApoE$^{-/-}$. *P < 0.05, **P < 0.01, ***P < 0.001, one-way ANOVA; error bars indicate s.d.

https://doi.org/10.1021/acsami.1c13417
ACS Appl. Mater. Interfaces 2021, 13, 45279−45290

of the arterial wall is visible; however, no significant contrast was observed (Figure 7a,c). On the contrary, the positive contrast was unambiguously appreciated 90 min after i.v. injection of HAP-multitag in the group B ApoE$^{-/-}$ mice (Figures 7b and S7).

Semi-quantitative analysis of the images confirmed these results. For this, 10 different ROIs were selected in the muscle (used as reference) and the aorta in 3 different animals per group. No significant differences were obtained using ^{68}Ga-IONP-citrate in all animals and HAP-multitag for group A and group D ApoE$^{-/-}$ mice (Figure 7d–f). In agreement with the *in vivo* imaging results, significant intensity differences were found for group B ApoE$^{-/-}$ mice. These results show the ability of HAP-multitag to generate positive contrast in MRI in a manner relevant to the calcification stage of the aorta.

■ CONCLUSIONS

The development of PET/MRI as a powerful molecular imaging technique requires the development of imaging probes capable of providing simultaneous signals in both modalities. In this sense, IONPs are the perfect candidate due to their tailored synthesis, biofunctionalization, and biocompatibility. They are perfect for the purpose, with the exception of one key aspect, that is, the typical negative contrast they provide. Here, we show that it is possible to combine the PET signal and positive contrast using IONPs. The *in vitro* affinity of HAP-multitag for calcium salts translates into an *in vivo* uptake that depends on mice age and therefore in the calcification stage. We show how the targeted accumulation of these nanoparticles translates into easily identifiable PET and—bright signal—MRI beyond the magnetic resonance angiography typically performed with other IONPs. Using our nanotracer, HAP-multitag, it is possible to perform an early characterization of atherosclerotic plaques in ApoE$^{-/-}$ mice just 16 weeks old. Its uptake enables the longitudinal characterization of micro-calcifications.

■ EXPERIMENTAL SECTION

^{68}Ga ($t_{1/2}$ = 68 min, β+ = 89%, and EC = 11%) was obtained from a ^{68}Ge/^{68}Ga generator system (ITG Isotope Technologies Garching GmbH, Germany) in which ^{68}Ge ($t_{1/2}$ = 270 d) was attached to a column based on an organic matrix generator. ^{68}Ga was eluted with 4 mL of 0.05 M hydrochloric acid. Iron(III) chloride, hydrazine monohydrate, *N*-(3-dimethylaminopropyl)-*N*′-ethylcarbodiimide hydrochloride, *N*-hydroxysulfosuccinimide sodium salt, and alendronate sodium salt were purchased from Sigma-Aldrich. Citric acid trisodium salt dihydrate was purchased from Acros organics. OsteoSense 680TM EX was purchased from PerkinElmer, and disposable PD-10 desalting salt columns were purchased from GE Healthcare Life Sciences and Amicon Ultra centrifugal filters from Merck Millipore.

Synthesis of ^{68}Ga-IONP-Citrate. $FeCl_3 \times 6\ H_2O$ (75 mg, 0.28 mmol), sodium citrate hydrate (80 mg, 0.27 mmol), and 1280 MBq of $^{68}GaCl_3$ in HCl (0.05 M, 4 mL) were dissolved in water (5 mL) in a microwave-adapted flask, followed by addition of 1 mL of hydrazine hydrate. The solution was ramped to 120 °C over 54 s and held at this temperature for 10 min (240 W) in a Monowave 300 microwave reactor equipped with an internal temperature probe and an external IR probe (Anton Paar, GmbH, Ostfildern-Scharnhausen, Germany). The reaction mixture was then cooled to 60 °C, and the ^{68}Ga-IONP-citrate product was purified by passing the mixture through a PD-10 column to eliminate excess small reagents, including all unincorporated radioisotopes. This purification process provided 9 mL of ^{68}Ga-IONP-citrate with a total activity of 781 MBq (measured 40 min after starting the reaction), with a radiolabeling yield of 92%.

Synthesis of ^{68}Ga-IONP-Alendronate (HAP-Multitag). To 750 MBq of ^{68}Ga-IONP-citrate (5 mL) were added 0.07 mmol of EDC and 0.075 mmol of *N*-hydroxysulfosuccinimide sodium salt (sulfo-NHS). The solution was stirred for 30 min at room temperature (r.t.) and then ultracentrifuged at 10,350*g* through Amicon Ultra-15 30 kDa centrifugal filters for 4 min to remove excess reagents. The retentate was resuspended in 1.5 mL of N-(2-hydroxyethyl)piperazine-N′-ethanesulfonic acid (HEPES) buffer, pH 8, and 1 mg of alendronate sodium salt was added to the solution. The mixture was maintained at r.t for 60 min with stirring. Finally, another ultrafiltration step was performed to eliminate unreacted alendronate. The retentate was resuspended in saline solution, giving 195.6 MBq of HAP-multitag with a radiolabeling yield of 98%.

Physicochemical Characterization. The hydrodynamic size and polydispersity index were measured with a Zetasizer Nano ZS90 system (Malvern Instruments, UK) using folded capillary cells with samples in water unless other solvents are indicated. For determination of the morphology and mean particle size and distribution, samples were examined under a transmission electron microscope (Tecnai F30, FEI) operated at 300 kV using scanning-transmission imaging with a high-angle annular dark-field detector (STEM-HAADF). Chemical analysis of the nanoparticles was performed by EDX. A drop of the nanoparticle suspension was deposited onto a holey-carbon-coated copper grid and left to evaporate at r.t. Mean sizes and standard deviations were calculated for approximately 50 particles.

Sample Preparation for Electron Microscopy. ^{68}Ga-IONP-citrate and ^{68}Ga-IONP-alendronate (cold samples, without the active ^{68}Ga isotope) were incubated with 20 μM HAP. After 30 min of incubation at r.t., a drop of the nanoparticle suspension was deposited onto a holey-carbon-coated copper grid and left to evaporate at r.t.

Titration of the Ca^{2+} Salts. ^{68}Ga-IONP-citrate and ^{68}Ga-IONP-alendronate (cold samples, without the active ^{68}Ga isotope) were incubated with different concentrations (0.2, 0.4, 1, 2, 4, 10, 20 μM) of three different calcium salts: HAP, calcium oxalate monohydrate, and β-tricalcium phosphate. After 60 min of incubation at r.t., the hydrodynamic size of the samples was measured using a Zetasizer Nano ZS90 system (Malvern Instruments, UK).

Binding Quantification by Fluorescence. The Alexa Fluor 647 (A647) dye (excitation λ = 649 nm; emission λ = 666 nm) was used to quantify the binding (%) of ^{68}Ga-IONP-citrate and ^{68}Ga-IONP-alendronate (cold samples, without the active ^{68}Ga isotope) to different calcium salts: HAP, calcium oxalate monohydrate, and β-tricalcium phosphate. To synthesize ^{68}Ga-IONP-citrate-A647 and ^{68}Ga-IONP-alendronate-A647, 5 mL of ^{68}Ga-IONP-citrate was added to 0.07 mmol EDC and 0.075 mmol of *N*-hydroxysulfosuccinimide sodium salt (sulfo-NHS). The solution was stirred for 30 min at r.t. and then ultracentrifuged at 10,350*g* through Amicon Ultra-15 30 kDa centrifugal filters for 4 min to remove excess reagents. The retentate was resuspended in 1.5 mL of HEPES buffer, pH 8, and 100 μg of Alexa 647 hydrazide to synthesize ^{68}Ga-IONP-citrate-A647, and 100 μg of Alexa 647 hydrazide plus 1 mg of alendronate sodium salt to obtain ^{68}Ga-IONP-alendronate-A647. The samples were maintained at r.t. for 60 min under vigorous stirring. Once this step was finished, samples were purified by ultrafiltration to eliminate unreacted A647 and alendronate. The retentate was resuspended in saline solution.

^{68}Ga-IONP-citrate-A647 and ^{68}Ga-IONP-alendronate-A647 were incubated for 60 min at r.t. with different concentrations of the calcium salts (0.2, 0.4, 1, 2, 4, 10, 20 μM). Posteriorly, supernatant fluorescence was measured at λ = 666 nm after 150 min centrifugation at 13,680*g*.

The degree of Ca salt binding was assessed using the following formula:

$$\text{binding}(\%) = \frac{(X - Y)\cdot 100}{X} \quad (1)$$

where X is the initial amount of fluorescence in ^{68}Ga-IONP-citrate-A647 and ^{68}Ga-IONP-alendronate-A647 and Y is the amount of fluorescence left in the supernatant after centrifugation.

https://doi.org/10.1021/acsami.1c13417
ACS Appl. Mater. Interfaces 2021, 13, 45279−45290

Relaxometry. Relaxometric properties of the samples were assessed by measuring longitudinal and transverse relaxation times. Four concentrations of each nanoparticle sample were selected, and the longitudinal and transversal relaxation times of each one were measured using a Bruker mq60 at 1.5 T and 37 °C. The r_1 and r_2 values were plotted against the Fe concentration (0, 0.25, 0.5, 1, and 2 mM).

^{68}Ga-IONP-citrate and ^{68}Ga-IONP-alendronate (cold samples, without the active ^{68}Ga isotope) were incubated with different concentrations (0.2, 0.4, 1, 2, 4, 10, 20 μM) of three different calcium salts: HAP, calcium oxalate monohydrate, and β-tricalcium phosphate, as well as magnesium and zinc chloride. After 60 min of incubation at r.t., r_1 and r_2 values were measured to calculate the r_2/r_1 ratio.

Animal Model. Mice were housed in the specific pathogen-free facilities at the Centro Nacional de Investigaciones Cardiovasculares Carlos III, Madrid. All animal experiments conformed to EU Directive 2010/63EU and Recommendation 2007/526/EC, enforced in Spanish law under Real Decreto 53/2013. The protocol was approved by the Madrid regional government (PROEX16/277).

ApoE$^{-/-}$ mice were fed with high-cholesterol diet (Western diet) from 8 weeks old onward to obtain the atherosclerosis mouse model.

PET/CT Imaging. *In vivo* PET/CT imaging in mice was performed with a nanoPET/CT small-animal imaging system (Mediso Medical Imaging Systems, Budapest, Hungary). List-mode PET data acquisition commenced 90 min after injection of a bolus of 10−15 MBq of HAP-multitag through the tail vein and continued for 30 min. At the end of PET, a micro-CT was performed for attenuation correction and anatomic reference. The dynamic PET images were reconstructed in a 105 × 105 matrix (frame rates: 3 × 10 min, 1 × 30 min, 1 × 60 min) using a Tera-Tomo 3D iterative algorithm. Images were obtained and reconstructed with proprietary Nucline software (Mediso, Budapest, Hungary). Images were analyzed using Horos software v.3.3.6.

Fluorescence Imaging. Experiments were conducted following the standard protocol provided by the manufacturer. OsteoSense 680EX was reconstituted by addition of 1.2 mL of phosphate-buffered saline (PBS) 1× into the vial. The mixture was gently shaken for 5 min at r.t. Then, 100 μL of the resultant solution was intravenously injected into 5 ApoE$^{-/-}$ mice. 24 h post injection, animals were sacrificed in a CO_2 chamber and perfused with 8 mL of PBS 1×, and the aortas were excised. *Ex vivo* imaging of the aortas was carried out in an IVIS Imaging System 200, Xenogen (acquisition parameters: Cy5.5 ex/em filter, high level, BIN-HR, FOV 13.3, f2, 4s).

MRI Acquisition. All experiments were performed on a 7 T Bruker Biospec 70/30 USR MRI system (Bruker Biospin GmbH, Ettlingen, Germany), interfaced to an AVANCE III console. Anesthesia was induced with 3% isoflurane in 30% oxygen and maintained 1−2% isoflurane along the experiment.

A BGA12 imaging gradient (maximum gradient strength 400 mT/m) system with a 40 mm diameter quadrature volume resonator was used for MRI data acquisition. Animals were positioned in a customized 3D printed bed with a head holder and kept warmed with heated air pumped through an MRI compatible system interfaced to a Monitoring and Gating Model 1025 (SA instruments). Temperature control (anal) and respiration (through a respiratory pad) were registered along the experiment.

To ensure an accurate positioning, pure axial and four-chamber view scout images were used to set up the representative aortic arch view. From these, images were obtained between the brachiocephalic artery and left common carotid artery, perpendicular to the direction of the flow in the aorta. A single 0.8 mm, 2.8 × 2.8 cm isotropic FOV (obtained and reconstructed with 256 × 256) slice was obtained using a Bruker self-gated cine gradient echo FLASH sequence using the following parameters: minimum TE 4 ms, TR 9 ms, flip angle 10°, 1 average. An additional image in the same position was obtained with a fat suppression module.

***Ex Vivo* Biodistribution.** Biodistribution was studied with a Wizard 1470 gamma counter (PerkinElmer). Animals were sacrificed in a CO_2 chamber, after which blood was extracted and the animals perfused with 8 mL of PBS 1×. Organs were extracted and counted in the gamma counter for 1 min each. Readings were decay-corrected and presented as the percentage of injected dose per gram (%ID/g).

Histological Analysis. Excised aortas were fixed in 10% formalin for 24 h. The tissue was dehydrated and embedded in paraffin until sectioning. Aorta sections were stained with Perl's Prussian Blue, von Kossa, and Alizarin red. Images were processed and digitalized with NIS-Elements acquisition software.

■ ASSOCIATED CONTENT

Supporting Information

The Supporting Information is available free of charge at https://pubs.acs.org/doi/10.1021/acsami.1c13417.

Additional STEM-HAADF, PET/CT, fluorescence, and MRI images (PDF)

■ AUTHOR INFORMATION

Corresponding Author

Fernando Herranz − *CIBER de Enfermedades Respiratorias (CIBERES), 28029 Madrid, Spain; NanoMedMol Group, Instituto de Química Medica (IQM), Consejo Superior de Investigaciones Científicas (CSIC), 28006 Madrid, Spain;* orcid.org/0000-0002-3743-0050; Email: fherranz@iqm.csic.es

Authors

Juan Pellico − *CIBER de Enfermedades Respiratorias (CIBERES), 28029 Madrid, Spain; School of Biomedical Engineering & Imaging Sciences, King's College London, SE1 7EH London, U.K.;* orcid.org/0000-0003-2787-8641

Irene Fernández-Barahona − *Facultad de Farmacia, Universidad Complutense de Madrid, 28040 Madrid, Spain; NanoMedMol Group, Instituto de Química Medica (IQM), Consejo Superior de Investigaciones Científicas (CSIC), 28006 Madrid, Spain*

Jesús Ruiz-Cabello − *CIBER de Enfermedades Respiratorias (CIBERES), 28029 Madrid, Spain; Facultad de Farmacia, Universidad Complutense de Madrid, 28040 Madrid, Spain; Center for Cooperative Research in Biomaterials (CIC biomaGUNE), Basque Research and Technology Alliance (BRTA), 20014 Donostia San Sebastián, Spain; IKERBASQUE, Basque Foundation for Science, 48013 Bilbao, Spain;* orcid.org/0000-0001-8681-5056

Lucía Gutiérrez − *Departamento de Química Analítica, Instituto de Nanociencia y Materiales de Aragón, Universidad de Zaragoza-CSIC y CIBER-BBN, 50018 Zaragoza, Spain;* orcid.org/0000-0003-2366-3598

María Muñoz-Hernando − *NanoMedMol Group, Instituto de Química Medica (IQM), Consejo Superior de Investigaciones Científicas (CSIC), 28006 Madrid, Spain; Centro Nacional de Investigaciones Cardiovasculares Carlos III (CNIC), 28029 Madrid, Spain*

María J. Sánchez-Guisado − *Center for Cooperative Research in Biomaterials (CIC biomaGUNE), Basque Research and Technology Alliance (BRTA), 20014 Donostia San Sebastián, Spain*

Irati Aiestaran-Zelaia − *Center for Cooperative Research in Biomaterials (CIC biomaGUNE), Basque Research and Technology Alliance (BRTA), 20014 Donostia San Sebastián, Spain*

Lydia Martínez-Parra − *Center for Cooperative Research in Biomaterials (CIC biomaGUNE), Basque Research and Technology Alliance (BRTA), 20014 Donostia San Sebastián, Spain*

Ignacio Rodríguez − *CIBER de Enfermedades Respiratorias (CIBERES), 28029 Madrid, Spain; Facultad de Farmacia, Universidad Complutense de Madrid, 28040 Madrid, Spain*
Jacob Bentzon − *Centro Nacional de Investigaciones Cardiovasculares Carlos III (CNIC), 28029 Madrid, Spain*

Complete contact information is available at: https://pubs.acs.org/10.1021/acsami.1c13417

Author Contributions

[O]J.P. and I.F.-B. contributed equally. The manuscript was written through contributions of all authors. All authors have given approval to the final version of the manuscript.

Funding

This work was supported by the Spanish Ministry of Science (grant nos. SAF2016-79593-P, RED2018-102469-T, and PID2019-104059RB-I00) and from the Gobierno Vasco, Dpto. Industria, Innovación, Comercio y Turismo under the ELKARTEK Program (grant no. KK-2019/bmG19). JR-C received funding from the BBVA Foundation (Ayudas a Equipos de investigación científica Biomedicina 2018). The CNIC is supported by the MICINN and the Pro-CNIC Foundation and is a Severo Ochoa Center of Excellence (MICINN award SEV-2015-0505). CIC biomaGUNE is supported by the Maria de Maeztu Units of Excellence Program from the Spanish State Research Agency—grant no. MDM-2017-0720. L.G. acknowledges financial support from the Ramón y Cajal program (RYC-2014-15512 0).

Notes

The authors declare no competing financial interest.

■ ACKNOWLEDGMENTS

The authors would like to acknowledge the use of the Advanced Microscopy Laboratory (LMA) for access to their instrumentation and expertise. The authors acknowledge support of the publication fee by the CSIC Open Access Publication Support Initiative through its Unit of Information Resources for Research (URICI).

■ ABBREVIATIONS

PET, positron emission tomography
MRI, magnetic resonance imaging
HAP, hydroxyapatite
BP, bisphosphonate
CY, computed tomography
IONPs, iron oxide nanoparticles
EDC, *N*-(3-dimethylaminopropyl)-*N*′-ethylcarbodiimide hydrochloride
NHS, *N*-hydroxysuccinimide
DLS, dynamic light scattering
FTIR, Fourier transform infrared
STEM-HAADF, scanning transmission electron microscopy high-angle annular dark-field imaging

■ REFERENCES

(1) Barrett, H. E.; Van der Heiden, K.; Farrell, E.; Gijsen, F. J. H.; Akyildiz, A. C. Calcifications in Atherosclerotic Plaques and Impact on Plaque Biomechanics. *J. Biomech.* **2019**, *87*, 1−12.
(2) Albanese, I.; Khan, K.; Barratt, B.; Al-Kindi, H.; Schwertani, A. Atherosclerotic Calcification: Wnt Is the Hint. *J. Am. Heart Assoc.* **2018**, *7*, No. e007356.
(3) Nishizawa, Y.; Higuchi, C.; Nakaoka, T.; Omori, H.; Ogawa, T.; Sakura, H.; Nitta, K. Compositional Analysis of Coronary Artery Calcification in Dialysis Patients in Vivo by Dual-Energy Computed Tomography Angiography. *Ther. Apher. Dial.* **2018**, *22*, 365−370.
(4) Tzolos, E.; Dweck, M. R. 18 F-Sodium Fluoride (18 F-NaF) for Imaging Microcalcification Activity in the Cardiovascular System. *Arterioscler. Thromb. Vasc. Biol.* **2020**, *40*, 1620−1626.
(5) Keeling, G. P.; Sherin, B.; Kim, J.; San Juan, B.; Grus, T.; Eykyn, T. R.; Rösch, F.; Smith, G. E.; Blower, P. J.; Terry, S. Y. A. [68 Ga]Ga-THP-Pam: A Bisphosphonate PET Tracer with Facile Radiolabeling and Broad Calcium Mineral Affinity. *Bioconjugate Chem.* **2021**, *32*, 1276.
(6) Pellico, J.; Lechuga-Vieco, A. V.; Benito, M.; García-Segura, J. M.; Fuster, V.; Ruiz-Cabello, J.; Herranz, F. Microwave-Driven Synthesis of Bisphosphonate Nanoparticles Allows in Vivo Visualisation of Atherosclerotic Plaque. *RSC Adv.* **2015**, *5*, 1661−1665.
(7) Mastrogiacomo, S.; Kownacka, A. E.; Dou, W.; Burke, B. P.; Rosales, R. T. M.; Heerschap, A.; Jansen, J. A.; Archibald, S. J.; Walboomers, X. F. Bisphosphonate Functionalized Gadolinium Oxide Nanoparticles Allow Long-Term MRI/CT Multimodal Imaging of Calcium Phosphate Bone Cement. *Adv. Healthcare Mater.* **2018**, *7*, 1800202.
(8) Bordoloi, J. K.; Berry, D.; Khan, I. U.; Sunassee, K.; de Rosales, R. T. M.; Shanahan, C.; Blower, P. J. Technetium-99m and Rhenium-188 Complexes with One and Two Pendant Bisphosphonate Groups for Imaging Arterial Calcification. *Dalton Trans.* **2015**, *44*, 4963−4975.
(9) Czernin, J.; Satyamurthy, N.; Schiepers, C. Molecular Mechanisms of Bone 18F-NaF Deposition. *J. Nucl. Med.* **2010**, *51*, 1826−1829.
(10) Felix, D. D.; Gore, J. C.; Yankeelov, T. E.; Peterson, T. E.; Barnes, S.; Whisenant, J.; Weis, J.; Shoukouhi, S.; Virostko, J.; Nickels, M.; McIntyre, J. O.; Sanders, M.; Abramson, V.; Tantawy, M. N. Detection of Breast Cancer Microcalcification Using (99m)Tc-MDP SPECT or Osteosense 750EX FMT Imaging. *Nucl. Med. Biol.* **2015**, *42*, 269−273.
(11) Ordonez, A. A.; DeMarco, V. P.; Klunk, M. H.; Pokkali, S.; Jain, S. K. Imaging Chronic Tuberculous Lesions Using Sodium [(18)F]-Fluoride Positron Emission Tomography in Mice. *Mol. Imag. Biol.* **2015**, *17*, 609−614.
(12) Wilson, G. H., 3rd; Gore, J. C.; Yankeelov, T. E.; Barnes, S.; Peterson, T. E.; True, J. M.; Shokouhi, S.; McIntyre, J. O.; Sanders, M.; Abramson, V.; Ngyuen, T.-Q.; Mahadevan-Jansen, A.; Tantawy, M. N. An Approach to Breast Cancer Diagnosis via PET Imaging of Microcalcifications Using (18)F-NaF. *J. Nucl. Med.* **2014**, *55*, 1138−1143.
(13) Ehman, E. C.; Johnson, G. B.; Villanueva-Meyer, J. E.; Cha, S.; Leynes, A. P.; Larson, P. E. Z.; Hope, T. A. PET/MRI: Where Might It Replace PET/CT? *J. Magn. Reson. Imag.* **2017**, *46*, 1247−1262.
(14) Judenhofer, M. S.; Wehrl, H. F.; Newport, D. F.; Catana, C.; Siegel, S. B.; Becker, M.; Thielscher, A.; Kneilling, M.; Lichy, M. P.; Eichner, M.; Klingel, K.; Reischl, G.; Widmaier, S.; Röcken, M.; Nutt, R. E.; Machulla, H.-J.; Uludag, K.; Cherry, S. R.; Claussen, C. D.; Pichler, B. J. Simultaneous PET-MRI: A New Approach for Functional and Morphological Imaging. *Nat. Med.* **2008**, *14*, 459−465.
(15) Robson, P. M.; Dweck, M. R.; Trivieri, M. G.; Abgral, R.; Karakatsanis, N. A.; Contreras, J.; Gidwani, U.; Narula, J. P.; Fuster, V.; Kovacic, J. C.; Fayad, Z. A. Coronary Artery PET/MR Imaging. *JACC Cardiovasc. Imaging* **2017**, *10*, 1103−1112.
(16) Dadfar, S. M.; Roemhild, K.; Drude, N. I.; von Stillfried, S.; Knüchel, R.; Kiessling, F.; Lammers, T. Iron Oxide Nanoparticles: Diagnostic, Therapeutic and Theranostic Applications. *Adv. Drug Deliv. Rev.* **2019**, *138*, 302−325.
(17) Kim, B. H.; Lee, N.; Kim, H.; An, K.; Park, Y. I.; Choi, Y.; Shin, K.; Lee, Y.; Kwon, S. G.; Na, H. B.; Park, J.-G.; Ahn, T.-Y.; Kim, Y.-W.; Moon, W. K.; Choi, S. H.; Hyeon, T. Large-Scale Synthesis of Uniform and Extremely Small-Sized Iron Oxide Nanoparticles for High-Resolution T 1 Magnetic Resonance Imaging Contrast Agents. *J. Am. Chem. Soc.* **2011**, *133*, 12624−12631.

(18) Tromsdorf, U. I.; Bruns, O. T.; Salmen, S. C.; Beisiegel, U.; Weller, H. A Highly Effective, Nontoxic T 1 MR Contrast Agent Based on Ultrasmall PEGylated Iron Oxide Nanoparticles. *Nano Lett.* **2009**, *9*, 4434−4440.
(19) Pellico, J.; Ruiz-Cabello, J.; Fernández-Barahona, I.; Gutiérrez, L.; Enríquez, J. A.; Morales, M. P.; Herranz, F.; Enríquez, J. A. J. A.; Morales, M. P. P.; Herranz, F. One-Step Fast Synthesis of Nanoparticles for MRI: Coating Chemistry as the Key Variable Determining Positive or Negative Contrast. *Langmuir* **2017**, *33*, 10239−10247.
(20) Fernández-Barahona, I.; Gutiérrez, L.; Veintemillas-Verdaguer, S.; Pellico, J.; Morales, M. d. P.; Catala, M.; del Pozo, M. A.; Ruiz-Cabello, J.; Herranz, F. Cu-Doped Extremely Small Iron Oxide Nanoparticles with Large Longitudinal Relaxivity: One-Pot Synthesis and in Vivo Targeted Molecular Imaging. *ACS Omega* **2019**, *4*, 2719−2727.
(21) Pellico, J.; Ruiz-Cabello, J.; Saiz-Alía, M.; del Rosario, G.; Caja, S.; Montoya, M.; Fernández de Manuel, L.; Morales, M. P.; Gutiérrez, L.; Galiana, B.; Enríquez, J. A.; Herranz, F.; Saiz-Al'ia, M.; del Rosario, G.; Caja, S.; Montoya, M. M.; Fernández de Manuel, L.; Morales, M. P.; Gutiérrez, L.; Galiana, B.; Enr'iquez, J. A.; Herranz, F. Fast Synthesis and Bioconjugation of 68Ga Core-Doped Extremely Small Iron Oxide Nanoparticles for PET/MR Imaging. *Contrast Media Mol. Imaging* **2016**, *11*, 203−210.
(22) Pellico, J.; Lechuga-Vieco, A. V.; Almarza, E.; Hidalgo, A.; Mesa-Nuñez, C.; Fernández-Barahona, I.; Quintana, J. A.; Bueren, J.; Enríquez, J. A.; Ruiz-Cabello, J.; Herranz, F. In Vivo Imaging of Lung Inflammation with Neutrophil-Specific 68Ga Nano-Radiotracer. *Sci. Rep.* **2017**, *7*, 13242.
(23) Teixeira, S.; Santos, M. M.; Fernandes, M. H.; Costa-Rodrigues, J.; Branco, L. C. Alendronic Acid as Ionic Liquid: New Perspective on Osteosarcoma. *Pharmaceutics* **2020**, *12*, 293.
(24) Groult, H.; Ruiz-Cabello, J.; Pellico, J.; Lechuga-Vieco, A. V.; Bhavesh, R.; Zamai, M.; Almarza, E.; Martín-Padura, I.; Cantelar, E.; Martínez-Alcázar, M. P.; Herranz, F. Parallel Multifunctionalization of Nanoparticles: A One-Step Modular Approach for in Vivo Imaging. *Bioconjugate Chem.* **2015**, *26*, 153−160.
(25) Salinas, B.; Ruiz-Cabello, J.; Lechuga-Vieco, A. V.; Benito, M.; Herranz, F.; Ruiz-Cabello, J.; Lechuga-Vieco, A. V.; Benito, M.; Herranz, F. Surface-Functionalized Nanoparticles by Olefin Metathesis: A Chemoselective Approach for In Vivo Characterization of Atherosclerosis Plaque. *Chem.—Eur. J.* **2015**, *21*, 10450−10456.
(26) Nakashima, Y.; Plump, A. S.; Raines, E. W.; Breslow, J. L.; Ross, R. ApoE-Deficient Mice Develop Lesions of All Phases of Atherosclerosis throughout the Arterial Tree. *Arterioscler. Thromb.* **1994**, *14*, 133−140.
(27) Emini Veseli, B.; Perrotta, P.; De Meyer, G. R. A.; Roth, L.; Van der Donckt, C.; Martinet, W.; De Meyer, G. R. Y. Animal Models of Atherosclerosis. *Eur. J. Pharmacol.* **2017**, *816*, 3−13.
(28) Feng, Q.; Liu, Y.; Huang, J.; Chen, K.; Huang, J.; Xiao, K. Uptake, Distribution, Clearance, and Toxicity of Iron Oxide Nanoparticles with Different Sizes and Coatings. *Sci. Rep.* **2018**, *8*, 2082.
(29) Fiz, F.; Morbelli, S.; Piccardo, A.; Bauckneht, M.; Ferrarazzo, G.; Pestarino, E.; Cabria, M.; Democrito, A.; Riondato, M.; Villavecchia, G.; Marini, C.; Sambuceti, G. (1)(8)F-NaF Uptake by Atherosclerotic Plaque on PET/CT Imaging: Inverse Correlation Between Calcification Density and Mineral Metabolic Activity. *J. Nucl. Med.* **2015**, *56*, 1019−1023.
(30) Irkle, A.; Vesey, A. T.; Lewis, D. Y.; Skepper, J. N.; Bird, J. L. E.; Dweck, M. R.; Joshi, F. R.; Gallagher, F. A.; Warburton, E. A.; Bennett, M. R.; Brindle, K. M.; Newby, D. E.; Rudd, J. H.; Davenport, A. P. Identifying Active Vascular Microcalcification by 18F-Sodium Fluoride Positron Emission Tomography. *Nat. Commun.* **2015**, *6*, 7495.
(31) Hu, Y.; Hu, P.; Hu, B.; Chen, W.; Cheng, D.; Shi, H. Dynamic Monitoring of Active Calcification in Atherosclerosis by 18F−NaF PET Imaging. *Int. J. Cardiovasc. Imag.* **2021**, *37*, 731.
(32) O'Rourke, C.; Shelton, G.; Hutcheson, J. D.; Burke, M. F.; Martyn, T.; Thayer, T. E.; Shakartzi, H. R.; Buswell, M. D.; Tainsh, R. E.; Yu, B.; Bagchi, A.; Rhee, D. K.; Wu, C.; Derwall, M.; Buys, E. S.; Yu, P. B.; Bloch, K. D.; Aikawa, E.; Bloch, D. B.; Malhotra, R. Calcification of Vascular Smooth Muscle Cells and Imaging of Aortic Calcification and Inflammation. *J. Visualized Exp.* **2016**, No. e54017.
(33) Schurgers, L. J.; Akbulut, A. C.; Kaczor, D. M.; Halder, M.; Koenen, R. R.; Kramann, R. Initiation and Propagation of Vascular Calcification Is Regulated by a Concert of Platelet- and Smooth Muscle Cell-Derived Extracellular Vesicles. *Front. Cardiovasc. Med.* **2018**, *5*, 36.

https://doi.org/10.1021/acsami.1c13417
ACS Appl. Mater. Interfaces 2021, 13, 45279−45290

4. Conclusions

Article 1

In this paper, we have synthesised citrate-coated extremely small iron oxide nanoparticles with high T_1 or positive response in MRI. A single-step microwave-driven yields IONPs that are colloidally stable in different biological media in an extremely short reaction time (10 minutes). Their superparamagnetic behaviour with a fairly low saturation magnetisation value, together with the good r_1 value they present, preserving a low r_2/r_1 ratio make them ideal candidates for T_1-weighted MRI.

Taking advantage of the use of microwave technology, we have been able to intrinsically radiolabel iron oxide nanoparticles with ^{68}Ga, considerably reducing the reaction time with respect to traditional radiolabelling methods. This is a major advantage, especially when working with short half-lived isotopes as ^{68}Ga ($t_{1/2}$= 68 min). Radiolabelling yield obtained in our synthesis is almost threefold the one obtained by the pioneering study using a similar approach.[112] This represents a significant improvement, as in less than 20 minutes we have been able to obtain intrinsically ^{68}Ga-radiolabelled IONPs with an excellent radiolabelling yield and radiochemical purity. Hence, ^{68}Ga-IONP not only overcome the limitations offered by traditional IONPs used for T_2-MRI by offering positive contrast; but also provide signal in a functional imaging technique as is PET.

Article 2

In this paper, the use of copper as dopant metal is shown to enhance T_1 contrast MRI for the first time. It enhances the *in vivo* performance of iron oxide nanoparticles in targeted MRI, key for further development and translational purposes.

Doping nanoparticles with different amount of copper has yielded samples with different properties, after physicochemical, magnetic and relaxometric characterisation of the three samples, the *in vivo* performance as blood pool contrast agents was studied in mice. Revealing Cu4NP is an excellent candidate for T_1 MRI. Its performance as targeted contrast agent for MRI was tried and compared to undoped IONPs in a breast cancer allograft model, showing it improves T_1 signal in comparison to IONPs alone. Smaller amount of copper doping (Cu1.7NP) yields nanoparticles with suitable properties for MRI, but not as outstanding as the former. The sample with the highest amount of copper has no improved relaxometric properties for T_1 MRI.

Altogether, Cu4NP seems an excellent candidate for future clinical translation, not only by virtue of its excellent relaxometric properties and performance *in vivo* but also due to the type and rapidness of its synthesis.

Article 3

In this paper, we have developed a tool to longitudinally characterise microcalcifications in atherosclerotic plaque by PET and positive contrast MRI. HAP-multitag accumulation was found to be dependent on calcification progression, with a maximum uptake in the microcalcification stage. HAP-multitag, composed by our citrate-coated ^{68}Ga core-doped IONPs and a bisphosphonate moiety, is stable under physiological conditions and presents suitable pharmacokinetics for *in vivo* imaging. ^{68}Ga included in the IONP core with a high radiolabeling yield and high radiochemical purity and stability enables PET imaging. Furthermore, HAP-multitag presents ideal relaxometric values for positive MRI. The bisphosphonate moiety ensures affinity towards HAP and other calcium salts present in the plaque. We have proved how the accumulation of this bisphosphonate-based nanotracer translates into easily identifiable PET and bright signal in MRI, beyond the magnetic resonance angiography typically performed with other IONPs. Using HAP-multitag it is possible to perform an early characterisation of atherosclerotic plaques in ApoE$^{-/-}$ mice just 16 weeks old.

5. Bibliography

1. Weissleder, R. & Mahmood, U. Molecular Imaging. *Radiology* **219**, 316–333 (2001).
2. Chen, K. & Chen, X. Design and development of molecular imaging probes. *Curr. Top. Med. Chem.* **10**, 1227–36 (2010).
3. James, M. L. & Gambhir, S. S. A Molecular Imaging Primer: Modalities, Imaging Agents, and Applications. *Physiol. Rev.* **92**, 897–965 (2012).
4. Hansell, D. M. Thin-Section CT of the Lungs: The Hinterland of Normal. *Radiology* **256**, 695–711 (2010).
5. Evertsson, M. *et al.* Combined Magnetomotive ultrasound, PET/CT, and MR imaging of 68Ga-labelled superparamagnetic iron oxide nanoparticles in rat sentinel lymph nodes in vivo. *Sci. Rep.* **7**, 4824 (2017).
6. Pellico, J. *et al.* One-Step Fast Synthesis of Nanoparticles for MRI: Coating Chemistry as the Key Variable Determining Positive or Negative Contrast. *Langmuir* **33**, 10239–10247 (2017).
7. Zheng, B. *et al.* Quantitative Magnetic Particle Imaging Monitors the Transplantation, Biodistribution, and Clearance of Stem Cells In Vivo. *Theranostics* **6**, 291–301 (2016).
8. Zheng, M. *et al.* Self-Targeting Fluorescent Carbon Dots for Diagnosis of Brain Cancer Cells. *ACS Nano* **9**, 11455–11461 (2015).
9. Pellico, J. *et al.* Fast synthesis and bioconjugation of 68 Ga core-doped extremely small iron oxide nanoparticles for PET/MR imaging. *Contrast Media Mol. Imaging* **11**, 203–210 (2016).
10. Shukla, A. K. & Kumar, U. Positron emission tomography: An overview. *J. Med. Phys.* **31**, 13–21 (2006).
11. Garcia, E. V. Physical attributes, limitations, and future potential for PET and SPECT. *J. Nucl. Cardiol.* **19**, 19–29 (2012).
12. Fowler, A. M. & Cho, S. Y. PET Imaging for Breast Cancer. *Radiol. Clin. North Am.* **59**, 725–735 (2021).
13. Kratochwil, C. *et al.* 68 Ga-FAPI PET/CT: Tracer Uptake in 28 Different Kinds of Cancer. *J. Nucl. Med.* **60**, 801–805 (2019).
14. Paydary, K. *et al.* The Evolving Role of FDG-PET/CT in the Diagnosis, Staging, and Treatment of Breast Cancer. *Mol. Imaging Biol.* **21**, 1–10 (2019).
15. Chen, K., Miller, E. J. & Sadeghi, M. M. PET-Based Imaging of Ischemic Heart Disease. *PET Clin.* **14**, 211–221 (2019).

16. Tarkin, J. M., Ćorović, A., Wall, C., Gopalan, D. & Rudd, J. H. Positron emission tomography imaging in cardiovascular disease. *Heart* **106**, 1712–1718 (2020).

17. Saraste, A. & Knuuti, J. PET imaging in heart failure: the role of new tracers. *Heart Fail. Rev.* **22**, 501–511 (2017).

18. Chételat, G. *et al.* Amyloid-PET and 18F-FDG-PET in the diagnostic investigation of Alzheimer's disease and other dementias. *Lancet Neurol.* **19**, 951–962 (2020).

19. Cavaliere, C. *et al.* Gliosis and Neurodegenerative Diseases: The Role of PET and MR Imaging. *Front. Cell. Neurosci.* **14**, (2020).

20. Dupont, A.-C., Largeau, B., Guilloteau, D., Santiago Ribeiro, M. J. & Arlicot, N. The Place of PET to Assess New Therapeutic Effectiveness in Neurodegenerative Diseases. *Contrast Media Mol. Imaging* **2018**, 1–15 (2018).

21. Crimì, F. *et al.* [18F]FDG PET/MRI in rectal cancer. *Ann. Nucl. Med.* **35**, 281–290 (2021).

22. Salmanoglu, E. The role of [18F]FDG PET/CT for gastric cancer management. *Nucl. Med. Rev.* **24**, 99–103 (2021).

23. Caresia Aroztegui, A. P. *et al.* 18F-FDG PET/CT in breast cancer: Evidence-based recommendations in initial staging. *Tumor Biol.* **39**, 101042831772828 (2017).

24. Evangelista, L., Cuppari, L., Zattoni, F., Mansi, L. & Bombardieri, E. The future of choline PET in the era of prostate specific membrane antigen. *Q. J. Nucl. Med. Mol. Imaging* **63**, (2019).

25. Mesguich, C. *et al.* Choline PET/CT in Multiple Myeloma. *Cancers (Basel).* **12**, 1394 (2020).

26. Schmilovitz-Weiss, H. *et al.* [^{11}C] choline as a potential PET/CT biomarker of liver cirrhosis: A prospective pilot study. *Dig. Liver Dis.* **53**, 753–759 (2021).

27. Nakajo, K. *et al.* Maximum 11C-methionine PET uptake as a prognostic imaging biomarker for newly diagnosed and untreated astrocytic glioma. *Sci. Rep.* **12**, 546 (2022).

28. Hotta, M., Minamimoto, R. & Miwa, K. 11C-methionine-PET for differentiating recurrent brain tumor from radiation necrosis: radiomics approach with random forest classifier. *Sci. Rep.* **9**, 15666 (2019).

29. Tsuchiya, J. *et al.* Tumor Identification of Less Aggressive or Indolent Lymphoma With Whole-Body 11C-Acetate PET/CT. *Clin. Nucl. Med.* **44**, 276–281 (2019).

30. Esch, L. H., Fahlbusch, M., Albers, P., Hautzel, H. & Müller-Mattheis, V. 11C-acetate positron-emission tomography/computed tomography imaging for detection of recurrent disease after radical prostatectomy or radiotherapy in patients with prostate cancer. *BJU Int.* **120**, 337–342 (2017).

31. Nejabat, M. *et al.* [11C]acetate PET as a tool for diagnosis of liver steatosis. *Abdom. Radiol.* **43**, 2963–2969 (2018).

32. Ulaner, G. A., Hyman, D. M., Lyashchenko, S. K., Lewis, J. S. & Carrasquillo, J. A. 89Zr-Trastuzumab PET/CT for Detection of Human Epidermal Growth Factor Receptor 2–Positive Metastases in Patients With Human Epidermal Growth Factor Receptor 2–Negative Primary Breast Cancer. *Clin. Nucl. Med.* **42**, 912–917 (2017).

33. Jansen, M. H. *et al.* Molecular Drug Imaging: 89 Zr-Bevacizumab PET in Children with Diffuse Intrinsic Pontine Glioma. *J. Nucl. Med.* **58**, 711–716 (2017).

34. McKnight, B. N., Kim, S., Boerner, J. L. & Viola, N. T. Cetuximab PET delineated changes in cellular distribution of EGFR upon dasatinib treatment in triple negative breast cancer. *Breast Cancer Res.* **22**, 37 (2020).

35. García-Toraño, E., Peyrés Medina, V., Romero, E. & Roteta, M. Measurement of the half-life of 68Ga. *Appl. Radiat. Isot.* **87**, 122–125 (2014).

36. Heim, B., Krismer, F., De Marzi, R. & Seppi, K. Magnetic resonance imaging for the diagnosis of Parkinson's disease. *J. Neural Transm.* **124**, 915–964 (2017).

37. Moore, C. M. & Taneja, S. S. Integrating MRI for the diagnosis of prostate cancer. *Curr. Opin. Urol.* **26**, 466–471 (2016).

38. Zhang, Y. & Yu, J. The role of MRI in the diagnosis and treatment of gastric cancer. *Diagnostic Interv. Radiol.* **26**, 176–182 (2020).

39. Harms, S. E. MRI in breast cancer diagnosis and treatment. *Curr. Probl. Diagn. Radiol.* **25**, 192–215 (1996).

40. Lim, T.-H. & Choi, S. Il. MRI of myocardial infarction. *J. Magn. Reson. Imaging* **10**, 686–693 (1999).

41. Flavian, A. *et al.* Cardiac MRI in the diagnosis of complications of myocardial infarction. *Diagn. Interv. Imaging* **93**, 578–585 (2012).

42. Hemond, C. C. & Bakshi, R. Magnetic Resonance Imaging in Multiple Sclerosis. *Cold Spring Harb. Perspect. Med.* **8**, a028969 (2018).

43. Berger, A. Magnetic resonance imaging. *BMJ* **324**, 35 (2002).

44. Grover, V. P. B. *et al.* Magnetic Resonance Imaging: Principles and Techniques: Lessons for Clinicians. *J. Clin. Exp. Hepatol.* **5**, 246–255 (2015).

45. Hendrick, R. E. & Mark Haacke, E. Basic physics of MR contrast agents and maximization of image contrast. *J. Magn. Reson. Imaging* **3**, 137–148 (1993).

46. Caravan, P., Ellison, J. J., McMurry, T. J. & Lauffer, R. B. Gadolinium(III) Chelates as MRI Contrast Agents: Structure, Dynamics, and Applications. *Chem. Rev.* **99**, 2293–2352 (1999).

47. Zhou, Z. & Lu, Z.-R. Gadolinium-based contrast agents for magnetic resonance cancer imaging. *Wiley*

Interdiscip. Rev. Nanomedicine Nanobiotechnology **5**, 1–18 (2013).

48. Perazella, M. A. Current Status of Gadolinium Toxicity in Patients with Kidney Disease. *Clin. J. Am. Soc. Nephrol.* **4**, 461–469 (2009).
49. Buhaescu, I. & Izzedine, H. Gadolinium-induced nephrotoxicity. *Int. J. Clin. Pract.* **62**, 1113–1118 (2008).
50. Sargent, J. F. The National Nanotechnology Initiative: Overview, Reauthorization, and Appropriations Issues. *Congr. Res. Serv.* (2014).
51. Moghimi, S. M., Hunter, A. C. & Murray, J. C. Nanomedicine: current status and future prospects. *FASEB J.* **19**, 311–330 (2005).
52. Kawasaki, E. S. & Player, A. Nanotechnology, nanomedicine, and the development of new, effective therapies for cancer. *Nanomedicine Nanotechnology, Biol. Med.* **1**, 101–109 (2005).
53. Freitas, R. A. What is nanomedicine? *Nanomedicine Nanotechnology, Biol. Med.* **1**, 2–9 (2005).
54. Wagner, V., Dullaart, A., Bock, A.-K. & Zweck, A. The emerging nanomedicine landscape. *Nat. Biotechnol.* **24**, 1211–1217 (2006).
55. Erathodiyil, N. & Ying, J. Y. Functionalization of Inorganic Nanoparticles for Bioimaging Applications. *Acc. Chem. Res.* **44**, 925–935 (2011).
56. Zhang, X.-Y. & Zhang, P.-Y. Nanotechnology for multimodality treatment of cancer. *Oncol. Lett.* **12**, 4883–4886 (2016).
57. Anselmo, A. C. & Mitragotri, S. Nanoparticles in the clinic. *Bioeng. Transl. Med.* **1**, 10–29 (2016).
58. Castaneda, R. T., Khurana, A., Khan, R. & Daldrup-Link, H. E. Labeling Stem Cells with Ferumoxytol, an FDA-Approved Iron Oxide Nanoparticle. *J. Vis. Exp.* (2011) doi:10.3791/3482.
59. Akhiezer, I. A. & Chudnovskii, E. M. A theory of ferromagnetism of metals. *Solid State Commun.* **19**, 5–7 (1976).
60. Piehler, S. *et al.* Iron Oxide Nanoparticles as Carriers for DOX and Magnetic Hyperthermia after Intratumoral Application into Breast Cancer in Mice: Impact and Future Perspectives. *Nanomater. (Basel, Switzerland)* **10**, (2020).
61. Espinosa, A. *et al.* Duality of Iron Oxide Nanoparticles in Cancer Therapy: Amplification of Heating Efficiency by Magnetic Hyperthermia and Photothermal Bimodal Treatment. *ACS Nano* **10**, 2436–46 (2016).
62. Tseng, Y.-J. *et al.* A Versatile Theranostic Delivery Platform Integrating Magnetic Resonance Imaging/Computed Tomography, pH/cis-Diol Controlled Release, and Targeted Therapy. *ACS Nano* **10**, 5809–22 (2016).

63. Vangijzegem, T., Stanicki, D. & Laurent, S. Magnetic iron oxide nanoparticles for drug delivery: applications and characteristics. *Expert Opin. Drug Deliv.* **16**, 69–78 (2019).

64. Hannecart, A. *et al.* Nano-thermometers with thermo-sensitive polymer grafted USPIOs behaving as positive contrast agents in low-field MRI. *Nanoscale* **7**, 3754–67 (2015).

65. Zhang, Y., Guo, S., Zhang, P., Zhong, J. & Liu, W. Iron oxide magnetic nanoparticles based low-field MR thermometry. *Nanotechnology* **31**, 345101 (2020).

66. Wang, Q. *et al.* Artificially Engineered Cubic Iron Oxide Nanoparticle as a High-Performance Magnetic Particle Imaging Tracer for Stem Cell Tracking. *ACS Nano* **14**, 2053–2062 (2020).

67. Panagiotopoulos, N. *et al.* Magnetic particle imaging: current developments and future directions. *Int. J. Nanomedicine* **10**, 3097–114 (2015).

68. Gao, Z. *et al.* Small is Smarter: Nano MRI Contrast Agents - Advantages and Recent Achievements. *Small* **12**, 556–76 (2016).

69. Jeon, M., Halbert, M. V, Stephen, Z. R. & Zhang, M. Iron Oxide Nanoparticles as T1 Contrast Agents for Magnetic Resonance Imaging: Fundamentals, Challenges, Applications, and Prospectives. *Adv. Mater.* **33**, e1906539 (2021).

70. Laurent, S. *et al.* Magnetic iron oxide nanoparticles: synthesis, stabilization, vectorization, physicochemical characterizations, and biological applications. *Chem. Rev.* **108**, 2064–110 (2008).

71. Lee, N. & Hyeon, T. Designed synthesis of uniformly sized iron oxide nanoparticles for efficient magnetic resonance imaging contrast agents. *Chem. Soc. Rev.* **41**, 2575–89 (2012).

72. Zhang, C. *et al.* Mono-dispersed high magnetic resonance sensitive magnetite nanocluster probe for detection of nascent tumors by magnetic resonance molecular imaging. *Nanomedicine Nanotechnology, Biol. Med.* **8**, 996–1006 (2012).

73. Shevtsov, M. A. *et al.* Detection of experimental myocardium infarction in rats by MRI using heat shock protein 70 conjugated superparamagnetic iron oxide nanoparticle. *Nanomedicine Nanotechnology, Biol. Med.* **12**, 611–621 (2016).

74. Abakumov, M. A. *et al.* VEGF-targeted magnetic nanoparticles for MRI visualization of brain tumor. *Nanomedicine Nanotechnology, Biol. Med.* **11**, 825–833 (2015).

75. Priprem. Cytotoxicity Studies of Superparamagnetic Iron Oxide Nanoparticles in Macrophage and Liver Cells. *Am. J. Nanotechnol.* **1**, 78–85 (2010).

76. Leung, K. Molecular Imaging and Contrast Agent Database (MICAD). (2004).

77. Corot, C., Robert, P., Idée, J. M. & Port, M. Recent advances in iron oxide nanocrystal technology for medical imaging. *Adv. Drug Deliv. Rev.* **58**, 1471–1504 (2006).

78. Bhavesh, R., Lechuga-Vieco, A., Ruiz-Cabello, J. & Herranz, F. T1-MRI Fluorescent Iron Oxide Nanoparticles by Microwave Assisted Synthesis. *Nanomaterials* **5**, 1880–1890 (2015).

79. Glaus, C., Rossin, R., Welch, M. J. & Bao, G. In Vivo Evaluation of 64 Cu-Labeled Magnetic Nanoparticles as a Dual-Modality PET/MR Imaging Agent. *Bioconjug. Chem.* **21**, 715–722 (2010).

80. Jarrett, B. R., Correa, C., Ma, K. L. & Louie, A. Y. In Vivo Mapping of Vascular Inflammation Using Multimodal Imaging. *PLoS One* **5**, e13254 (2010).

81. Thorek, D. L. J. *et al.* Non-invasive mapping of deep-tissue lymph nodes in live animals using a multimodal PET/MRI nanoparticle. *Nat. Commun.* **5**, 3097 (2014).

82. Choi, J. *et al.* A Hybrid Nanoparticle Probe for Dual-Modality Positron Emission Tomography and Magnetic Resonance Imaging. *Angew. Chemie Int. Ed.* **47**, 6259–6262 (2008).

83. Devaraj, N. K., Keliher, E. J., Thurber, G. M., Nahrendorf, M. & Weissleder, R. 18 F Labeled Nanoparticles for in Vivo PET-CT Imaging. *Bioconjug. Chem.* **20**, 397–401 (2009).

84. Sun, Z. *et al.* Robust surface coating for a fast, facile fluorine-18 labeling of iron oxide nanoparticles for PET/MR dual-modality imaging. *Nanoscale* **8**, 19644–19653 (2016).

85. Sharma, R. *et al.* Carbon-11 radiolabeling of iron-oxide nanoparticles for dual-modality PET/MR imaging. *Nanoscale* **5**, 7476 (2013).

86. Madru, R. *et al.* (68)Ga-labeled superparamagnetic iron oxide nanoparticles (SPIONs) for multi-modality PET/MR/Cherenkov luminescence imaging of sentinel lymph nodes. *Am. J. Nucl. Med. Mol. Imaging* **4**, 60–9 (2013).

87. Kim, S. *et al.* Hybrid PET/MR imaging of tumors using an oleanolic acid-conjugated nanoparticle. *Biomaterials* **34**, 8114–8121 (2013).

88. Moon, S.-H. *et al.* Development of a complementary PET/MR dual-modal imaging probe for targeting prostate-specific membrane antigen (PSMA). *Nanomedicine Nanotechnology, Biol. Med.* **12**, 871–879 (2016).

89. Yang, B. Y. *et al.* Development of a multimodal imaging probe by encapsulating iron oxide nanoparticles with functionalized amphiphiles for lymph node imaging. *Nanomedicine* **10**, 1899–1910 (2015).

90. Comes Franchini, M. *et al.* Biocompatible nanocomposite for PET/MRI hybrid imaging. *Int. J. Nanomedicine* **7**, 6021 (2012).

91. Karageorgou, M.-A. *et al.* Gallium-68 Labeled Iron Oxide Nanoparticles Coated with 2,3-Dicarboxypropane-1,1-diphosphonic Acid as a Potential PET/MR Imaging Agent: A Proof-of-Concept Study. *Contrast Media Mol. Imaging* **2017**, 1–13 (2017).

92. Lee, H.-Y. *et al.* PET/MRI Dual-Modality Tumor Imaging Using Arginine-Glycine-Aspartic (RGD)–Conjugated Radiolabeled Iron Oxide Nanoparticles. *J. Nucl. Med.* **49**, 1371–1379 (2008).

93. Patel, D. *et al.* The cell labeling efficacy, cytotoxicity and relaxivity of copper-activated MRI/PET imaging contrast agents. *Biomaterials* **32**, 1167–1176 (2011).

94. Zeng, J. *et al.* In situ111In-doping for achieving biocompatible and non-leachable 111In-labeled Fe3O4 nanoparticles. *Chem. Commun.* **50**, 2170 (2014).

95. Weissleder, R. *et al.* Superparamagnetic iron oxide: pharmacokinetics and toxicity. *Am. J. Roentgenol.* **152**, 167–173 (1989).

96. Chouly, C., Pouliquen, D., Lucet, I., Jeune, J. J. & Jallet, P. Development of superparamagnetic nanoparticles for MRI: effect of particle size, charge and surface nature on biodistribution. *J. Microencapsul.* **13**, 245–255 (1996).

97. Cędrowska, E. *et al.* Trastuzumab Conjugated Superparamagnetic Iron Oxide Nanoparticles Labeled with 225Ac as a Perspective Tool for Combined α-Radioimmunotherapy and Magnetic Hyperthermia of HER2-Positive Breast Cancer. *Molecules* **25**, 1025 (2020).

98. Wong, R. M., Gilbert, D. A., Liu, K. & Louie, A. Y. Rapid Size-Controlled Synthesis of Dextran-Coated, 64 Cu-Doped Iron Oxide Nanoparticles. *ACS Nano* **6**, 3461–3467 (2012).

99. Carenza, E. *et al.* Rapid synthesis of water-dispersible superparamagnetic iron oxide nanoparticles by a microwave-assisted route for safe labeling of endothelial progenitor cells. *Acta Biomater.* **10**, 3775–85 (2014).

100. Fernández-Barahona, I., Muñoz-Hernando, M. & Herranz, F. Microwave-Driven Synthesis of Iron-Oxide Nanoparticles for Molecular Imaging. *Molecules* **24**, (2019).

101. Gallo-Cordova, A. *et al.* Engineering Iron Oxide Nanocatalysts by a Microwave-Assisted Polyol Method for the Magnetically Induced Degradation of Organic Pollutants. *Nanomater. (Basel, Switzerland)* **11**, (2021).

102. Li, L. *et al.* Effect of synthesis conditions on the properties of citric-acid coated iron oxide nanoparticles. *Microelectron. Eng.* **110**, 329–334 (2013).

103. Liu, C. & Huang, P. M. Atomic Force Microscopy and Surface Characteristics of Iron Oxides Formed in Citrate Solutions. *Soil Sci. Soc. Am. J.* **63**, 65–72 (1999).

104. Fortin, J.-P., Gazeau, F. & Wilhelm, C. Intracellular heating of living cells through Néel relaxation of magnetic nanoparticles. *Eur. Biophys. J.* **37**, 223–228 (2008).

105. Gutierrez, L., Aubry, C., Cornejo, M. & Croue, J.-P. Citrate-Coated Silver Nanoparticles Interactions with Effluent Organic Matter: Influence of Capping Agent and Solution Conditions. *Langmuir* **31**,

8865–8872 (2015).

106. Ojea-Jiménez, I., López, X., Arbiol, J. & Puntes, V. Citrate-Coated Gold Nanoparticles As Smart Scavengers for Mercury(II) Removal from Polluted Waters. *ACS Nano* **6**, 2253–2260 (2012).

107. Kotsmar, C. *et al.* Stable Citrate-Coated Iron Oxide Superparamagnetic Nanoclusters at High Salinity. *Ind. Eng. Chem. Res.* **49**, 12435–12443 (2010).

108. Liang, Q. *et al.* Citric Acid Capped Iron Oxide Nanoparticles as an Effective MALDI Matrix for Polymers. *J. Am. Soc. Mass Spectrom.* **28**, 409–418 (2017).

109. Pellico, J. *et al.* In vivo imaging of lung inflammation with neutrophil-specific 68Ga nano-radiotracer. *Sci. Rep.* **7**, 13242 (2017).

110. Adrover, J. M. *et al.* Thrombo-tag, an in vivo formed nanotracer for the detection of thrombi in mice by fast pre-targeted molecular imaging. *Nanoscale* **12**, 22978–22987 (2020).

111. Pellico, J. *et al.* Unambiguous detection of atherosclerosis using bioorthogonal nanomaterials. *Nanomedicine Nanotechnology, Biol. Med.* **17**, 26–35 (2019).

112. Wong, R. M., Gilbert, D. A., Liu, K. & Louie, A. Y. Rapid Size-Controlled Synthesis of Dextran-Coated, 64 Cu-Doped Iron Oxide Nanoparticles. *ACS Nano* **6**, 3461–3467 (2012).

113. Fantechi, E. *et al.* Exploring the Effect of Co Doping in Fine Maghemite Nanoparticles. *J. Phys. Chem. C* **116**, 8261–8270 (2012).

114. Moise, S. *et al.* The cellular magnetic response and biocompatibility of biogenic zinc- and cobalt-doped magnetite nanoparticles. *Sci. Rep.* **7**, 39922 (2017).

115. Jang, J. *et al.* Critical Enhancements of MRI Contrast and Hyperthermic Effects by Dopant-Controlled Magnetic Nanoparticles. *Angew. Chemie Int. Ed.* **48**, 1234–1238 (2009).

116. Yin, X. *et al.* Large T1 contrast enhancement using superparamagnetic nanoparticles in ultra-low field MRI. *Sci. Rep.* **8**, 11863 (2018).

117. Li, Z. *et al.* Ultrasmall Manganese Ferrite Nanoparticles as Positive Contrast Agent for Magnetic Resonance Imaging. *Adv. Healthc. Mater.* **2**, 958–964 (2013).

118. Zhang, M. *et al.* Manganese doped iron oxide theranostic nanoparticles for combined T 1 magnetic resonance imaging and photothermal therapy. *ACS Appl. Mater. Interfaces* **7**, 4650–4658 (2015).

119. Xiao, N. *et al.* T1–T2 dual-modal MRI of brain gliomas using PEGylated Gd-doped iron oxide nanoparticles. *J. Colloid Interface Sci.* **417**, 159–165 (2014).

120. Abbasi Pour, S., Shaterian, H. R., Afradi, M. & Yazdani-Elah-Abadi, A. Carboxymethyl cellulose (CMC)-loaded Co-Cu doped manganese ferrite nanorods as a new dual-modal simultaneous contrast agent for magnetic resonance imaging and nanocarrier for drug delivery system. *J. Magn. Magn.*

Mater. **438**, 85–94 (2017).

121. Kratz, J. D., Chaddha, A., Bhattacharjee, S. & Goonewardena, S. N. Atherosclerosis and Nanotechnology: Diagnostic and Therapeutic Applications. *Cardiovasc. Drugs Ther.* **30**, 33–39 (2016).

122. Barrett, H. E., Van der Heiden, K., Farrell, E., Gijsen, F. J. H. & Akyildiz, A. C. Calcifications in atherosclerotic plaques and impact on plaque biomechanics. *J. Biomech.* **87**, 1–12 (2019).

123. Bentzon, J. F., Otsuka, F., Virmani, R. & Falk, E. Mechanisms of Plaque Formation and Rupture. *Circ. Res.* **114**, 1852–1866 (2014).

124. Mathers, C. D. & Loncar, D. Projections of Global Mortality and Burden of Disease from 2002 to 2030. *PLoS Med.* **3**, e442 (2006).

125. Libby, P. The Forgotten Majority. *J. Am. Coll. Cardiol.* **46**, 1225–1228 (2005).

126. Jia, H. *et al.* In Vivo Diagnosis of Plaque Erosion and Calcified Nodule in Patients With Acute Coronary Syndrome by Intravascular Optical Coherence Tomography. *J. Am. Coll. Cardiol.* **62**, 1748–1758 (2013).

127. Yahagi, K., Davis, H. R., Arbustini, E. & Virmani, R. Sex differences in coronary artery disease: Pathological observations. *Atherosclerosis* **239**, 260–267 (2015).

128. Spagnoli, L. G. Extracranial Thrombotically Active Carotid Plaque as a Risk Factor for Ischemic Stroke. *JAMA* **292**, 1845 (2004).

129. Rader, D. J. & Daugherty, A. Translating molecular discoveries into new therapies for atherosclerosis. *Nature* **451**, 904–913 (2008).

130. Albanese, I., Khan, K., Barratt, B., Al-Kindi, H. & Schwertani, A. Atherosclerotic Calcification: Wnt Is the Hint. *J. Am. Heart Assoc.* **7**, (2018).

131. Czernin, J., Satyamurthy, N. & Schiepers, C. Molecular Mechanisms of Bone 18 F-NaF Deposition. *J. Nucl. Med.* **51**, 1826–1829 (2010).

132. Felix, D. D. *et al.* Detection of breast cancer microcalcification using 99mTc-MDP SPECT or Osteosense 750EX FMT imaging. *Nucl. Med. Biol.* **42**, 269–273 (2015).

133. Wilson, G. H. *et al.* An Approach to Breast Cancer Diagnosis via PET Imaging of Microcalcifications Using 18 F-NaF. *J. Nucl. Med.* **55**, 1138–1143 (2014).

134. Ordonez, A. A., DeMarco, V. P., Klunk, M. H., Pokkali, S. & Jain, S. K. Imaging Chronic Tuberculous Lesions Using Sodium [18F]Fluoride Positron Emission Tomography in Mice. *Mol. Imaging Biol.* **17**, 609–614 (2015).

135. Judenhofer, M. S. *et al.* Simultaneous PET-MRI: a new approach for functional and morphological imaging. *Nat. Med.* **14**, 459–465 (2008).

136. Robson, P. M. *et al.* Coronary Artery PET/MR Imaging. *JACC Cardiovasc. Imaging* **10**, 1103–1112 (2017).